AFIT/DS/ENG/92-06

INCREASING THE CORRECTED FIELD OF VIEW OF AN ADAPTIVE OPTICAL TELESCOPE

DISSERTATION

Dustin Clay Johnston
Captain, USAF

AFIT/DS/ENG/92-06

AFIT/DS/ENG/92-06

INCREASING THE CORRECTED FIELD OF VIEW OF AN ADAPTIVE OPTICAL TELESCOPE

DISSERTATION

Presented to the Faculty of the School of Engineering

of the Air Force Institute of Technology

Air University

In Partial Fulfillment of the

Requirements for the Degree of

Doctor of Philosophy

Dustin Clay Johnston, B.S.E.E., M.S.E.E.

Captain, USAF

December, 1992

AFIT/DS/ENG/92-06

INCREASING THE CORRECTED FIELD OF VIEW OF AN ADAPTIVE OPTICAL TELESCOPE

Dustin Clay Johnston, B.S.E.E., M.S.E.E.

Captain, USAF

Approved:

Byron M White	23 Nov 92
Johnny W Lunn	23 NOV 92
Donald Rok	23 Nov 92
[illegible]	23 Nov 92
Dennis W. Ruck	23 Nov 92

J. S. Przemieniecki 23 Nov 92

J. S. Przemieniecki

Senior Dean

Acknowledgements

I am indebted to many people for their help and encouragement during my research program. First of all, I could not have had a better advisor than Dr Byron Welsh. He patiently answered my questions and helped me develop an intuitive, as well as analytical, understanding of atmospheric and adaptive optics. He kept the faith at times when I thought the problem was unsolvable, obtained the resources I needed, and supported my attendance and participation in a number of conferences at which I could learn from the most important contributors in the field. I would also like to thank my other committee members, Dr Dennis Quinn, Major Steven Rogers, and Dr Won Roh for their insight and observations. The Air Force Phillips Laboratory sponsored this research, and discussions with two Phillips Lab scientists, Dr Brent Ellerbroek and Capt Michael Roggemann, were extremely valuable. In particular, I would like to thank Capt Roggemann for helping me obtain an opportunity to publish some of my work, and Dr Ellerbroek for an invitation to participate in a conference. Thanks also to Mr Dan Zambon for keeping the computers running. On a personal level, I would like to thank the members of Beavercreek Baptist Church for their prayers and friendship. Most of all, thank you Barbara, Steven, and Scott for your love, patience, and encouragement while I was at AFIT.

Dustin Clay Johnston

Table of Contents

List of Figures

List of Tables

Abstract

Current adaptive optical telescope designs use a single deformable mirror (DM), usually conjugated to the telescope pupil, to compensate for the cumulative effects of optical turbulence along a single observation direction. The corrected field of view (FOV) of an adaptive optics system could theoretically be increased through the use of multiple DMs optically conjugated to a like number of corresponding planes which sample the turbulence region in altitude. Often, the atmospheric turbulence responsible for the degradation of long-exposure telescope images is concentrated in several relatively strong layers. The logical location for the conjugate planes in a multiconjugate adaptive optics (MCAO) system would be the same as these "seeing layers." Each DM would correct for the component of the total wavefront in the pupil contributed by its corresponding turbulent layer. If the atmosphere does not possess a distinctly layered structure, the best fit of the turbulence profile can be made to a layered model, with the number of layers in the model equal to the number of DMs. This dissertation describes and analyzes two novel methods for estimating the proper DM surfaces which would result in wide-FOV compensation. Both methods take advantage of spatial diversity in multiple wavefront sensor (WFS) measurements in order to reconstruct an estimate of the three-dimensional turbulence structure. The wavefront measurements are made using an array of artificial guide stars created by scattered laser light. The analysis includes the integrated effects of measurement noise, realistic models of systems components, and the limitations of artificial guide stars. It is shown that multiple-DM, multiple-guide-star systems can significantly increase the compensated FOV relative to single-DM, single-guide star systems.

INCREASING THE CORRECTED FIELD OF VIEW OF AN ADAPTIVE OPTICAL TELESCOPE

I. Introduction

1.1 Problem Statement

Nearly 40 years after Horace Babcock suggested "the possibility of compensating astronomical seeing" (2), the development of adaptive optics technology has enabled the production of binary star images which have been substantially corrected for atmospheric distortion (20, 46, 55). We have not yet seen, however, similar high-resolution images of planets, galaxies, or nebulae. The reason is that the high level of compensation achieved by adaptive optical telescopes is effective only over a small field area called the isoplanatic patch. At visible wavelengths, even in excellent observing conditions, the isoplanatic patch is only a few arcseconds (i.e. a few tens of microradians) in diameter (49). Many interesting astronomical objects, however, extend from several tens of arcseconds to arcminutes in apparent size. The desire to obtain high-resolution images of these objects from ground-based telescopes is one motivation for solving the problem addressed in this dissertation:

> Develop a method for increasing the corrected field of view (FOV) of an adaptive optical telescope for astronomical imaging and conduct a performance analysis of an adaptive telescope which incorporates this technique.

Adaptive optics literature contains statements of the need for developing a method for increasing the corrected FOV, and informal reports have advanced heuristic suggestions as to how to approach the problem, but no detailed work on corrected FOV widening has been published. The result of the proposed research is a detailed performance analysis of a new adaptive optics system design. The

goal of the analysis was to quantify both the benefits and the costs of increasing the corrected FOV, as compared with other adaptive telescope designs found in the literature. The outcome of this research includes the first in-depth contributions in the area of adaptive optics FOV widening (38, 39).

This dissertation is organized into five chapters. Chapter I presents the justification for pursuing the suggested study and details the problem to be solved. Chapter II is background material, intended to familiarize the reader with the current state of the art and summarize information about optical systems analysis, atmospheric turbulence effects on imaging, and adaptive optics. Chapter III contains an approximate frequency domain analysis of the FOV widening problem while Chapter IV, the main work of the dissertation, describes a rigorous spatial domain analysis. Conclusions and recommendations for further research are found in chapter V. Mathematical details and results not included in the main text are compiled in the Appendices.

1.2 Justification for Conducting the Proposed Research

In 1989, astronomers at the Observatoir de Haute Provence, France, were the first non-military researchers to obtain astronomical photographic images corrected to the diffraction limit of the telescope with adaptive optics (55). This experiment was conducted at infrared wavelengths (2.2–5 μm); adaptive optics is considerably more difficult to implement in the visible region of the spectrum where the effects of atmospheric turbulence are more pronounced and hence, harder to correct. Recently, the U.S. Air Force has revealed the existence of a 1.5-meter adaptive telescope at the Starfire Optical Range (SOR) in New Mexico, with which they have obtained a number of strikingly resolved astronomical images with visible light (20). Prior to these May, 1991, Air Force announcements, Welsn and Gardner had predicted the performance of an adaptive optical telescope based on a detailed theoretical analysis (64). They show that the corrected FOV of this telescope will be only a few arcseconds in diameter. Many interesting astronomical objects, such as planets

(47″ for Jupiter), nebulae (up to 20′), and the sun (32′), subtend angles significantly larger than this expected FOV.

The military's interest in adaptive telescopes stems from intelligence gathering requirements such as imaging earth-orbiting satellites (1). Air Force researchers at the SOR list "wide-FOV adaptive optics" on their agenda of future research (21). Beckers (5), Fried (19), and Hardy (30), prominent researchers in the field of adaptive optics, have written papers discussing the requirement for FOV widening of adaptive optical systems. Although they suggested ways to look for a solution, neither they nor any other researcher has published a detailed study of this problem.

1.3 Approach

The small size of the compensated field of an adaptive optical telescope does not result from component limitations such as measurement noise but from a more fundamental source: the vertical extent of the atmospheric turbulence structure. Although atmospheric refractive index inhomogeneities, which are the source of astronomical image distortion, form a three-dimensional spatial random process, a conventional adaptive optical telescope applies only a two-dimensional spatial correction using a single deformable mirror (DM). The DM surface is intended to undo the optical phase distortion caused by the atmosphere, but it can only do so for the *cumulative* phase distortion along one propagation direction. This direction of optimum compensation will correspond to the location of the reference source, or guide star, which is used for the atmospheric distortion measurements. The correlation between the surface of the DM and the cumulative phase distortion along other propagation directions drops off rapidly with the offset angle between the reference and observation directions.

One approach to increase the corrected field of view of an adaptive optical telescope is to devise a method of applying a three-dimensional correction for atmospheric distortion. An example of a three-dimensional phase correction system would be a series of DMs in the optical train of the

adaptive telescope. Dicke was the first to suggest this idea (11), proposing a two-DM system to correct for low and high altitude contributions to atmospheric distortion. More recently, Beckers has considered this concept, coining the term "multiconjugate adaptive optics (MCAO)." Beckers suggested optically conjugating each DM to a plane at a specified distance from the telescope aperture (5). Ideally, these conjugate planes would be located at altitudes where the atmospheric turbulence strength is chiefly concentrated.

To illustrate the idea of MCAO, Figure 1.1 depicts a schematic comparison between single-DM and two-DM correction when the atmospheric phase distortion is confined to two thin turbulent layers. The phases, ϕ_i (rad), in the figure represent the contribution to the phase distortion by the indicated point in the turbulent layer. In Figure 1.1(a), a ray from object point 1 to the indicated point in the aperture plane undergoes a cumulative phase distortion of $\phi_1 + \phi_3$ rad. If this object point is used as the reference, a phase compensation $\phi_c = -\phi_1 - \phi_3$ rad is applied in the aperture plane. (Usually, the DM is optically conjugated to the aperture plane, so we can imagine the phase correction taking place in this plane.) A ray from object point 2 to the same point in the aperture plane has accumulated a phase deviation of $\phi_2 + \phi_4$ rad. Depending on the spatial correlation of the layers, the phase compensation ϕ_c, appropriate for object point 1, may be of little benefit in compensating a wavefront propagating from object point 2. This decorrelation of the phase correction with offset angle is known as angular anisoplanatism. Even for a "perfect" adaptive optical telescope, having no measurement noise or DM figuring error, angular anisoplanatism presents a fundamental limit to performance.

Now consider Figure 1.1(b). Instead of a single phase correction in the aperture plane, this figure shows two separate phase corrections made in the conjugate planes of the turbulent layers. The surface of DM 1 is figured to negate the phase aberration caused by turbulent layer 1, while DM 2 compensates for turbulent layer 2. In this case, the rays from both object points receive the correct phase compensation. Assuming the availability of ideal adaptive optical components,

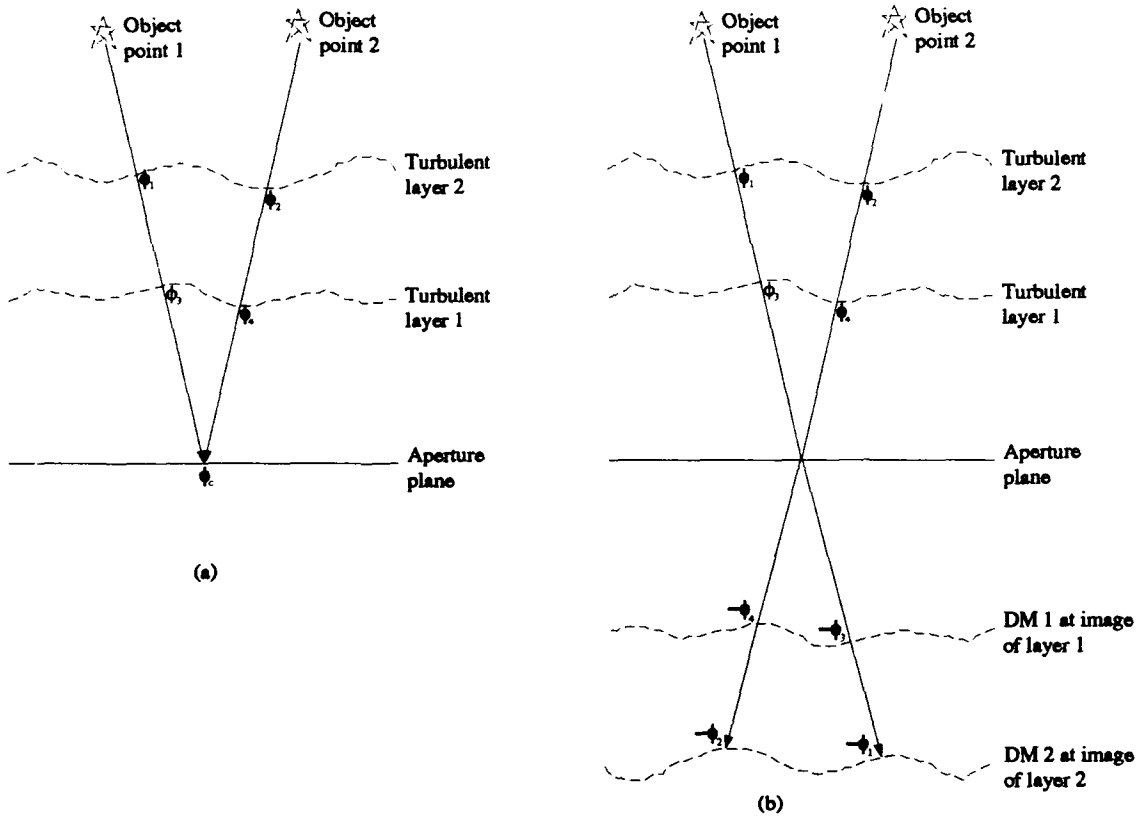

Figure 1.1. Schematic comparison between single-DM correction and 2-DM correction when atmospheric distortion is caused by 2 thin turbulent layers.

angular anisoplanatism could be completely eliminated when the number of thin turbulent layers equals the number of DMs.

We have seen in the preceding example that MCAO can eliminate angular anisoplanatism when optical turbulence can be accurately modeled by a small number of thin phase-changing screens. Ultimately, we would like to know if MCAO can significantly widen the corrected FOV of an adaptive optical telescope over a variety of realistic turbulence conditions. Before this question can be answered, however, we need to determine a means of estimating the individual contributions of different layers of the atmosphere to the total wavefront aberration in the aperture of the telescope. An estimate of the contribution of the individual layers is required in order to properly figure the conjugated DMs. Dicke first suggested that high and low altitude turbulence effects could be distinguished using the difference in the wind speed at the two altitudes. By comparing phase distortion measurements made approximately 0.01 sec apart, he presumed that the low and high altitude phase distortion contributions could be separated (11). It is not known if Dicke's scheme was ever implemented, but his concept of processing multiple linearly independent wavefront measurements to estimate the phase contributions of different parts of the atmosphere is the key to the approach presented in this dissertation.

Fried suggested obtaining the multiple wavefront measurements by projecting through the turbulence region at a variety of angles using multiple reference sources (19). The measurements are linearly independent in this case because they are separated spatially, rather than temporally as in Dicke's proposal. To determine what phase function to put on the surface of the DMs, Fried suggested interpreting the measurements as arising from propagation through a series of phase screens, the number of phase screens equal to the number of DMs. Even if the turbulence does not have a layered structure, one could make the best fit of a layered structure to the measured data. Although angular anisoplanatism may not be completely eliminated, it is hoped that it could be substantially mitigated.

The advent of the laser guide star, or synthetic beacon, has raised the practical possibility of multiple linearly independent wavefront measurements in astronomical applications of adaptive optics (15, 20, 35, 50, 58, 65). Artificial reference sources are necessary because there are too few natural stars bright enough to use as reference sources for the wavefront sensor (WFS) measurements. Beckers (5) and Tallon and Foy (57) have proposed ways to combine the wavefront measurements from each reference source to obtain the correct phase perturbation values to associate with each phase screen in the propagation path. Beckers' idea involves spatially shifting each measurement to "line up" the contribution of a particular phase screen across the ensemble. The contributions of the other phase screens will be misaligned. An average of the measurements would then presumably be weighted toward the contribution of the desired phase screen, while the other contributions will tend to average out. Tallon and Foy suggest modeling each phase screen as a mosaic of coherence areas. Two rays passing through the same coherence area are considered to have experienced the same phase perturbation. A constellation of artificial guide stars is arranged so that all the coherence areas in all the phase screens are probed. To obtain the phase map associated with each phase screen, Tallon and Foy suggest constructing and solving a system of linear equations, with the phase perturbations associated with each coherence area as the unknowns and the Hartmann WFS measurements as the known quantities. A detailed analysis of either of these proposed methods for estimating the phase screen functions has not been published.

In this dissertation, two novel methods of obtaining the phase screen contributions from WFS measurements are proposed. The first method involves transforming the phase functions into the spatial frequency domain. The transforms of the WFS measurements are linearly combined to obtain estimates of the transforms of the phase screen contributions. In computing the linear combination of measurements, an optimum set of complex weights is derived in order to minimize the mean-squared error in the estimated phase screen contribution. Since complex weights in the spatial frequency domain correspond to amplitude weighting and shifting in the spatial domain,

this estimation approach is similar to, but more general than that proposed by Beckers. Details of this frequency domain approach are the subject of Chapter III.

The second approach, detailed in Chapter IV, is to work in the spatial domain and estimate the phase screen contributions as a linear combination of wavefront slope measurements. This approach is an extension of the method presented by Wallner in (62). Whereas Wallner only used a single guide star to estimate the total wavefront phase, this dissertation describes for the first time how to combine multiple wavefront measurements to estimate the contribution of different parts of the atmosphere to the total wavefront phase. Both approaches assume *a priori* knowledge of the atmospheric turbulence conditions, which must be obtained from a remote sensing instrument.

Before construction of an MCAO system can be considered, a theoretical analysis of the concept is in order. Such an analysis is necessary to answer several questions concerning practical issues. For example, how accurately can we estimate each phase perturbation function? How much improvement in the corrected FOV may be expected for a particular atmospheric turbulence structure, given a specified number of DMs? What is the effect of WFS noise and DM figuring error on such a system? The purpose of this dissertation is to present analysis methods which can be used to study these questions.

1.4 Assumptions

Three major assumptions are made in this dissertation: 1) geometrical optics is adequate to describe propagation down through the atmosphere at a good observatory site, 2) the atmospheric turbulence structure at such a site may be modeled as a series of phase-changing screens, and 3) multiple reference sources, less than one arcminute apart, are available for WFS measurements. By assuming geometrical optics propagation, any refraction or diffraction of optical waves traversing the atmosphere is ignored. In other words, the only atmospheric effect considered is phase delay due to optical path length changes caused by variations in the index of refraction. The validity

of this assumption can only be established experimentally—doing so is beyond the scope of this dissertation. Regardless of the results of this research, successful practical implementation of MCAO depends on how closely the near field criterion approximates reality. Most researchers consider this assumption to be valid for a good observatory site (5, 26, 63). A theoretical argument in support of the validity of this assumption is presented in Section 2.3.5.

Several factors motivated the use of a layered atmosphere model for an initial analysis of MCAO. One reason is that experimental evidence indicates that the optical turbulence in the atmosphere is often concentrated in a small number of layers (52, 61). However, we could approximate any turbulence distribution by using a sufficient number of layers. Since an MCAO system approximates a layered atmospheric structure, the use of such a model is convenient for analysis purposes. In addition, it allows the mathematical results to be expressed in terms of the phase statistics instead of refractive index statistics.

Earlier it was pointed out that, due to the lack of adequate natural stars, the multiple WFS reference sources in an MCAO system must be artificially generated by laser backscatter. Practical issues not addressed in this dissertation include accurate calibration of the synthetic beacon projection system and associating wavefront measurements with the correct reference source. It is assumed that the beacons can be projected with offset angles on the order of a few arcseconds and that all phase perturbation measurements can be made within the atmosphere's correlation time (27) so that time multiplexing can be used to associate the measurements and reference stars. This requirement clearly limits the number of measurements, but researchers have already demonstrated adaptive optics using sequential wavefront measurements from two artificial guide stars (47).

1.5 Scope

The analysis in this dissertation involves only spatial, not temporal, quantities and the scope of the analysis is limited to open-loop operation (i.e., the system measures and reconstructs the incoming wavefronts individually vs. nulling the residual phase error via a feedback loop). Optical design issues (materials, losses, etc.) are not considered. This dissertation concentrates on studying signal processing techniques as opposed to the design of wavefront sensing devices and methods.

1.6 Significant Results

Two novel methods for obtaining the correct DM surface functions are developed. Additionally, thorough analysis demonstrates for the first time that MCAO is a promising technology for increasing the compensated FOV of an adaptive optical telescope. However, the inability of artificial guide star systems to sense overall tilt limits the theoretical performance of MCAO systems.

1.7 Summary

In this chapter we have described the dissertation problem, which is to analyze a method for increasing the corrected FOV of an adaptive optical telescope. The approach is to add additional wavefront correcting elements (DMs) in the optical train of the telescope. To obtain the commands for multiple DMs, multiple linearly independent measurements of the atmospheric phase distortion are needed. The main work of this dissertation involves proposing and analyzing methods for obtaining the DM commands from the measurements. Before describing this analysis in chapters III and IV, the next chapter presents some background material on atmospheric and adaptive optics.

II. Background

2.1 Introduction

It is well known that the atmosphere degrades the performance of optical imaging systems such as ground-based astronomical telescopes. This atmospheric distortion is the result of inhomogeneities in the index of refraction, n, of the air, randomized by the turbulent mixing which results from solar heating. During the past several decades, great progress has been made in describing and measuring the effects of turbulence on light passing through the atmosphere and in devising methods of correcting for these effects (29, 31, 43, 60). Such image compensation methods fall into two categories: predetection and post-detection compensation. Post-detection compensation entails processing already blurred images to reduce the degradation due to the interfering atmosphere. This post-processing usually involves multiple short-exposure images, that is, images obtained using an integration time sufficiently short to "freeze" a particular realization of the random atmospheric turbulence structure. Predetection compensation, also known as adaptive optics, involves nulling the phase component of the distortion in real-time using a servo loop. This dissertation is concerned with predetection compensation systems.

In chapters III and IV, the performance of adaptive optics systems will be evaluated in terms of the variance of the phase aberration function in the pupil plane of the telescope. In the context of adaptive optics system analysis, the error that remains after compensation is of interest. Thus this criterion is often referred to as "mean-square residual phase error." The reason this criterion is chosen is because it is directly related to optical system performance. Specifically, as shown in Section 2.2, the phase aberration function determines the system optical transfer function (OTF), point spread function, and Strehl ratio. Other concepts underlying the analysis in chapters III and IV include the refractive index structure constant, C_n^2, phase structure function, $\mathcal{D}_\psi$, and the atmospheric coherence diameter, r_0. Section 2.3 defines these terms and relates them to each other.

Finally sections 2.4 and 2.5 provide background on adaptive optical telescopes and laser guide stars, respectively.

2.2 *Incoherent Optical Systems Analysis*

2.2.1 Optical Transfer Function. Consider Goodman's generalized model of an imaging system shown in Figure 2.1. The object being imaged lies in the $x_o y_o$ plane. The coordinates of the object plane are normalized by the magnification of the imaging system such that if the physical coordinates of a point on the object are (X_0, Y_0), then its coordinates in the $x_o y_o$ plane are given by $x_0 = MX_0, y_0 = MY_0$, where M is the system magnification. Note that M can be either negative or positive; negative M indicating that the image is inverted. With this normalization, an object point and its corresponding point in the image $(x_i y_i)$ plane will have the same coordinate values.

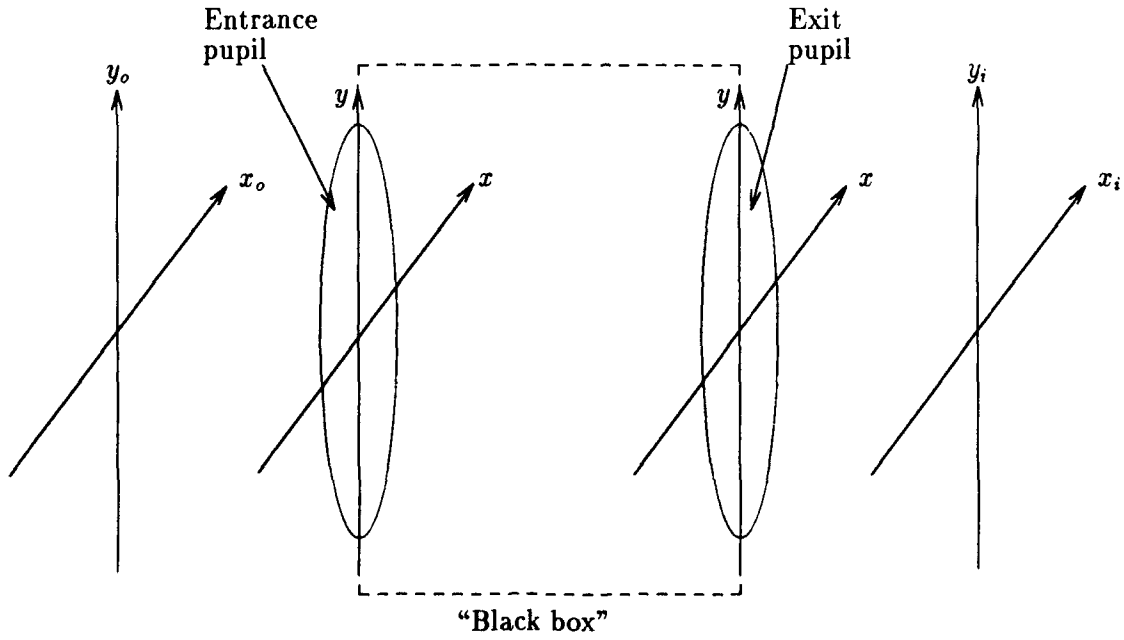

Figure 2.1. Generalized model of an imaging system (25).

The imaging system may be mathematically modeled by a transmission function (7), also known as the impulse response function (37), represented by $\mathbf{h}(x_o, y_o; x_i, y_i; \lambda)$ with λ representing wavelength and bold type indicating a complex quantity. Born and Wolf define $\mathbf{h}$ as the normalized

complex amplitude at image point (x_i, y_i), due to a unit amplitude, zero phase disturbance at object point (x_o, y_o) (7). In many cases, optical systems analysis is performed using the form of $\mathbf{h}$ derived for monochromatic light, therefore the wavelength dependence will be dropped from this point on.

From the Huygens-Fresnel principle and electromagnetic theory, it is known that the propagation of light is a linear phenomenon. Hence, if $\mathbf{u}_o$ is the complex amplitude of the optical field emitted from the object, the complex amplitude of the optical field in the image plane can be found by means of a superposition integral (7):

$$\mathbf{u}_i(\vec{x}_i, t) = \int d^2\vec{x}_o \, \mathbf{u}_o(\vec{x}_o, t)\mathbf{h}(\vec{x}_o, \vec{x}_i) \tag{2.1}$$

where t indicates a time varying object and image field and $\vec{x} = (x, y)$ is a two-dimensional position vector. The limits of integration are formally infinite but effectively defined by $\mathbf{h}$. For the finite region of the object plane known as the isoplanatic region, the transmission function of a good optical system will be shift invariant. Hence, for objects smaller than the isoplanatic region, equation (2.1) can be written as a convolution integral (7):

$$\mathbf{u}_i(\vec{x}_i, t) = \int d^2\vec{x}_o \, \mathbf{u}_o(\vec{x}_o, t)\mathbf{h}(\vec{x}_i - \vec{x}_o) \tag{2.2}$$

A practical imaging system records the image intensity, I_i, which is defined as the time average of the magnitude squared of the complex field amplitude. Using angle brackets to denote averaging in time and $\mathbf{z}^*$ for the complex conjugate of $\mathbf{z}$, the image intensity can be written as (37)

$$I_i(\vec{x}_i) = \int d^2\vec{x}_o \int d^2\vec{x}'_o \, \langle \mathbf{u}_o(\vec{x}_o, t)\mathbf{u}_o^*(\vec{x}'_o, t)\rangle \mathbf{h}(\vec{v}_i - \vec{x}_o)\mathbf{h}^*(\vec{x}_i - \vec{x}'_o) \tag{2.3}$$

For the case of an object radiating incoherent light, the image intensity can be easily related to the object intensity. For the incoherent imaging case, the object mutual intensity is given by (37)

$$\langle \mathbf{u}_o(\vec{x}_o, t)\mathbf{u}_o^*(\vec{x}_o', t)\rangle = |\mathbf{u}_o(\vec{x}_o)|^2\delta(\vec{x}_o - \vec{x}_o') = I_o(\vec{x}_o)\delta(\vec{x}_o - \vec{x}_o') \tag{2.4}$$

Substituting equation (2.4) into equation (2.3) and using the sifting property of the Dirac delta function, $\delta(\vec{x}\,)$, it is found that the image intensity for an optical system in the presence of incoherent light is described by the following expression, in which the operator $*$ stands for convolution (37):

$$I_i(\vec{x}_i) = I_o(\vec{x}_i) * |\mathbf{h}(\vec{x}_i)|^2 \tag{2.5}$$

The Fourier transform of the preceding relationship may be used to analyze the optical system in the spatial frequency domain. Typically, the Fourier transforms of each of the quantities in equation (2.5) are normalized by their zero-frequency values. Using script letters to indicate these normalized Fourier transforms, the frequency domain representation of incoherent imaging is (37)

$$\mathcal{I}_i(\vec{f}\,) = \mathcal{I}_o(\vec{f}\,)\mathcal{H}(\vec{f}\,) \tag{2.6}$$

where $\vec{f} = (f_x, f_y)$ is a spatial frequency vector. $\mathcal{H}$ in equation (2.6) is the optical transfer function, given by (37)

$$\mathcal{H}(\vec{f}\,) = \frac{\mathcal{F}\{|\mathbf{h}(\vec{x}_i)|^2\}}{\mathcal{F}\{|\mathbf{h}(\vec{x}_i)|^2\}_{\vec{f}=0}} \tag{2.7}$$

where $\mathcal{F}\{\cdot\}$ represents the Fourier transform.

The form of the optical transfer function can be derived if a point source object is used in equation (2.2). For a point source object, the resulting image will be the system impulse response. Referring again to the generalized imaging system model of Figure 2.1, the usual procedure is to assume that geometrical optics applies to the contents of the "black box." Under this assumption,

diffraction effects are entirely due to the entrance or exit pupil, whichever is smaller. Here it is assumed that the exit pupil is the smaller aperture, described by the pupil function $\mathbf{W_a}(\vec{x})$. If the exit pupil is preceded by a converging lens, and the distance d_i to the image plane satisfies the lens law, point source illumination will produce an image which is the Fraunhofer diffraction pattern of the exit pupil. This image is the impulse response function (25):

$$\mathbf{h}(\vec{x}_i - \vec{x}_o) = \int d^2\vec{x}\, \mathbf{W_a}(\vec{x}) \exp\left\{-j\frac{2\pi}{\lambda d_i}[(\vec{x}_i - \vec{x}_o)\cdot\vec{x}]\right\} \tag{2.8}$$

In the preceding equation, a constant multiplicative factor, which is of no consequence due to the normalized form of the OTF definition, has been neglected. With the following change of variables (25):

$$\vec{f} = \frac{\vec{x}}{\lambda d_i} \tag{2.9}$$

in equation (2.8), the impulse response function becomes, apart from constants (25):

$$\mathbf{h}(\vec{x}_i - \vec{x}_o) = \iint d^2\vec{f}\, \mathbf{W_a}(\lambda d_i \vec{f}) \exp\left\{-j2\pi[(\vec{x}_i - \vec{x}_o)\cdot\vec{f}]\right\} \tag{2.10}$$

Thus, the Fourier transform of $\mathbf{h}$ is $\mathbf{W_a}(\lambda d_i \vec{f})$. Applying the Fourier autocorrelation theorem to equation (2.7) leads to the well-known formula for the optical transfer function of a diffraction-limited imaging system (26):

$$\mathcal{H}(\vec{f}) = \frac{\mathbf{W_a}(\lambda d_i \vec{f}) \star \mathbf{W_a^*}(\lambda d_i \vec{f})}{\int d^2\vec{x}\, |\mathbf{W_a}(\vec{x})|^2} \tag{2.11}$$

where the operator $\star$ indicates correlation. This formula can also be used for systems that are not diffraction-limited by modifying the pupil function to account for aberrations in the optics or inhomogeneities in the intervening medium. For example, to obtain an OTF for a system consisting

of both atmosphere and optics, it is necessary to start with a new pupil function (26),

$$\mathbf{W}'_{\mathrm{a}}(\vec{x}) = \mathbf{W}_{\mathrm{a}}(\vec{x})\mathbf{t}(\vec{x}) \tag{2.12}$$

where the transmittance function $\mathbf{t}(\vec{x})$ accounts for the effects of the atmosphere. For astronomical imaging at a good observatory site, it may be assumed that the turbulence is close to the aperture, relative to the object distance, and sufficiently weak that diffraction and refraction may be ignored. Because of this assumption, phase delay is considered the only atmospheric effect of consequence, and the transmittance function is chosen to model phase disturbances only. Hence, $\mathbf{t}(\vec{x})$ can be written (26)

$$\mathbf{t}(\vec{x}) = \exp[j\psi(\vec{x})] \tag{2.13}$$

where ψ is the random phase perturbation.

Substituting equations (2.12) and (2.13) into the OTF formula leads to an expression for the instantaneous OTF of the turbulence-degraded system:

$$\mathcal{H}(\vec{f}) = \frac{\iint d^2\vec{x}\,\mathbf{W}_{\mathrm{a}}(\vec{x})\mathbf{W}^*_{\mathrm{a}}(\vec{x} - \bar{\lambda}d_{\mathrm{i}}\vec{f})\exp[j(\psi_1 - \psi_2)]}{\iint |\mathbf{W}_{\mathrm{a}}(\vec{x})|^2\,dx\,dy} \tag{2.14}$$

where

$$\begin{aligned} \psi_1 &= \psi(\vec{x}) \\ \psi_2 &= \psi(\vec{x} - \bar{\lambda}d_{\mathrm{i}}\vec{f}) \end{aligned} \tag{2.15}$$

To get the long exposure OTF, the usual procedure is to assume that $\psi(\vec{x})$ is an ergodic random process and find the ensemble average OTF, which is defined as the expected value of the numerator of equation (2.14) divided by the expected value of the denominator of equation (2.14) (26). Note that this definition is not the same as $\langle\mathcal{H}(\vec{f})\rangle$, but it contains the same information and is easier

to compute. With this definition, it is noted that the average OTF of the aberrated system can be written as the product of the OTF for the diffraction-limited system times

$$\overline{\mathcal{H}}_{\mathrm{L}}(\vec{f}) = \langle \exp[j(\psi_1 - \psi_2)] \rangle \tag{2.16}$$

which is called the long exposure OTF of the atmosphere (26). Here the angle brackets denote expectation.

The Rytov solution for propagation of an electromagnetic wave in a medium of inhomogeneous n (with the variation contained in the permittivity) predicts that $\psi(\vec{x})$ has Gaussian statistics. Based on this fact, and the fact that the phase fluctuations are zero-mean, it can be shown that

$$\overline{\mathcal{H}}_{\mathrm{L}}(f) = \exp\left[-\frac{1}{2}\mathcal{D}_{\psi}(\bar{\lambda} d_{\mathrm{i}} f)\right] \tag{2.17}$$

where $f = |\vec{f}|$ and

$$\mathcal{D}_{\psi}(r) = \left\langle [\psi(\vec{x}) - \psi(\vec{x} + \vec{r})]^2 \right\rangle \tag{2.18}$$

is the phase structure function discussed in Section 2.3. In writing $\mathcal{D}_{\psi}$ as a function of r, isotropic turbulence was assumed with $r = |\vec{r}|$.

As pointed out in the introduction to this chapter, the performance of an adaptive optical system, as measured by the OTF, is a function of the phase aberration function, $\psi(\vec{x})$, in the pupil plane. The objective of an adaptive optical telescope is to reduce $\psi(\vec{x})$ to 0 at all points in the aperture, thereby achieving the diffraction limited OTF. Other measures of optical system quality, the point spread function, resolution, and the Strehl ratio, are derivable from the OTF and thus also functions of $\psi(\vec{x})$.

2.2.2 Point Spread Function. The point spread function (PSF) is the inverse Fourier transform of the optical transfer function. The PSF describes the incoherent image of a point source.

For a diffraction-limited optical system with a circular exit pupil, the PSF is the familiar Airy pattern, $[2J_1(r)/r]^2$, where $J_1(\cdot)$ is the Bessel function of the first kind, order 1 (25).

2.2.3 Resolution. Optical system resolution may be evaluated in either the spatial or the spatial frequency domain. In the spatial domain, the Rayleigh criterion is often used. By this criterion, if the peak of the Airy pattern resulting from one object point is located on the first zero of the Airy pattern resulting from another object point, the two points are considered "barely resolved" by the system (25). Another spatial domain parameter is the full width at half maximum (FWHM) of the point spread function. Frequency domain measures of resolution include the cutoff frequency of the optical transfer function as well as the volume under the OTF (26).

2.2.4 Strehl Ratio. The Strehl ratio is defined as the ratio of the peak of the point spread function of an actual optical system to that of a diffraction-limited system. It is a measure of the additional spreading of the image intensity distribution due to aberrations in the optical system. To show how the Strehl ratio is related to the wavefront phase, Born and Wolf's derivation is presented in this section, with the aid of Hardy (7, 29).

Figure 2.2 depicts a perfectly spherical wave converging to an image point P. A diffraction-limited system would create such a wave from a perfectly spherical diverging wave that was received by its entrance pupil. The free-space Green's function describes this wave (25):

$$\mathrm{G}(R) = \frac{\exp(-jkR)}{R} \tag{2.19}$$

where R is the radius of the sphere and $k = 2\pi/\lambda$ is the wave number. Figure 2.2 also shows an aberrated wavefront which is displaced from the reference sphere by an amount ψ (rad), which is a function of position. If ψ is so small that the amplitude of the aberrated wave may be considered

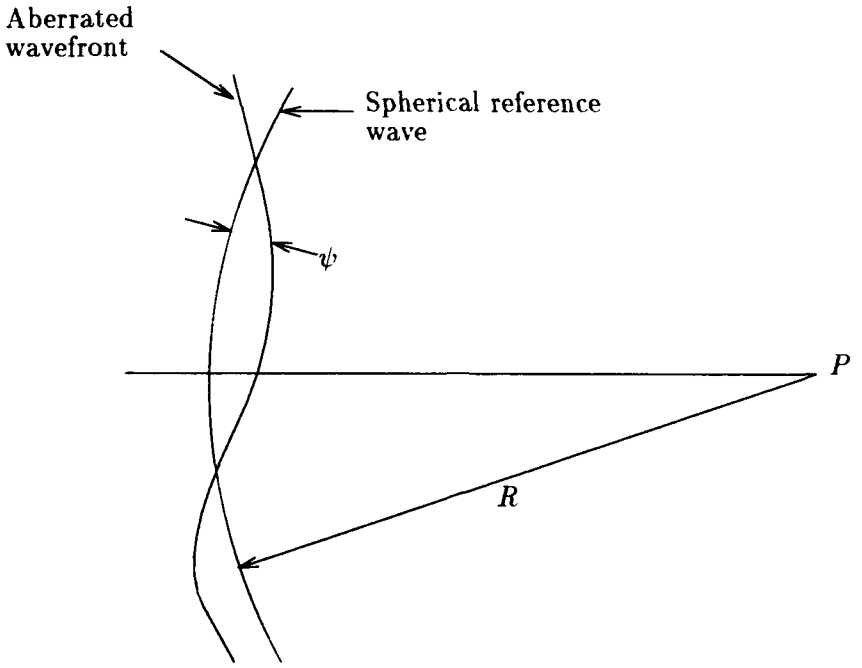

Figure 2.2. Aberrated wavefront (29).

constant, an expression for the field follows directly from equation (2.19):

$$\mathbf{G}_1(R) = A\frac{\exp[-j(kR-\psi)]}{R} \tag{2.20}$$

where A is the constant amplitude at unit distance from the source. The Huygens-Fresnel principle states that the field at point P may be considered as the resultant of an infinite number of point sources located on the portion of the aberrated wavefront enclosed by the exit pupil of the optical system. Hence, the field at P (the center of the reference sphere) may be found using the Rayleigh-Sommerfeld diffraction formula (25):

$$\mathbf{U}(P) = \frac{-jA}{\lambda}\frac{\exp(jkR)}{R^2}\int d^2\vec{x}\, W_{\mathbf{a}}(\vec{x})\exp\{-j[kR-\psi(\vec{x})]\} \tag{2.21}$$

the integration takes place over the exit pupil. From this point on in the dissertation, the pupil will be modeled by a real aperture weighting function $W_{\mathbf{a}}(\vec{x})$ normalized for mathematical convenience

such that

$$\int d^2\vec{x}\, W_a(\vec{x}) = 1 \tag{2.22}$$

Note in equation (2.21) that the diffraction angles are assumed small enough that the obliquity factor may be neglected. From equation (2.21), the intensity at point P follows (29):

$$I(P) = \left(\frac{A}{\lambda R^2}\right)^2 \left| \int d^2\vec{x}\, W_a(\vec{x}) \exp[j\psi(\vec{x})] \right|^2 \tag{2.23}$$

The intensity of an unaberrated system, $I_1(P)$, may be found by setting $\psi(\vec{x}) = 0$ (29):

$$I_1(P) = \left(\frac{A}{\lambda R^2}\right)^2 \tag{2.24}$$

Earlier in this section, the Strehl ratio was defined as the ratio of the intensity of the aberrated system to that of the diffraction-limited system,

$$S[\psi(\vec{x})] = \frac{I(P)}{I_1(P)} = \left| \int d^2\vec{x}\, W_a(\vec{x}) \exp[j\psi(\vec{x})] \right|^2 \tag{2.25}$$

Using the power series expansion for $\exp[j\psi(\vec{x})]$, the above expression can be rewritten (7):

$$S[\psi(\vec{x})] = \left| \int d^2\vec{x}\, W_a(\vec{x}) \left[1 + j\psi(\vec{x}) - \frac{1}{2}\psi^2(\vec{x}) + \ldots\right] \right|^2 \tag{2.26}$$

For small $\psi(\vec{x})$ (7),

$$S[\psi(\vec{x})] \approx \left| \left[1 + j\bar{\psi} - \frac{1}{2}\overline{\psi^2}\right] \right|^2 \tag{2.27}$$

where the overbar indicates the averages of $\psi(\vec{x})$ and $\psi^2(\vec{x})$ over the exit pupil (7):

$$\overline{\psi^n} = \int d^2\vec{x}\, W_a(\vec{x}) \psi^n(\vec{x}) \tag{2.28}$$

Expanding equation (2.27), and continuing to drop terms of higher than quadratic order, the Strehl ratio approximation becomes (7)

$$S[\psi(\vec{x})] \approx 1 - \left[\overline{\psi^2} - \bar{\psi}^2\right] \tag{2.29}$$

Defining ϵ^2 as the aperture average variance of the phase aberration function:

$$\begin{aligned} \epsilon^2 &= \int d^2 W_{\mathbf{a}}(\vec{x}) \left[\psi(\vec{x}) - \bar{\psi}\right]^2 \\ &= \overline{\psi^2} - \bar{\psi}^2 \end{aligned} \tag{2.30}$$

the Strehl ratio can be written

$$S(\epsilon^2) = 1 - \epsilon^2 \tag{2.31}$$

A second application of the series expansion for $\exp(x)$ yields the further approximation for small ϵ (22):

$$S(\epsilon^2) \approx \exp(-\epsilon^2) \tag{2.32}$$

with ϵ^2 (rad^2) being the total phase error variance of the optical system. Tyson points out that this formula is valid for $\epsilon < 1.25$ rad $\approx \lambda/5$ (59).

2.3 Atmospheric Optics

The previous section showed that several important measures of optical system quality are functions of the phase of the wavefront in the pupil plane. Consequently, the results of the adaptive optics system analysis of chapters III and IV are in terms of statistical averages of the random process $\psi(\vec{x})$. This section discusses the statistical properties of atmospheric phase distortion following a geometrical optics approach.

A wavefront, a useful concept in the discussion of atmospheric optics, is defined as a surface of constant optical path length orthogonal to a collection of rays (29). The light emanating from a source located in a medium of constant n propagates with spherical wavefronts. At a sufficient distance from the source, the wavefront may be considered planar.

The index of refraction of the atmosphere is a random function of position, as well as time and wavelength. Since, in a geometrical optics framework, optical path length between two points A and B is equal to the path integral of n (7),

$$(\text{O.P.L.}) = \int_A^B ds\, n(s) \tag{2.33}$$

it is found that initially planar wavefronts become distorted as they pass through the atmosphere. This distortion is described by a two-dimensional function of position, $\psi(\vec{x})$, which goes by various names in the literature such as wavefront aberration function (4) or waveheight function (45). Following most authors, this dissertation will frequently use the term "phase" as a shorthand nomenclature for $\psi(\vec{x})$, since it is understood that an absolute phase measurement is never implied. The following sections present the statistical quantities used to characterize optical turbulence and aberrated wavefronts.

2.3.1 Refractive Index Power Spectrum. The refractive index power spectrum, $\Phi_n(\vec{\kappa})$, is a measure of the strength of the optical turbulence at a point in space as a function of spatial frequency. The argument $\vec{\kappa} = (2\pi/l_x, 2\pi/l_y, 2\pi/l_z)$ is a wave number vector indicating the scale size of pockets of air, with dimensions $l_x \times l_y \times l_z$, inside which n is considered to be approximately constant. These pockets of air are called eddies; large eddies correspond to small values of $\vec{\kappa}$ while small scale turbulence implies large $\vec{\kappa}$. Φ_n may be interpreted as the relative abundance of different size eddies (26).

The formation of these eddies begins with uneven heating of large volumes of air due to the position of the sun and different types of underlying terrain. These large volumes of air are broken up into eddies of various sizes by mechanical turbulence. The resulting random distribution of pockets of air having slightly different temperatures is the underlying cause of atmospheric distortion. The reason for this phenomenon is that the index of refraction, while a function of temperature, pressure, humidity, and wavelength, is more sensitive to variations in temperature than to changes in the other parameters (33). When the term turbulence is used in the context of optical imaging, it is the three-dimensional random process of temperature (or index of refraction) that is being referred to. Mechanical turbulence itself actually has relatively little effect on imaging.

The most commonly used form of Φ_n, based on the work of Kolmogorov (42), is given by (26):

$$\Phi_n(\kappa) = 0.033 C_n^2 \kappa^{-11/3} \tag{2.34}$$

where C_n^2 is the structure constant discussed in the next section and isotropic turbulence is assumed ($\kappa = |\vec{\kappa}|$). This expression is valid for an intermediate range of scale sizes called the inertial subrange; it does not describe the refractive index structure that results from very large or very small inhomogeneities because the physical laws used to derive equation (2.34) do not govern the formation of eddies of these sizes. The inertial subrange is the region in which energy is transferred from large to small eddies without appreciable loss. The boundaries for which the Kolmogorov spectrum is valid are known as the inner scale, on the order of a few millimeters, and the outer scale, which may be as large as 100 meters (26). This range of validity is not of great concern, since scale sizes larger than the optical aperture will cause a uniform, as opposed to randomly varying, optical path length change across the area of the wavefront intercepted by the aperture. A uniform value of phase across the aperture has no effect on the imaging system, since it does not represent a deformation of the received wavefront. As for the inner scale of the turbulence, even if the ability to

correct for the very high spatial frequency, but low power, deformations that result from microscale turbulence were available, it would yield a virtually indiscernible improvement in image quality.

2.3.2 Refractive Index Structure Constant. The term "refractive index structure constant" can lead to confusion, since C_n^2 is in fact a function of geographical location and altitude. An indication of the strength of the optical turbulence, the refractive index structure constant is measured in units of meters$^{-2/3}$ (26). Experimental data reveals that the value of C_n^2 is highly variable with altitude. For this reason, combined with its dependence on geographical location, the structure constant is difficult to characterize. For analytical purposes, however, C_n^2 is often set to a uniform value over a finite altitude range.

Hufnagel presents two additional C_n^2 profiles to aid in propagation calculations in cases where a uniform model would be too simplistic (33). A simple model, in terms of altitude h in meters above local ground, is

$$C_n^2(h) = \begin{cases} \frac{1.5 \times 10^{-13}}{h} & \text{below 20,000 m above sea level} \\ 0 & \text{above 20,000 m above sea level} \end{cases} \tag{2.35}$$

In the preceding profile, local ground is assumed to be < 2500 m above sea level. Equation (2.35) models one of the notable features of empirical C_n^2 data, which show that the turbulence is strongest near the ground and generally decreases with altitude. A more complicated formula, known as the Hufnagel model, captures a second C_n^2 characteristic—a peak in the turbulence strength in the neighborhood of the tropopause:

$$C_n^2(z) = 8.2 \times 10^{-56} v^2 z^{10} \exp(-z/1000) + 2.7 \times 10^{-16} \exp(-z/1500) \tag{2.36}$$

where v (m/sec) is the rms wind speed averaged between 5000 and 20,000 meters and z (m) is the altitude above sea level. Strictly speaking, the Hufnagel model is only valid above the first strong

inversion layer (33), however it is often used as a sea level to 20,000 meter profile as shown in the plot in Figure 2.3.

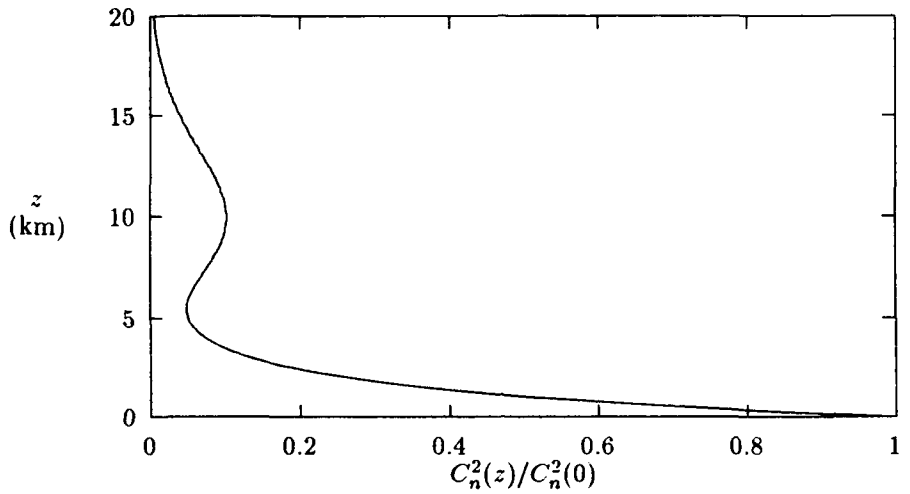

Figure 2.3. Hufnagel model for $v = 27$ m/sec.

2.3.3 Phase Structure Function. According to equation (2.34), the functional form of the Kolmogorov refractive index power spectrum has a nonintegrable pole at the origin, implying an infinite variance. Hence, a corresponding autocorrelation function cannot be defined. For this reason, structure functions are often used to describe statistical quantities in atmospheric optics. The structure function of a general random process $Z(\vec{r})$ is defined as (26)

$$\mathcal{D}_Z(\vec{r}_1, \vec{r}_2) = \left\langle [Z(\vec{r}_1) - Z(\vec{r}_2)]^2 \right\rangle \tag{2.37}$$

For homogeneous and isotropic Kolmogorov turbulence and vertical viewing, the refractive index structure function, $\mathcal{D}_n$, is found to be (26)

$$\mathcal{D}_n(r) = C_n^2 r^{2/3} \tag{2.38}$$

Note that $\mathcal{D}_n$ is finite for path length separations near zero.

In this dissertation, the phase structure function, $\mathcal{D}_\psi$, is used in the analysis of Chapter IV. The derivation of the phase structure function is mathematically complex (26). The procedure, shown in Figure 2.4, is to calculate the optical path length for two parallel rays traversing the atmosphere and separated by a distance r. The formula (2.33) is used to obtain expressions for the

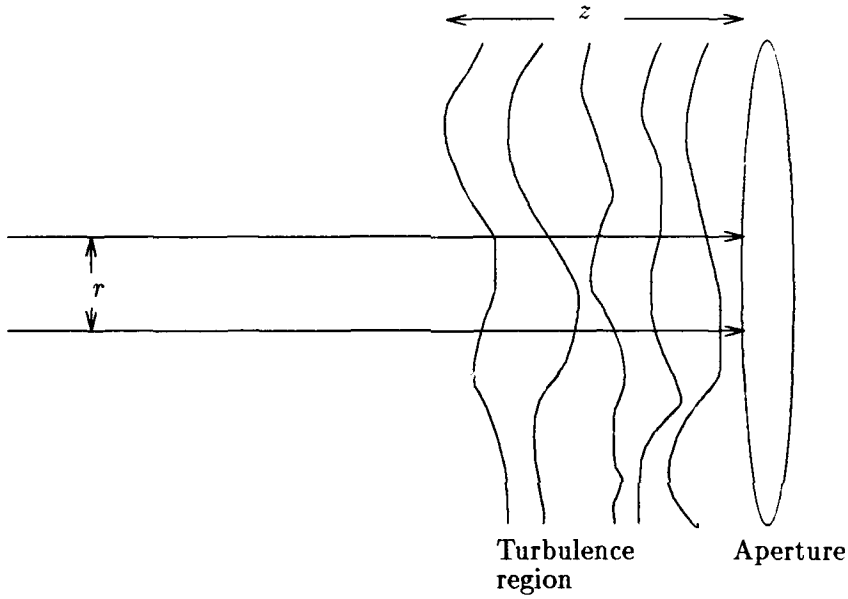

Figure 2.4. Procedure used to calculate phase structure function (26)

two phases, ψ_1 and ψ_2, in terms of the random index of refraction. Using these results, $\mathcal{D}_\psi$ can be found in terms of $\mathcal{D}_n$, which in turn is obtainable from Φ_n. For isotropic Kolmogorov turbulence, the final result is (26)

$$\mathcal{D}_\psi(r) = 2.91\bar{k}^2 r^{5/3} \int_0^z d\xi \, C_n^2(\xi) \tag{2.39}$$

where $\bar{k}$ is the average wave number of the light and z is the thickness of the turbulence region. The above result is valid for path separations r within the inertial subrange, a restriction that is usually of no consequence for the reasons mentioned at the end of Section 2.3.1. Also notice that equation (2.39) shows that it is the integrated turbulence strength which is of importance for propagation calculations.

By substituting equation (2.39) into equation (2.17), the formula for the average long exposure OTF of the atmosphere for Kolmogorov turbulence is obtained (26):

$$\overline{\mathcal{H}}_{\mathrm{L}}(f) = \exp\left[-57.4(d_{\mathrm{i}}f)^{5/3}\bar{\lambda}^{-1/3}\int d\xi\, C_n^2(\xi)\right] \tag{2.40}$$

2.3.4 Atmospheric Coherence Diameter. As illustrated in Figure 2.5, optical rays separated laterally by more than a few centimeters cross different collections of turbulent eddies, resulting in deformation in the wavefront. As might be expected, the turbulence scale size results in the wavefront phase at two points being correlated to some degree if the points are close together and uncorrelated if the points are widely separated. Fried derived a measure of the area over which the phase is nominally correlated (17, 18). This quantity, designated r_0, is known as the Fried parameter or atmospheric coherence diameter.

The analysis which leads to the definition of r_0 begins with the calculation of the long exposure transfer function of a circular aperture imaging through turbulence. The diffraction-limited OTF of a circular aperture of diameter D is given by (18):

$$\mathcal{H}_0(f) = \begin{cases} \frac{2}{\pi}\left[\cos^{-1}(\bar{\lambda}d_{\mathrm{i}}f/D) - (\bar{\lambda}d_{\mathrm{i}}f/D)\sqrt{1-(\bar{\lambda}d_{\mathrm{i}}f/D)^2}\right] & \bar{\lambda}d_{\mathrm{i}}f \le D \\ 0 & \bar{\lambda}d_{\mathrm{i}}f > D \end{cases} \tag{2.41}$$

By multiplying transfer function (2.40) by (2.41), the long exposure OTF of a circular aperture imaging through Kolmogorov turbulence is obtained. One measure of resolution for the turbulence-degraded system is the volume under the OTF. (By Fourier theory, it is also equal to the peak of the PSF, which is equivalent to a Strehl ratio measure.) Fried found that by taking the limit of the integrated OTF as D goes to infinity, this resolution approached a maximum value. Fried then defined r_0 as the diameter of an equivalent diffraction-limited telescope with this same value of resolution. It is a function of wavelength and the optical turbulence strength integrated over the

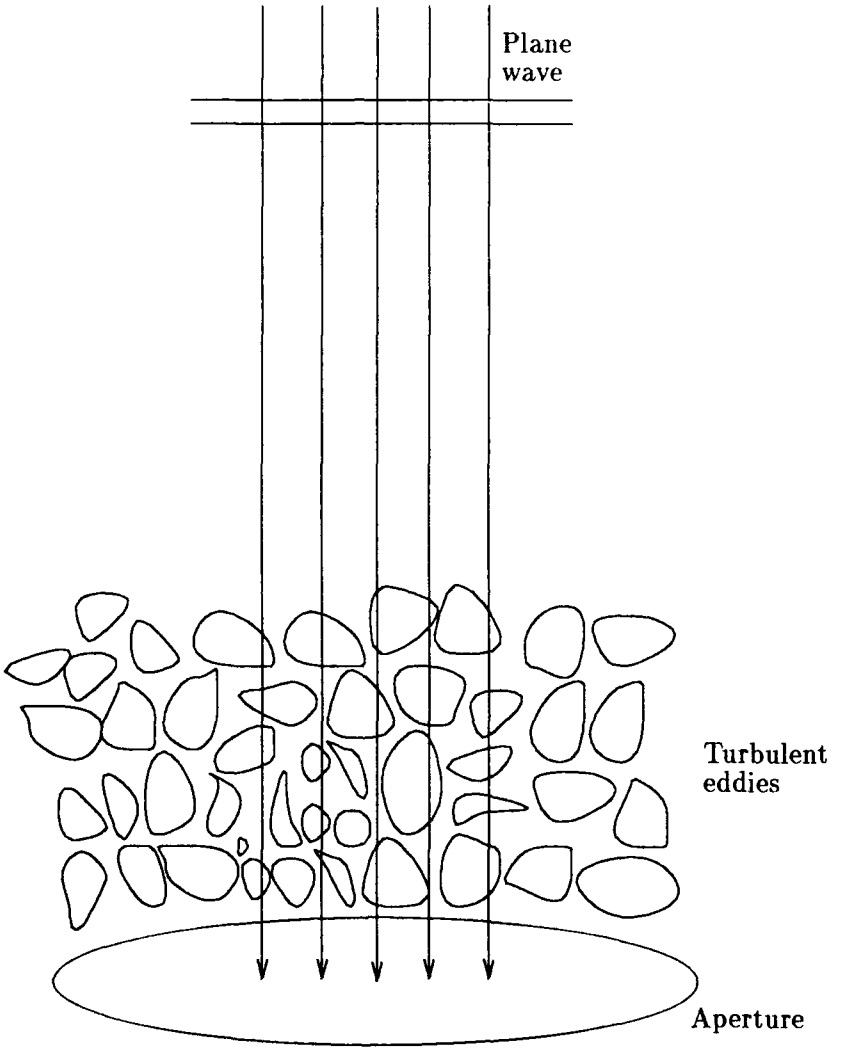

Figure 2.5. Optical paths separated by an amount greater than the scale size of the turbulence traverse different collections of eddies. Hence, the degree of correlation between the phase change experienced by two different rays depends on their path length separation.

optical path (26):

$$r_0 = 0.185 \left[\frac{\bar{\lambda}^2}{\int_0^z d\xi \, C_n^2(\xi)} \right]^{3/5} \tag{2.42}$$

where the overbar indicates an average value and z is the thickness of the turbulence region. Thus, r_0 is often more useful than Φ_n or C_n^2 in that, as a single number, it characterizes atmospheric turbulence conditions. Fried has shown how r_0 can be interpreted as a measure of the limiting resolution of an optical system imaging through a random medium (18). Specifically, regardless of the actual aperture size, the resolution of a telescope looking through the atmosphere is approximately that of a diffraction-limited telescope of diameter r_0. (Astronomers still build large telescopes to gather more light from the object of interest, thereby increasing signal to noise ratio.) This limitation is quite severe, typical values of r_0 range from less than 5 cm for poor observing or "seeing" conditions to 20 cm if the seeing is "exceptionally good (26)." Measurement of r_0 is a useful parameter for evaluation of potential observatory sites. With the preceding definition of r_0, the formula for the Kolmogorov phase structure function simplifies:

$$\mathcal{D}_\psi(r) = 6.8839 \left(\frac{r}{r_0} \right)^{5/3} \tag{2.43}$$

2.3.5 Phase Power Spectrum. The frequency domain analogue to the phase structure function is the phase power spectrum (48):

$$\Phi_\psi(f) = \frac{0.023}{r_0^{5/3} f^{11/3}} \tag{2.44}$$

This function is plotted in Figure 2.6 for several values of r_0. From inspection of the figure, it is clear that most of the power in the phase fluctuations is contained in the lowest spatial frequencies. At a good observatory site, one would expect r_0 to be ≥ 0.05 most of the time. Even for this "moderately poor" value of r_0, there is very little power in the phase fluctuations at spatial frequencies above

5 cycles per meter. This observation provides support for the assumption that geometrical optics adequately models propagation down through the atmosphere at a good observatory site. It has been shown that Fresnel propagation can be described by a transfer function (25):

$$\mathbf{H}(f) = \exp(-j\pi\lambda z f^2) \tag{2.45}$$

where k is the wave number, z is the propagation distance, and a constant phase delay term has been suppressed. If the argument of this transfer function is plotted out to a spatial frequency of 5 cycles per meter, as shown in Figure 2.7, it is seen that the quadratic phase dispersion is insignificant for the spatial frequencies and propagation distances of interest. In studying Figure 2.7, keep in mind that the strongest turbulence is at the lowest altitudes, usually within $\sim$ 1 km of the telescope. For this propagation distance, the phase dispersion is of the order of $\lambda/100$ or less. For this reason, as well as the demonstrated success of phase-only correction in adaptive optics systems, virtually all adaptive optics calculations in the literature are based on geometrical optics.

2.4 Adaptive Optics Imaging Systems

An adaptive optics system performs two main functions: wavefront sensing and wavefront correction. The next two sections discuss these functions in the context of a telescope aperture with diameter D larger than the atmospheric coherence diameter r_0. For such a telescope, one may think of the aperture as divided up into $\sim D^2/r_0^2$ subapertures. In each of these subapertures, the wavefront deviates from a plane, having a nonzero slope (tilt), curvature, and higher derivatives. The objective of current wavefront sensing and correction techniques is to sample the wavefront in the aperture with a period $\leq r_0$, measure the subaperture tilts, and reconstruct an estimated wavefront which would produce the measured slopes.

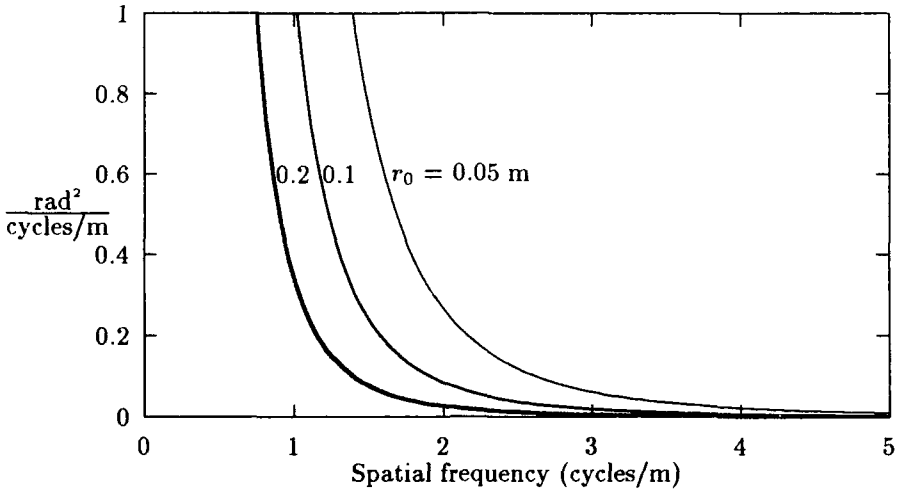

Figure 2.6. Phase power spectrum for several values of r_0.

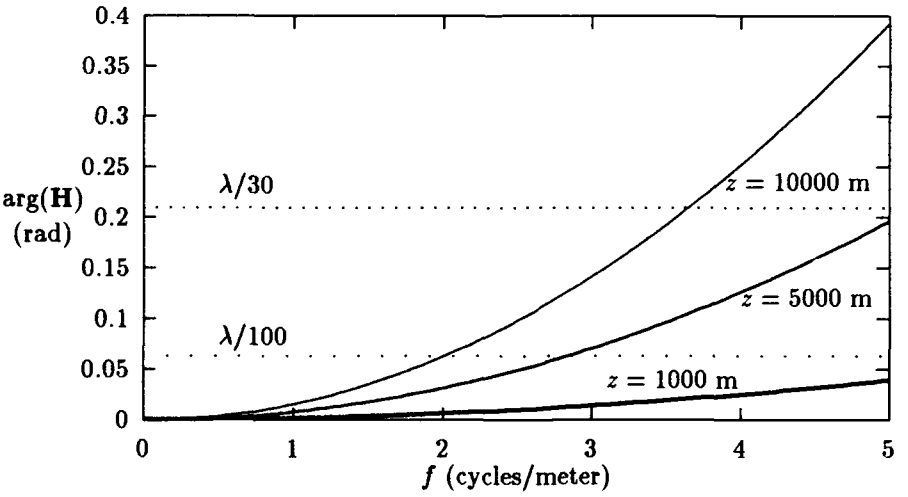

Figure 2.7. Argument of Fresnel transfer function for several propagation distances z (λ = 500 nm.)

Following the sections on wavefront sensing and correction, Section 2.4.3 describes some of the sources of error in adaptive optics systems. Finally, Section 2.4.4 reviews some of the latest experiments.

2.4.1 Wavefront Sensing. For a phase correcting adaptive optics system, the WFS must determine the wavefront deviation from an ideal plane. There is no need to determine the mean phase (known in the adaptive optics community as "piston") since it has no effect on the image.

The most common WFS discussed in the literature is the Hartmann-Shack (H-S) WFS. Shown in Figure 2.8, the H-S WFS consists of a lenslet array and a charge-coupled device (CCD) grid in the focal plane of the lenslets. The H-S WFS requires an unresolved point source for best results.

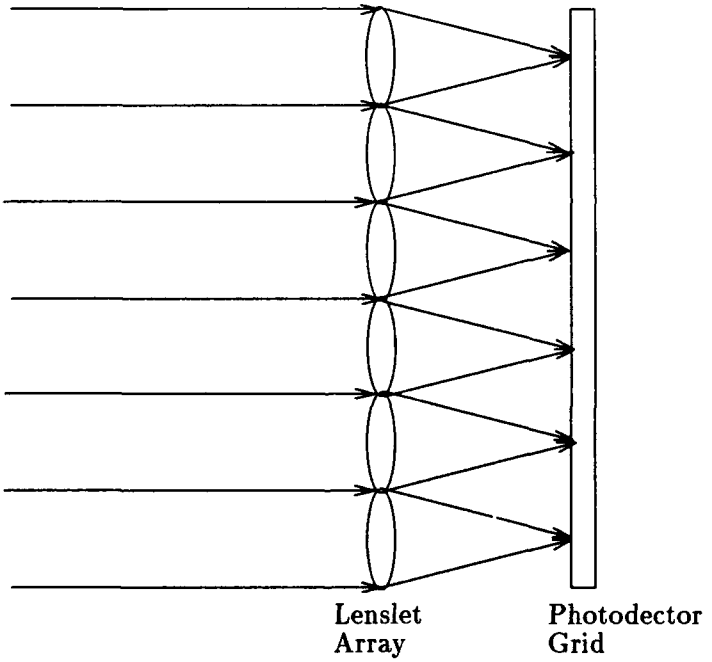

Figure 2.8. Hartmann-Shack WFS.

If the lenslets are of smaller diameter than r_0, they will focus a diffraction-limited spot on the CCD photodetectors. From the displacement of the spot from its ideal position, the local wavefront slope can be calculated.

2.4.2 Wavefront Correction. At this time, the most common high-bandwidth wavefront correction device is the continuously deformable mirror. The surface of the DM is perturbed to fit, as much as possible, the original aberrated wavefront. The relative amount of mirror surface deflection caused by a single aperture, as a function of distance from the actuator's position, is called the actuator influence function (29) or mirror response function (63).

The simplest type of DM is a thin plate which is deformed using an arrangement of electromechanical, electromagnetic, or piezoelectric actuators. Thin plate DMs have a wide influence function which may overlap that of several other actuators, complicating the mirror control problem (29).

A type of mirror with a narrower influence function is a monolithic mirror which incorporates the reflector surface, actuators, and rigid backplate in one block of material (29). In fact, the interactuator coupling for Litton/Itek's monolithic piezoelectric mirror (MPM), used at the Air Force Maui Optical Site (AMOS), can be adjusted from 0 to 20% (12).

A third type of DM with a continuous reflecting surface is the membrane mirror. Tension is maintained on the membrane to keep it flat, and its surface is deformed with electrostatic forces. The interesting property of the membrane mirror is that the force F necessary to achieve a given displacement Z at a distance r from the center is proportional to the Laplacian of the displacement (10):

$$\nabla^2 Z = -\frac{F(r,t)}{T} \tag{2.46}$$

where ∇^2 is the Laplacian operator, t is time, and T is the tension/length. Roddier has proposed a wavefront curvature sensor which measures the Laplacian of the wavefront over a subaperture instead of its slope (53). Its output could be applied directly to a membrane mirror with no wavefront reconstruction necessary. The mirror itself would perform the reconstruction since it solves Poisson's equation (equation (2.46)). Such a scheme is also possible with bimorph mirrors, which are constructed by gluing the reflective surface to a piece of piezoelectric material sandwiched between electrodes (56).

In addition to continuous facesheet DMs, there is renewed interest in segmented mirrors. Each segment of this type of mirror is independently controllable with three degrees of freedom: tip, tilt, and piston; there is no problem with influence functions cross coupling with other segments (34).

2.4.3 Sources of Error in Adaptive Optics Systems. The four chief causes of systemic error in adaptive optics systems are measurement noise and sampling error, associated with the WFS; fitting error, associated with the DM; and time delay error, associated with the control loop. The residual aperture-average phase variance associated with each of these error sources (rad^2 or waves^2) is designated σ_n^2, σ_s^2, σ_f^2, and σ_τ^2, respectively. If these errors are uncorrelated, the total error due to system imperfections, σ_t^2, can be found by summing the variances:

$$\sigma_t^2 = \sigma_n^2 + \sigma_s^2 + \sigma_f^2 + \sigma_\tau^2 \tag{2.47}$$

Some integrated system analyses have shown that the combined effect of various error sources is less than that indicated by the quadrature sum (14). This systemic wavefront variance is in addition to residual phase error due to anisoplanatism (59).

2.4.3.1 Measurement Noise. WFS measurement noise arises from two primary sources: photon noise and detector noise. Photon noise is a problem when WFS measurements are made at low signal levels. The fewer the number of photons collected by the subaperture per integration time, the less accurate will be the estimate of the centroid of the focused spot. In fact, the wavefront phase measurement error variance due to photon noise is inversely proportional to the number of photons per subaperture per integration time, N_{ph}:

$$\sigma_n^2 = \frac{k_n}{N_{ph}} \qquad ((\text{rad/subaperture})^2) \tag{2.48}$$

Researchers differ as to the exact value of the proportionality constant k_n for a H-S WFS. Lincoln Laboratory researchers give 26.1 as a typical value (46), Kern *et al.* use 19.7 (41), Genrui *et al.* report 12.2 (24), which is close to the value of 13.4 used by Gardner *et al.* in their calculations (22).

Previous analyses of adaptive optics often assumed photon-limited detectors, that is, they assumed that photon noise dominates. However, in practice, Lincoln Laboratory researchers have found that detector noise dominates. Detector noise may be accounted for by adding a second term, proportional to N_{ph}^{-2}, to equation (2.48).

2.4.3.2 Sampling Error. If the WFS subapertures were vanishingly small, the wavefront could be measured with perfect accuracy, assuming no measurement noise. However, due to the finite size of actual subapertures, coupled with the fact that only the wavefront tilt is measured, there will be residual wavefront error resulting from the sampling process even in noise-free conditions. The appropriate Zernike-Kolmogorov residual error formula derived by Noll gives σ_s^2 for a WFS that measures tilt (48):

$$\sigma_s^2 = 0.134 \left(\frac{d}{r_0}\right)^{5/3} \qquad (\text{rad}^2) \tag{2.49}$$

where d (m) is the subaperture diameter.

2.4.3.3 Fitting Error. The term "fitting error" describes the inability of the DM to perfectly match the reference wavefront, due to the mirror's finite number of degrees of freedom. Hudgin gives a general expression for this type of error (32):

$$\sigma_f^2 = k_f \left(\frac{L}{r_0}\right)^{5/3} \qquad (\text{rad}^2) \tag{2.50}$$

where L (m) is the distance between actuators. The constant k_f depends on actuator geometry and influence functions. Hudgin calculated a value of $k_f = 1.302$ for a square array of piston-only segments while Tyson lists a value of 0.2 for a new type of DM (59).

2.4.3.4 Time Delay Error. During the WFS integration time, combined with the time required for wavefront reconstruction and mirror response, the optical turbulence structure changes slightly. A rule of thumb for time delay error is

$$\sigma_\tau^2 = k_\tau \left(\frac{v\tau}{r_0}\right)^{5/3} \qquad (\text{rad}^2) \tag{2.51}$$

where v (m/s) is the transverse wind velocity and τ (s) is the time delay. In this case, the proportionality constant is a function of the control algorithm (59).

2.4.4 Experimental Results. Evidently, the first diffraction-limited images obtained with an adaptive optics system were made in January, 1976, using a technique called image sharpening (8, 9). The device used was a 30 × 5 cm aperture telescope which employed a linear arrangement of six piston-adjustable mirrors to maximize the intensity of light passing through a narrow slit. The system required bright objects and atmospheric coherence times > 7–8 ms. One dimensional images of the stars Sirius and Arcturus were recorded at visible wavelengths.

Conducting research for the U.S. military, the Massachusetts Institute of Technology Lincoln Laboratory began adaptive optics research in the 1970s. In 1982, the first compensated star images were made using the Compensated Imaging System at AMOS, which employs a 168-actuator MPM (28). Performance details for this system have still not been published (31).

It was not until October, 1989, that the first diffraction-limited photographs of an astronomical object were produced by civilian astronomers (55). The components of this prototype system included a 1.52 m aperture, an H-S WFS with 5×5 subapertures, a DM with 19 actuators, and a

tip-tilt mirror for overall tilt compensation. Images of Polaris, binary stars, and a satellite were made using infrared light, with the best results at wavelengths $> 2.2\mu$m.

2.5 Laser Guide Stars

As discussed in Section 2.4.3.1, WFS measurement noise for a photon-limited detector is inversely proportional to the number of detected photons per subaperture. This result implies that there is a minimum required level of brightness for a reference source to be suitable for WFS measurements. An additional requirement for a WFS reference source is that it be located very close to the object of interest, so that the light from the reference travels through the same atmospheric turbulence structure as the light from the object. It turns out that these two requirements are so stringent at visible wavelengths that adaptive optics can only be used to compensate a few of the brightest natural stars. For adaptive optics to be useful to astronomers, a means of generating a suitable WFS reference source at any desired location is necessary. A layer of sodium (Na) atoms, evidently the result of meteoric ablation, resides in a region of the atmosphere known as the mesosphere at an altitude of approximately 92 km (58). These atoms can be made to fluoresce when stimulated by a laser operating at a wavelength of 589 nm. In 1985, Foy and Labeyrie, unaware of ongoing (at the time, classified) military research, first proposed to the astronomical community the concept of using laser stimulation of the Na layer to generate reference beacons for wavefront sensing (15). They also suggested using Rayleigh scattered laser light from molecules in denser, lower altitude regions of the atmosphere.

There are three problems, directly related to the guide stars themselves, facing the designer of a laser guided adaptive telescope: guide star brightness, guide star size, and anisoplanatism. The brightness requirement translates to a laser power requirement, which is currently the most significant technological limiting factor for this type of telescope. For the most accurate WFS measurements, the laser guide stars should be as small as natural stars, that is, they should be

appear to the telescope as an unresolved point source (angular radius $\leq 1.22\lambda/r_0$) (58). In order to approach this goal as close as possible, the laser itself may be projected through the adaptive telescope where it is precompensated by the DM (22).

Anisoplanatism causes two deleterious effects which must be accounted for in the design of a laser-guided adaptive optics system. The first effect results from the finite height of the reference stars. As shown in Figure 2.9, there is an angular separation, α, between the optical paths from the reference and object for virtually all points in the aperture. (In this figure, the object is assumed to be a point source.) This effect is known as focus anisoplanatism, because the rays from the beacon and object seem to focus at different points. It is anticipated, but not yet demonstrated, that focus

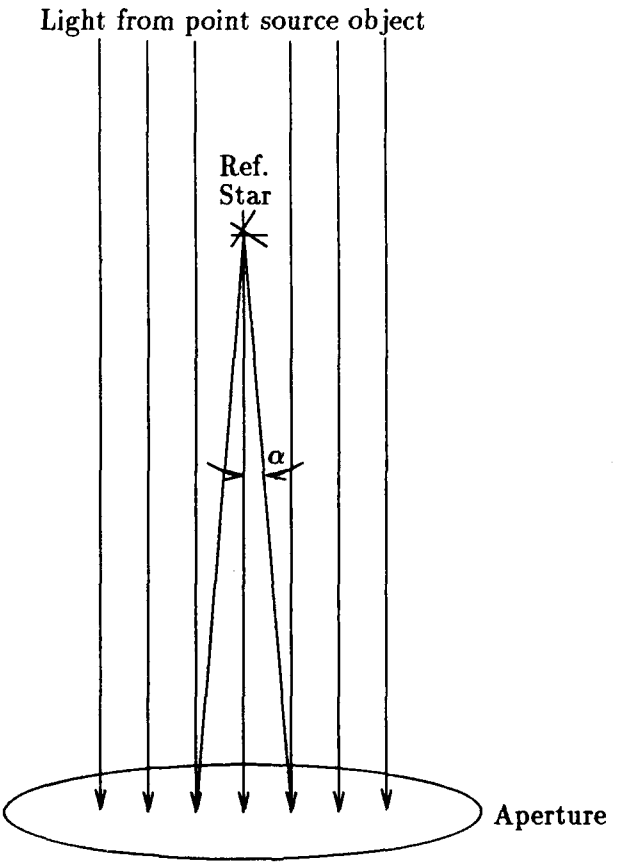

Figure 2.9. Focus anisoplanatism due to finite height of guide stars.

anisoplanatism can be mitigated through the use of multiple guide stars; the required number is determined via an analysis such as that recently completed by Welsh and Gardner (64). The second

problem, which is investigated in this dissertation, is depicted in Figure 2.10. In this case, plane

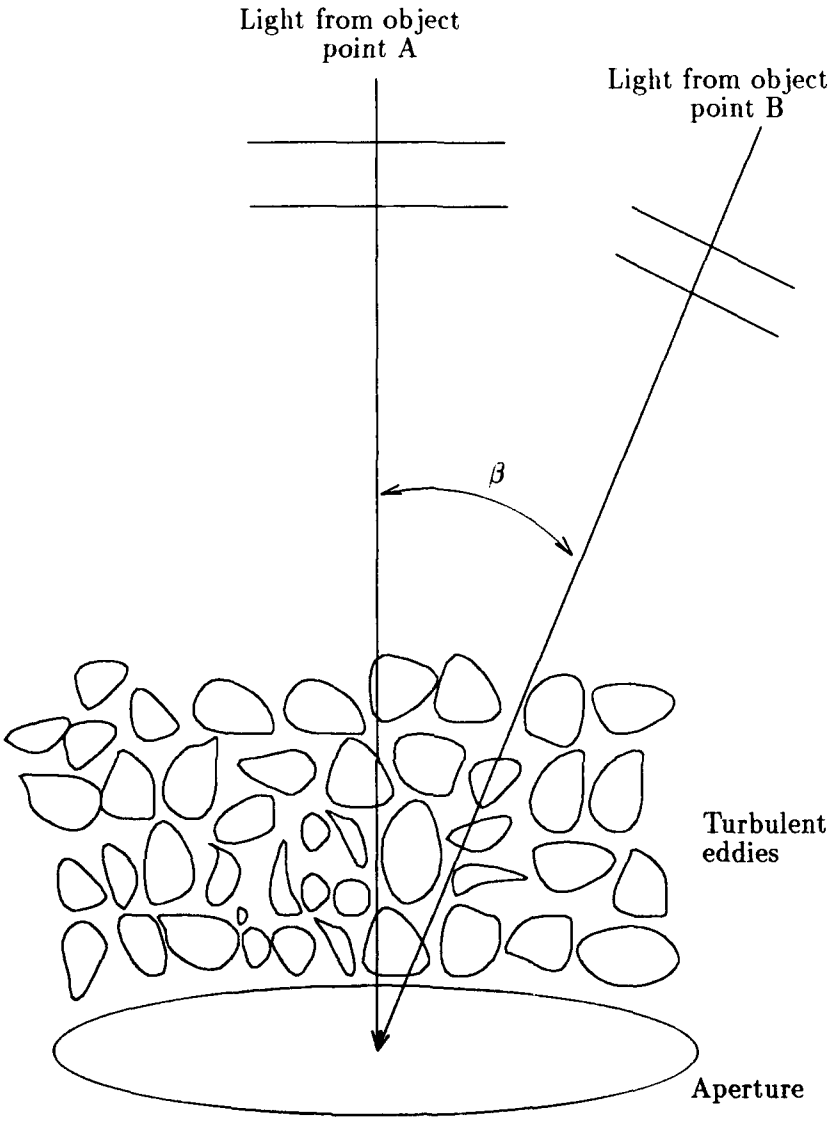

Figure 2.10. Illustration of FOV problem: Two object points are separated by an angle β, which may be greater than the isoplanatic angle.

waves from the object, now an extended source, arrive from various angles, thus traversing different regions of turbulence than the plane wave perpendicular to the telescope axis. Hence, even though an adaptive optics system with a single DM may employ a constellation of guide stars to correct the entire aperture, such correction is only effective for the on-axis plane wave and those from points

with zenith angles less than approximately the isoplanatic angle. Note that this FOV problem is also applicable to adaptive telescopes which use natural stars for wavefront sensing.

2.5.1 Experimental Results. As of April, 1991, as far as the general optics and astronomical communities knew, a laser guide star adaptive telescope for visible light was still a futuristic concept. Thompson and Gardner had demonstrated the laser guide star concept in 1987 (58), while, as discussed in Section 2.2, European astronomers had obtained diffraction-limited infrared imagery in 1989 (55). These two accomplishments represented the state of the art until, in May, 1991, the Air Force declassified the results of a decade of research (20, 50). They announced the development of a 1.5-meter laser guided adaptive telescope with which a number of turbulence-compensated astronomical images have been obtained.

In 1983, researchers at the USAF Phillips Laboratory made the first wavefront measurements using Rayleigh backscattered laser light (20). By comparing the wavefront measurements using the laser guide star with those made simultaneously with the star Polaris, the utility of the laser guide star concept was demonstrated. These experiments were also used to validate the theory which predicted the magnitude of the focus anisoplanatism error.

In 1984–1985, similar experiments were conducted by Lincoln Laboratory using sodium guide stars (35). This experiment provided the first empirical data showing that focus anisoplanatism is less severe for a sodium guide star than for a lower-altitude Rayleigh guide star.

Thompson and Gardner were the first civilian researchers to field test the laser guide star concept (58). In 1987, they produced and imaged a Na guide star with an apparent brightness of $M_v = 14.4$ on the visual magnitude scale used by astronomers. This guide star was not bright enough for wavefront sensing and no attempt was made to achieve the guide star size criterion.

The first astronomical images compensated using a laser guide star were produced in 1988 by Lincoln Laboratory at AMOS (50). They compensated a 60 cm telescope with an open-loop adaptive optics system consisting of 256-subaperture Hartmann WFS, a 241 actuator DM, and a

Rayleigh guide star at an altitude of 4–8 km. The column of air used for the synthetic beacon was 0.75–1.5 km long. Measured Strehl ratios for the star Procyon averaged ~ 0.3 at visible wavelengths vs. ~ 0.05 with no adaptive optics compensation.

In 1989, researchers at the Phillips Laboratory achieved closed loop adaptive optics compensation on a 1.5 m telescope using a guide star range of 10 km (20). Full-width-half-maximum resolution of 0.18 arcsec at visible wavelengths was achieved in 2 arcsec seeing conditions. This level of improvement allowed the two stars of the binary star system 53 ξ Ursa Majoris (separation 1.3 arcsec) to be resolved in a 1-second exposure.

The latest significant development occurred in 1990, when the first multiple synthetic beacon adaptive optics system was demonstrated (65). In this experiment, the wavefront measurements from two Rayleigh guide stars were combined to compensate an image of the star Pollux. Because only a 60-cm aperture was used, the reduction in focus anisoplanatism was not apparent. However, this experiment served to demonstrate the feasibility of multiple guide star systems.

2.6 Summary

Over the past several decades, techniques for rigorous analysis of the problem of imaging through the atmosphere have been developed, refined, and validated with experimental results. Meanwhile, advances in electronic and optical hardware have resulted in successful application of this theory to obtain nearly diffraction-limited resolution, over small fields, with ground-based telescopes. Increasing the corrected field of view of these telescopes is one of the next major problems of interest to the community. A detailed analysis of this problem begins with the next chapter.

III. Frequency Domain Analysis

3.1 Introduction

In this chapter the problem of estimating the contributions of different parts of the atmosphere to optical wavefront aberration is addressed from a frequency domain point of view. Motivation for a frequency domain analysis stems from Beckers' suggestion that the contribution of a particular layer of the atmosphere to the total phase may be estimated as a linear combination of weighted and shifted wavefront measurements (5). By transforming into the frequency domain, the spatial shifts become multiplicative complex exponentials. The result is a linear system of equations with the layer contributions as unknowns. If the number of measurements equals the number of turbulent layers, the system may be inverted to obtain the layer contributions. Using Figure 3.1, this approach will be illustrated for the case of a 2-layer atmosphere with noise-free measurements.

In this chapter, it is assumed that the WFS can directly measure the total phase aberration function in the aperture plane, $\psi_{t_m}(\vec{x})$, where m indicates the reference source (guide star). In the example illustrated in Figure 3.1, two such measurements are made, first with guide star 1 and then with guide star 2. It is assumed that the atmosphere does not change at all during the time it takes to make the two measurements. Using geometrical optics and assuming the guide stars are at an infinite altitude, the two measurements may be written

$$\psi_{t_1}(\vec{x}) = \psi_{l_1}(\vec{x} + z_{l_1}\vec{\theta}_1) + \psi_{l_2}(\vec{x} + z_{l_2}\vec{\theta}_1) \tag{3.1}$$

$$\psi_{t_2}(\vec{x}) = \psi_{l_1}(\vec{x} + z_{l_1}\vec{\theta}_2) + \psi_{l_2}(\vec{x} + z_{l_2}\vec{\theta}_2) \tag{3.2}$$

where $\vec{\theta}_m$ is the angular position of guide star m, z_{l_i} is the altitude of turbulent layer i, and $\psi_{l_i}(\vec{x})$ is the contribution of turbulent layer i to the total phase aberration. Throughout this dissertation, this contribution is referred to as wavefront "component" i. Note that a small angle approximation was used in writing the preceding equations. Transforming the this system of equations into the

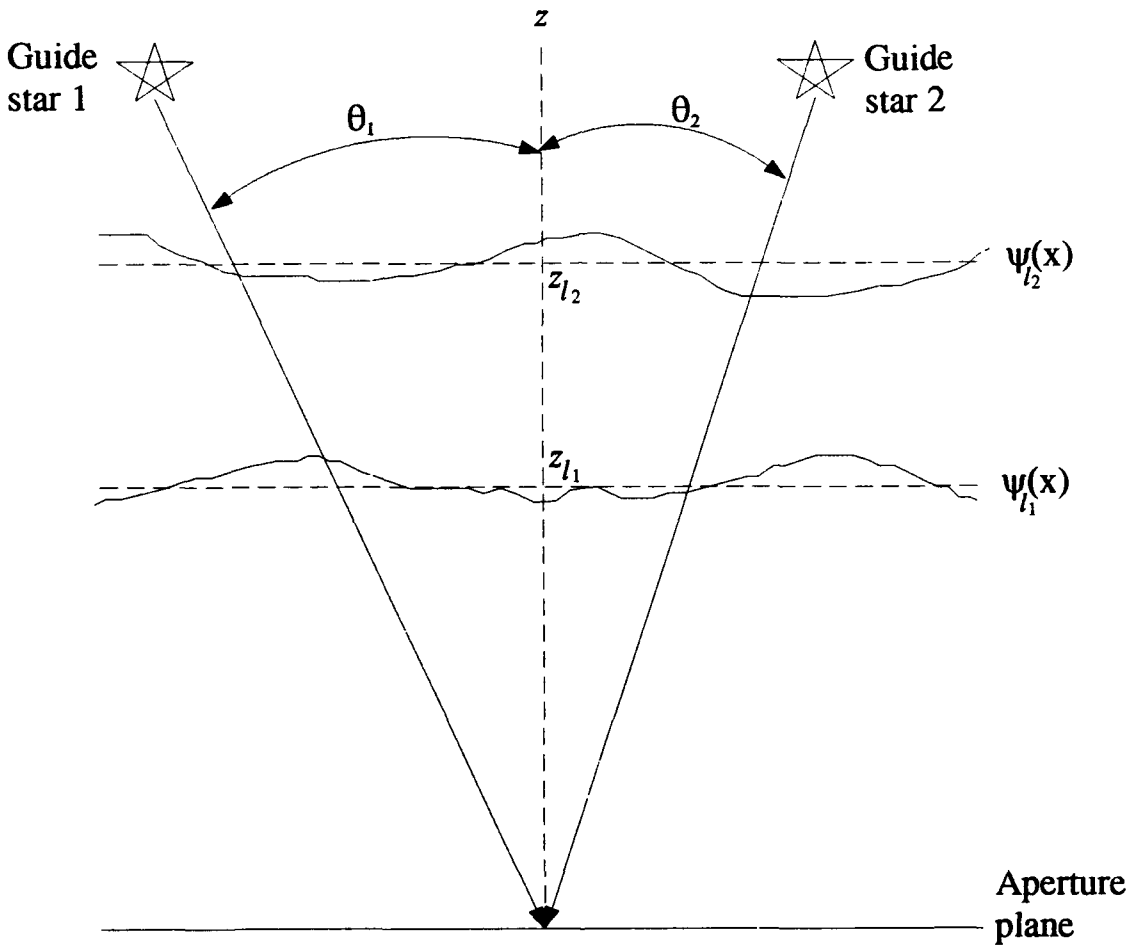

Figure 3.1. Atmosphere modeled by 2 phase screens and probed with 2 guide stars.

frequency domain:

$$\tilde{\psi}_{t_1}(\vec{f}) = \exp(j2\pi z_{l_1}\vec{f}\cdot\vec{\theta}_1)\tilde{\psi}_{l_1}(\vec{f}) + \exp(j2\pi z_{l_2}\vec{f}\cdot\vec{\theta}_1)\tilde{\psi}_{l_2}(\vec{f}) \tag{3.3}$$

$$\tilde{\psi}_{t_2}(\vec{f}) = \exp(j2\pi z_{l_1}\vec{f}\cdot\vec{\theta}_2)\tilde{\psi}_{l_1}(\vec{f}) + \exp(j2\pi z_{l_2}\vec{f}\cdot\vec{\theta}_2)\tilde{\psi}_{l_2}(\vec{f}) \tag{3.4}$$

where the tilde indicates the Fourier transform. By inverting the preceding system, the transform of the turbulent layer contributions may be obtained in terms of the transforms of the measurements. For turbulent layer 1 the result is

$$\tilde{\psi}_{l_1}(\vec{f}) = \tilde{h}_{w_{11}}(\vec{f})\psi_{t_1}(\vec{f}) + \tilde{h}_{w_{12}}(\vec{f})\psi_{t_2}(\vec{f}) \tag{3.5}$$

where

$$\tilde{h}_{w_{11}}(\vec{f}) = \frac{\exp(j2\pi z_{l_2}\vec{f}\cdot\vec{\theta}_2)}{\exp[j2\pi\vec{f}\cdot(z_{l_1}\vec{\theta}_1 + z_{l_2}\vec{\theta}_2)] - \exp[j2\pi\vec{f}\cdot(z_{l_1}\vec{\theta}_2 + z_{l_2}\vec{\theta}_1)]} \tag{3.6}$$

$$\tilde{h}_{w_{12}}(\vec{f}) = \frac{-\exp(j2\pi z_{l_2}\vec{f}\cdot\vec{\theta}_1)}{\exp[j2\pi\vec{f}\cdot(z_{l_1}\vec{\theta}_1 + z_{l_2}\vec{\theta}_2)] - \exp[j2\pi\vec{f}\cdot(z_{l_1}\vec{\theta}_2 + z_{l_2}\vec{\theta}_1)]} \tag{3.7}$$

The magnitude of these complex weights is

$$|\tilde{h}_{w_{11}}| = |\tilde{h}_{w_{12}}| = \left|\frac{1}{2\sin\left\{\pi\left[(z_{l_2} - z_{i_1})\vec{f}\cdot(\vec{\theta}_2 - \vec{\theta}_1)\right]\right\}}\right| \tag{3.8}$$

From the preceding equation, it is seen that these weighting functions, $\tilde{h}_{w_{i,m}}(\vec{f})$, have a singularity at the origin. As a result, the low frequency components of any noise in the measurements will be amplified and the estimates of the turbulent layer contributions will be poor. To deal with noisy measurements, a minimum mean square error filtering approach is taken in this chapter. Assumed *a priori* knowledge statistics of the phase and noise random processes are used to obtain optimum weights.

Several simplifying assumptions are necessary in order to analyze this problem in the frequency domain. As in the preceding example, it is assumed throughout this chapter that measurements of the total phase are available, which is not usually true in practice. Also, the finite size of the telescope aperture is not taken into account. Adaptive optical components such as the WFS and tilt removal system are modeled approximately as linear spatial filters. Finally, phase statistics are described with a Gaussian correlation function instead of the Kolmogorov structure function. Because of these assumptions, and because the analysis is mathematically cumbersome, the results of this frequency domain analysis are more suitable for qualitative understanding of the estimation problem rather than for quantitative performance predictions. All of the simplifying assumptions listed in this paragraph are dropped in the spatial domain analysis of Chapter IV.

In Section 3.2, the atmospheric model used in this chapter is presented while Section 3.3 outlines the geometry of the problem. Section 3.4 defines linear models for wavefront propagation, piston and overall tilt removal, wavefront measurement, and wavefront component estimation. The analysis is performed in Sections 3.5 and 3.6, while the performance of the estimator is evaluated for several choices of parameters in Section 3.7. Finally, an example problem is worked in Section 3.8 and a summary is in Section 3.9.

3.2 Atmospheric Model

Experimental evidence indicates that optical turbulence in the atmosphere is often concentrated in a small number of layers (52, 61). In a recent paper, McKechnie presented a theoretical framework for a layered atmospheric model, in which he collapsed the effects of each layer into a phase screen (45). Based on these experimental and theoretical results, the validity of an atmospheric model consisting of I statistically independent phase screens is assumed. As indicated in Chapter I, it is assumed that geometrical optics may be used to describe the propagation of light through down through the atmosphere at the observatory site.

As described in the previous section, a phase perturbation function $\psi_{l_s}(\vec{x})$ is associated with each phase screen in this atmospheric model. This function is assumed to be a sample function of a zero-mean, spatially stationary random process, described by a phase variance, $\sigma^2_{\psi_{l_s}}$ (rad^2), and spatial correlation function

$$\Gamma_{\psi_{l_s}}(r) = \langle \psi_{l_s}(\vec{x})\psi_{l_s}(\vec{x}+\vec{r})\rangle \tag{3.9}$$

where $r = |\vec{r}|$ (m) is the distance between two points in the plane and angle brackets indicate ensemble averaging. Following Barakat and Beletic (3), it is assumed that the spatial statistics of the phase screens may be described by Gaussian correlation functions:

$$\Gamma_{\psi_{l_s}}(r) = \sigma^2_{\psi_{l_s}} \exp\left(-\frac{r^2}{\rho^2_{l_s}}\right) \qquad (\text{rad}^2) \tag{3.10}$$

The parameter ρ_{l_s} (m) is the wavefront correlation length associated with each phase screen. Also of interest is the power spectral density (PSD) of the phase screen,

$$\Phi_{\psi_{l_s}}(f) = \pi\sigma^2_{\psi_{l_s}}\rho^2_{l_s}\exp(-\pi^2\rho^2_{l_s}f^2) \qquad ((\text{rad-m})^2) \tag{3.11}$$

which is the Fourier transform of the autocorrelation function with f (m^{-1}) being the spatial frequency variable.

Some researchers may question the validity of the Gaussian autocorrelation function (3.10) in describing atmospheric statistics. Normally the Kolmogorov structure function, equation (2.43) is used, because it is well supported by experimental data. However, for proper choice of the parameters $\sigma^2_{\psi_{l_s}}$ and ρ_{l_s}, the structure function which corresponds to the Gaussian correlation function of equation (3.10),

$$\mathcal{D}_G(r) = 2\sigma^2_{\psi_{l_s}}\left[1 - \exp\left(-\frac{r^2}{\rho^2_{l_s}}\right)\right] \tag{3.12}$$

is similar in shape except it approaches a finite variance, in contrast to the infinite variance associated with Kolmogorov statistics. In this sense, the Gaussian autocorrelation function is more physically intuitive. By equating expressions (2.43) and (3.12) at the point $r = \rho_{l_s}$, the following formula relates r_0 and ρ_{l_s}:

$$r_0 = 2.76 \frac{\rho_{l_s}}{\sigma_{\psi_{l_s}}^{6/5}} \tag{3.13}$$

Figure 3.2 is a representative plot of the two structure functions related by equation (3.13), out to an approximate outer scale of 1 meter. Strictly speaking, the Kolmogorov structure function is not valid for points separated by a distance greater than the outer scale. It may be argued that the Gaussian structure function is as good a model as any for larger scale sizes, given the present state of knowledge. It should be noted that the *correlation* length, ρ_{l_s}, and the atmospheric *coherence* diameter, r_0, describe different wavefront characteristics (60).

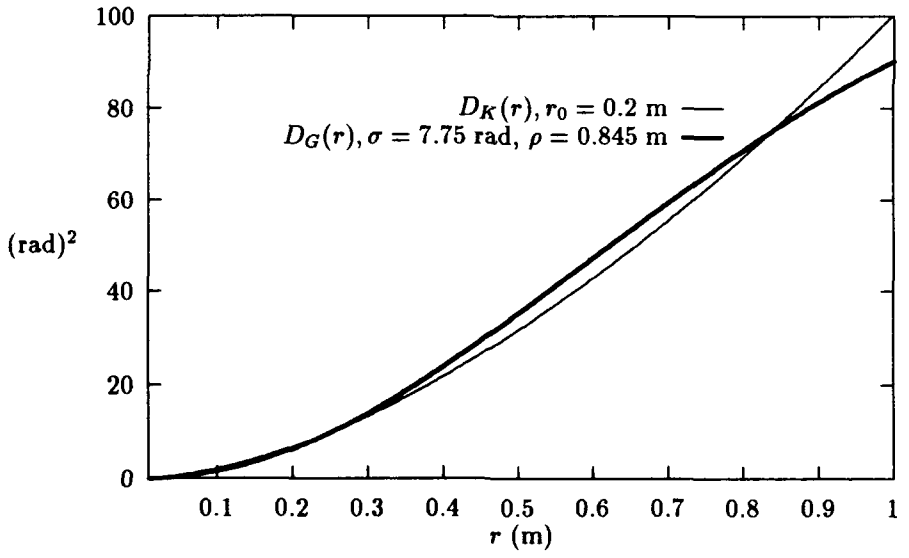

Figure 3.2. Comparison of Kolmogorov and Gaussian structure functions

It is useful to relate the strength of each turbulent layer to r_0, the most common measure of overall seeing conditions. In Chapter II it was shown that for zenith viewing at a particular

wavelength,

$$r_0^{-5/3} = \gamma \int_0^z d\xi \, C_n^2(\xi) \tag{3.14}$$

where γ is a constant and z is the upper bound of the turbulence region. If the turbulence region is divided into K contiguous slabs,the preceding equation may be rewritten as follows:

$$\begin{aligned} r_0^{-5/3} &= \sum_{k=1}^{K} \gamma \int_{z_{k-1}}^{z_k} d\xi \, C_n^2(\xi) \\ &= \sum_{k=1}^{K} r_k^{-5/3} \end{aligned} \tag{3.15}$$

where slab k lies between the altitudes z_{k-1} and z_k. The definition

$$r_k = \left[\gamma \int_{z_{k-1}}^{z_k} d\xi \, C_n^2(\xi) \right]^{-3/5} \tag{3.16}$$

is due to Beckers (5). In addition, McKechnie showed that the total wavefront correlation function is equal to the sum of the individual correlation functions (45). Using this result and equation (3.15), the statistical averages of of the overall atmosphere can be related to those of the component layers.

3.3 Geometry

Figure 3.3(a) shows two of M reference sources located well above the optical turbulence region of the atmosphere, of which two of I turbulent layers are depicted. It is assumed that the altitude of the reference sources is high enough that the waves emanating from them can be considered planar. The reference stars are somehow multiplexed so that all M phase perturbation measurements are made within the atmosphere's correlation time (27), using a single WFS. The problem is, based on such measurements, to determine the phase perturbation function, $\psi_{l_i}(\vec{x})$, associated with each layer. The coordinate system used for this analysis is shown in Figure 3.3(b). The position of each reference star is described by a two-dimensional vector $\vec{\theta}_m = (\theta_{m_x}, \theta_{m_y})$. The

components of this vector are angular offsets from the telescope (z) axis in the x and y directions and are related to the zenith angle θ by

$$\theta = \tan^{-1}\left(\tan^2\theta_x + \tan^2\theta_y\right)^{1/2} \tag{3.17}$$

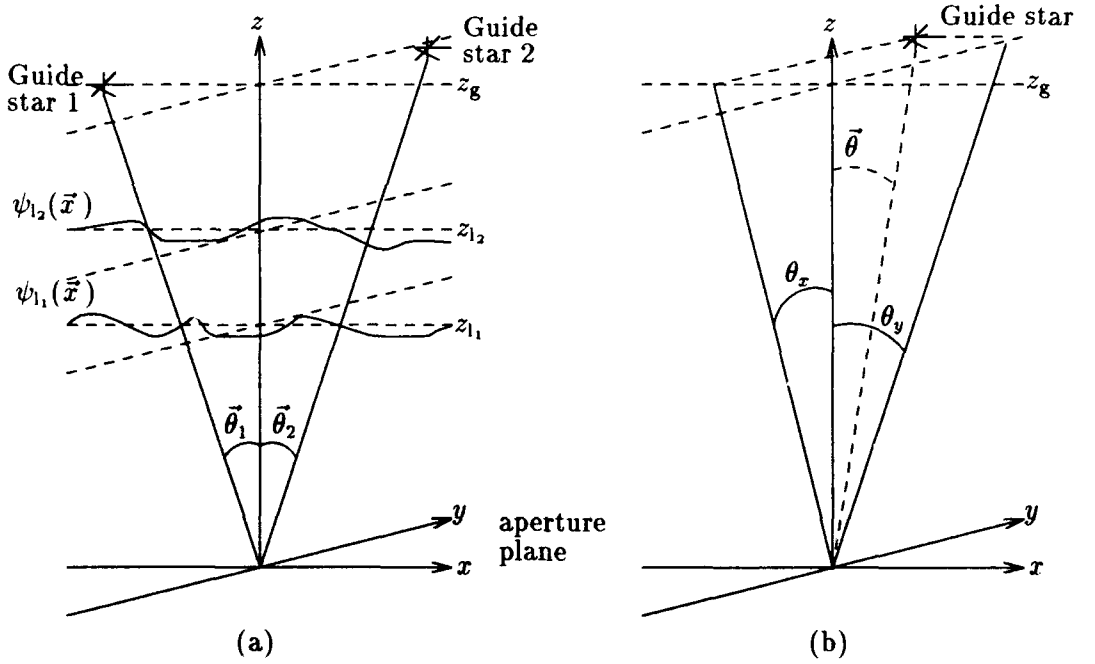

Figure 3.3. Location and geometry of reference sources.

Recall that in this chapter the implications of a finite telescope aperture are not being addressed. As discussed in Chapter IV, an important consideration is that the guide stars must be close enough together to project a large common portion of each turbulent layer onto the aperture.

3.4 Signal Processing

In the following sections, a linear model for wavefront propagation, overall tilt removal, wavefront measurement, and wavefront component estimation is presented. The model assumes that the wavefront sensor output is a continuous representation of the wavefront rather than a discrete array of slope measurements. This approach avoids the numerical complexities of large matrix cal-

culations ((13, 63) and Chapter IV) and allows intuitive understanding of the wavefront component estimation problem. The various functions performed by the adaptive optics system are modeled as spatial filtering operations (59), allowing insight to be gained into the effect of different system parameters on the accuracy of the estimates. The analysis of Chapter IV follows a more rigorous formalism along the lines of reference (63).

3.4.1 Wavefront Propagation. Using a small angle approximation and referring to Figure 3.3, it can be seen that the plane wave from reference source m projects $\psi_{l_i}(\vec{x})$ onto the aperture plane, shifted by an amount dependent on the layer altitude and guide star position. Assuming the validity of the geometrical optics approach, the total perturbation, $\psi_{t_m}(\vec{x})$, of a plane wave from reference source m propagating through I layers is

$$\psi_{t_m}(\vec{x}) = \sum_{i=1}^{I} \psi_{l_i}(\vec{x} + z_{l_i}\vec{\theta}_m) \tag{3.18}$$

3.4.2 Piston and Overall Tilt Removal. The average value of the phase aberration function over the area of the telescope aperture is known as the piston mode of the wavefront. The piston mode is not considered an aberration and does not need to be estimated and compensated by an adaptive optics system. To obtain accurate results in adaptive optics calculations, the piston mode must be removed from all wavefront models. Otherwise, adaptive optics system performance predictions may be too pessimistic because piston estimation and correction errors are included. In addition to the piston mode, the wavefront intercepted by the telescope aperture will almost always have a significant nonzero aperture-averaged gradient. Usually, an adaptive optics system removes this overall tilt with a separate feedback mechanism from the DM. One reason for this approach is that most deformable mirrors lack the dynamic range to remove substantial overall tilt components. In keeping with the linear systems approach, overall piston and tilt removal is approximated by attenuation of the lowest spatial frequencies in the wavefront. Tyson finds that in

such a spatial filtering method, tilt is seen as having a spatial frequency content of "about 1/2 cycle per mirror diameter (59)." Since the amount of piston and overall tilt depends on the aperture size, the piston and tilt removal operation is modeled as a convolution of the total wavefront with an impulse response function $h_a(\vec{x})$ which depends on the effective telescope aperture. Letting the notation $\varphi(\vec{x})$ represent a tilt-removed wavefront,

$$\begin{aligned} \varphi_{t_m}(\vec{x}) &= \psi_{t_m}(\vec{x}) * h_a(\vec{x}) \\ &= \sum_{i=1}^{I} \psi_{l_i}(\vec{x} + z_{l_i}\vec{\theta}_m) * h_a(\vec{x}) \\ &= \sum_{i=1}^{I} \varphi_{l_i}(\vec{x} + z_{l_i}\vec{\theta}_m) \end{aligned} \tag{3.19}$$

where $*$ indicates two-dimensional convolution and $\varphi_{l_i}(\vec{x}) = \psi_{l_i}(\vec{x}) * h_a(\vec{x})$ is the piston- and tilt-removed phase of the ith layer. The function $\varphi_{t_m}(\vec{x})$ represents the wavefront to be measured. The remainder of the analysis deals only with piston- and tilt-removed wavefronts.

3.4.3 Wavefront Measurement. Typically, wavefront sensors used in practical adaptive optics systems measure the gradient of the total wavefront instead of the actual phase. The estimate of the wavefront is then reconstructed on the surface of the DM via a summation of the influence functions which describe the spatial response of each mirror actuator. In this chapter, these two processes are combined and the adaptive optics system is modeled as measuring the wavefront phase directly. This wavefront "measurement" will have two chief sources of error: sampling error and measurement noise. Both of these error sources are related to the size of the WFS subapertures in an adaptive optics system.

3.4.3.1 Sampling Error. Actual wavefront sensors usually divide the telescope aperture into an array of subapertures, and the wavefront slope is measured over each subaperture. Because of the finite size of the subaperture, the WFS cannot measure the phase gradient at a

single point. Instead, the WFS determines the average gradient over the subaperture. Similarly, the DM cannot reconstruct the highest spatial frequencies in the wavefront due to the spatial separation of the actuator positions, which is approximately equal to the size of the WFS subapertures. These inaccuracies are modeled as a sampling error in the wavefront measurement process. In this analysis these spatial limitations are described with an impulse response function, $h_{\mathrm{sa}}(\vec{x})$, related to the subaperture size, so that the output of the wavefront measurement/reconstruction system can be written

$$\bar{\varphi}_{\mathrm{t_m}}(\vec{x}) = \varphi_{\mathrm{t_m}}(\vec{x}) * h_{\mathrm{sa}}(\vec{x}) \tag{3.20}$$

Because of the fact that actual wavefront sensors measure the average wavefront gradient over the subaperture, the form of $h_{\mathrm{sa}}(\vec{x})$ is chosen to implement subaperture wavefront averaging. Hence, $\bar{\varphi}_{\mathrm{t_m}}(\vec{x})$ represents the measured wavefront, with the overbar indicating the average phase over the subaperture. In this model, the subapertures are not fixed to a grid of points, rather, a continuous output is assumed. As indicated previously, this approximation simplifies the analysis by allowing the analysis to be conducted in terms of continuous functions.

3.4.3.2 Measurement Noise. Due primarily to photon noise, the WFS measurements will be somewhat in error. This effect is modeled with a continuous, zero mean random process, $n(\vec{x})$ (rad), which is independent of the random processes $\psi_{\mathrm{l}_i}(\vec{x})$. In an actual wavefront sensor, the measurement noise is uncorrelated from subaperture to subaperture (62). For this reason, the noise is not expected to contribute significantly to the lowest spatial frequencies in the wavefront aberration function. Hence, the noise is modeled as white, except for attenuation of the lowest spatial frequencies according to the size of the telescope aperture:

$$\eta(\vec{x}) = n(\vec{x}) * h_{\mathrm{a}}(\vec{x}) \tag{3.21}$$

where $\eta(\vec{x})$ (rad) is the "tilt-removed" noise.

To complete the model of the wavefront sensor, the second order statistics of the noise need to be further specified by selecting an appropriate value, $\mathcal{N}$, for the constant noise power spectral density. If the mean square error in the WFS measurements is σ_η^2 (rad^2), then the corresponding noise power density level is

$$\mathcal{N} = \frac{\sigma_\eta^2}{\int d\vec{f}\,|\tilde{h}_{\mathrm{a}}(\vec{f})|^2 |\tilde{h}_{\mathrm{sa}}(\vec{f})|^2} \tag{3.22}$$

where $\tilde{h}$ indicates the Fourier transform of h and $\vec{f} = (f_x, f_y)$ (m^{-1}) is a spatial frequency vector. The tilt-removed noise PSD is then

$$\Phi_\eta(\vec{f}) = \mathcal{N}|\tilde{h}_{\mathrm{a}}(\vec{f})|^2 \qquad ((\text{rad-m})^2) \tag{3.23}$$

The final output of the measurement system, $\bar{\varphi}'_{\mathrm{t}_m}(\vec{x})$, is the average noise-contaminated wavefront over a subaperture:

$$\bar{\varphi}'_{\mathrm{t}_m}(\vec{x}) = [\varphi_{\mathrm{t}_m}(\vec{x}) + \eta_m(\vec{x})] * h_{\mathrm{sa}}(\vec{x}) \tag{3.24}$$

where $\eta_m(\vec{x})$ is the noise in the mth wavefront measurement.

3.4.4 Component Estimation. Beckers suggested collecting an ensemble of wavefront measurements given by equation (3.24), spatially shifting them so that the component from a particular turbulent layer will be properly aligned in each measurement, and then averaging the ensemble. He expected that the result of such an averaging process will be strongly weighted toward the contribution from the turbulent layer of interest, with contributions from other layers tending to average out. This idea is generalized to a goal of finding the optimum combination of amplitude weighting and shifting which needs to be applied to each measurement in the linear combination. Since amplitude weighting and spatial shifting are linear shift-invariant operations, the estimate of

$\varphi_{l_i}(\vec{x})$ takes the following form:

$$\begin{aligned}\hat{\varphi}_{l_i}(\vec{x}) &= \sum_{m=1}^{M} \bar{\varphi}'_{l_m}(\vec{x}) * h_{w_i m}(\vec{x}) \\ &= \sum_{m=1}^{M} \left[\sum_{i'=1}^{N} \varphi_{l_{i'}}(\vec{x} + z_{l_{i'}} \vec{\theta}_m) + \eta_m(\vec{x}) \right] * h_{sa}(\vec{x}) * h_{w_i m}(\vec{x}) \end{aligned} \tag{3.25}$$

where $h_{w_i m}(\vec{x})$ represents the amplitude weighting and shifting applied to wavefront sensor measurement m in the estimate of wavefront component $\psi_{l_i}(\vec{x})$. The task at hand is to find the optimum set of functions $h_{w_i m}(\vec{x})$.

3.5 Mean Square Error Calculation

The goal is to minimize the mean square error in the estimate. Using angle brackets to signify expectation, the mean square difference between the estimated and actual wavefront phase from the ith turbulent layer is defined as:

$$\begin{aligned}\epsilon^2(\vec{x}) &= \left\langle [\varphi_{l_i}(\vec{x}) - \hat{\varphi}_{l_i}(\vec{x})]^2 \right\rangle \\ &= \left\langle \varphi_{l_i}^2(\vec{x}) \right\rangle + \left\langle \hat{\varphi}_{l_i}^2(\vec{x}) \right\rangle - 2 \left\langle \hat{\varphi}_{l_i}(\vec{x}) \varphi_{l_i}(\vec{x}) \right\rangle \\ &= \Gamma_{\varphi_{l_i}}(0) + \Gamma_{\hat{\varphi}_{l_i}}(0) - 2\Gamma_{\hat{\varphi}_{l_i}\varphi_{l_i}}(0) \\ &= \sigma^2_{\varphi_{l_i}} + \int d\vec{f}\, \Phi_{\hat{\varphi}_{l_i}}(\vec{f}) - 2 \int d\vec{f}\, \Phi_{\hat{\varphi}_{l_i}\varphi_{l_i}}(\vec{f}) \end{aligned} \tag{3.26}$$

The double subscripts indicate cross correlation functions or cross power spectra, as appropriate. If it assumed that the second order statistics (i.e. $\Gamma_{\psi_{l_i}}$) of each phase screen are known *a priori*, then the quantities in equation (3.26) can be calculated (i.e. $\Gamma_{\varphi_{l_i}}$, $\sigma^2_{\varphi_{l_i}}$, $\Gamma_{\hat{\varphi}_{l_i}}$, $\Phi_{\hat{\varphi}_{l_i}}$, $\Gamma_{\hat{\varphi}_{l_i}\varphi_{l_i}}$, and

$\Phi_{\hat{\varphi}_{l_i}\varphi_{l_i}}$). Using equation (3.25), the autocorrelation function of $\hat{\varphi}_{l_i}(\vec{x})$ is found:

$$\begin{aligned}\Gamma_{\hat{\varphi}_{l_i}}(\vec{x}) &= \langle \hat{\varphi}_{l_i}(\vec{x}' + \vec{x})\hat{\varphi}_{l_i}(\vec{x}')\rangle \\ &= \sum_{m=1}^{M}\left\{\sum_{m'=1}^{M}\sum_{i'=1}^{I}\Gamma_{\varphi_{l_{i'}}}\left[\vec{x} + z_{l_{i'}}(\vec{\theta}_m - \vec{\theta}_{m'})\right] * h_{\mathrm{w}_{i,m}}(\vec{x}) * h_{\mathrm{w}_{i,m'}}(-\vec{x}) + \right. \\ &\quad \left. \Gamma_{\eta}(\vec{x}) * h_{\mathrm{w}_{i,m}}(\vec{x}) * h_{\mathrm{w}_{i,m}}(-\vec{x})\right\} * h_{\mathrm{sa}}(\vec{x}) * h_{\mathrm{sa}}(-\vec{x}) \end{aligned} \tag{3.27}$$

In arriving at equation (3.27), the mutual independence of the random process $\psi_{l_i}(\vec{x})$ and $n_m(\vec{x})$ was used. The derivation of this expression is found in Appendix A.

The Fourier transform of equation (3.27) is the power spectral density of $\hat{\varphi}_{l_i}(\vec{x})$:

$$\begin{aligned}&\Phi_{\hat{\varphi}_{l_i}}(\vec{f}) = \\ &\quad |\tilde{h}_{\mathrm{sa}}(\vec{f})|^2 \sum_{m=1}^{M}\left[\sum_{m'=1}^{M}\sum_{i'=1}^{I}\Phi_{\varphi_{l_{i'}}}(\vec{f})\tilde{h}_{i'm}(\vec{f})\tilde{h}^*_{i'm'}(\vec{f})\tilde{h}_{\mathrm{w}_{i,m}}(\vec{f})\tilde{h}^*_{\mathrm{w}_{i,m'}}(\vec{f}) + \Phi_{\eta}(\vec{f})|\tilde{h}_{\mathrm{w}_{i,m}}(\vec{f})|^2\right]\end{aligned} \tag{3.28}$$

In the above equation, $\tilde{h}_{im} = \exp[j2\pi z_{l_i}(\vec{\theta}_m \cdot \vec{f})]$, and h^* is the complex conjugate of h. Having derived equation (3.28), it is less difficult to obtain the cross power spectrum $\Phi_{\hat{\varphi}_{l_i}\varphi_{l_i}}(\vec{f})$:

$$\Phi_{\hat{\varphi}_{l_i}\varphi_{l_i}}(\vec{f}) = \Phi_{\varphi_{l_i}}(\vec{f})\tilde{h}_{\mathrm{sa}}(\vec{f})\sum_{m=1}^{M}\tilde{h}_{im}(\vec{f})\tilde{h}_{\mathrm{w}_{i,m}}(\vec{f}) \tag{3.29}$$

The power spectra in (3.28) and (3.29) may be substituted in equation (3.26) to obtain a general expression for the mean squared error in estimating the wavefront contribution of one of I turbulent layers using measurements made from M different reference sources.

3.6 Derivation of Optimum Weights

For illustration purposes, the case of two turbulent layers and two reference sources is considered. The calculations can be generalized for $M \geq I \geq 2$, but, as the previous section indicates,

lengthy expressions are involved. Letting $M = I = 2$, the general results of the preceding section are used to obtain the mean-square error in the estimation for this case:

$$\begin{aligned}\epsilon^2 &= \sigma^2_{\varphi_{l_1}} + \int\int df_x\, df_y \left[|\tilde{h}_{\rm sa}|^2 \left(|\tilde{h}_{{\rm w}_{11}}|^2 + |\tilde{h}_{{\rm w}_{12}}|^2 + 2{\rm Re}\left\{ \tilde{h}_{{\rm w}_{11}} \tilde{h}^*_{{\rm w}_{12}} \tilde{h}_{11} \tilde{h}^*_{12} \right\} \right) - \right. \\ &\quad \left. 2\tilde{h}_{\rm sa} \left(\tilde{h}_{{\rm w}_{11}} \tilde{h}_{11} + \tilde{h}_{{\rm w}_{12}} \tilde{h}_{12} \right) \right] \Phi_{\varphi_{l_1}} + \\ &\quad \int\int df_x\, df_y \left[|\tilde{h}_{\rm sa}|^2 \left(|\tilde{h}_{{\rm w}_{11}}|^2 + |\tilde{h}_{{\rm w}_{12}}|^2 + 2{\rm Re}\left\{ \tilde{h}_{{\rm w}_{11}} \tilde{h}^*_{{\rm w}_{12}} \tilde{h}_{21} \tilde{h}^*_{22} \right\} \right) \right] \Phi_{\varphi_{l_2}} + \\ &\quad \int\int df_x\, df_y \left[|\tilde{h}_{\rm sa}|^2 \left(|\tilde{h}_{{\rm w}_{11}}|^2 + |\tilde{h}_{{\rm w}_{12}}|^2 \right) \right] \Phi_\eta \end{aligned} \tag{3.30}$$

Here, the fact that $|\tilde{h}_{im}|^2 = 1$ was used, and the (f_x, f_y) dependence was suppressed to shorten the expression. The goal is to find $\tilde{h}_{{\rm w}_{11}}$ and $\tilde{h}_{{\rm w}_{12}}$ to minimize ϵ^2. To simplify the mathematics five assumptions are made:

$$\Phi_{\psi_{l_1}} = \Phi_{\psi_{l_2}} \tag{3.31}$$

$$\theta_1 = -\theta_2 \tag{3.32}$$

$$z_{l_2} = 2z_{l_1} \tag{3.33}$$

$$\tilde{h}_{\rm sa}(\vec{f}) = \begin{cases} 1 & f_x, f_y < f_{\rm sa} \\ 0 & \text{otherwise} \end{cases} \tag{3.34}$$

$$\tilde{h}_{\rm a}(\vec{f}) = \begin{cases} 0 & f_x, f_y < f_{\rm a} \\ 1 & \text{otherwise} \end{cases} \tag{3.35}$$

Assumption (3.31) is not realistic for typical atmospheric conditions. Usually, the turbulent layer nearest the ground is stronger than the one at higher altitude. However, using this assumption, the results should represent a median value for ϵ. That is, the results are expected to be better than if one were trying to estimate the wavefront due to the weaker of a pair of turbulent layers, but worse than if one were estimating that of the stronger of the two. Assumptions (3.32) and (3.33) allow the use of trigonometric identities to simplify the mathematics. Physically, these assumptions

specify that the guide stars are placed symmetrically about the optical axis and that the highest turbulent layer is located at twice the altitude of the lowest. A consequence of assumption (3.34) is that the impulse response of the WFS is

$$h_{\mathrm{sa}}(x,y) = 4f_{\mathrm{sa}}^2 \frac{\sin(2\pi f_{\mathrm{sa}} x)}{2\pi f_{\mathrm{sa}} x} \frac{\sin(2\pi f_{\mathrm{sa}} y)}{2\pi f_{\mathrm{sa}} y} \tag{3.36}$$

A measure of the width of $h_{\mathrm{sa}}(\vec{x})$ is

$$d = \frac{1}{2f_{\mathrm{sa}}} \tag{3.37}$$

The parameter d is equivalent to the subaperture spacing in a WFS. Assumption (3.35), models piston and tilt removal as the attenuation of the lowest spatial frequencies in the wavefront random process. The cutoff frequency f_{a} is related to the aperture diameter D in a manner similar to equation (3.37):

$$f_{\mathrm{a}} = \frac{1}{2D} \tag{3.38}$$

Using the assumptions given in (3.31) through (3.35), a somewhat simpler expression for the mean square error is obtained:

$$\begin{aligned} \epsilon^2 \;=\; & \sigma^2_{\varphi_{l_1}} + \int_{-f\mathrm{sa}}^{f\mathrm{sa}} \int_{-f\mathrm{sa}}^{f\mathrm{sa}} df_x\, df_y \left\{ 2\Phi_{\varphi_{l_1}} \left[|\tilde{h}_{\mathrm{w}_{11}}|^2 + |\tilde{h}_{\mathrm{w}_{12}}|^2 + \mathrm{Re}\left\{ \tilde{h}_{\mathrm{w}_{11}} \tilde{h}^*_{\mathrm{w}_{12}} (\tilde{h}^2_{11} + \tilde{h}^4_{11}) \right\} - \right.\right. \\ & \left.\left. \left(\tilde{h}_{\mathrm{w}_{11}} \tilde{h}_{11} + \tilde{h}_{\mathrm{w}_{12}} \tilde{h}^*_{11} \right) \right] + \left(|\tilde{h}_{\mathrm{w}_{11}}|^2 + |\tilde{h}_{\mathrm{w}_{12}}|^2 \right) \Phi_\eta \right\} \end{aligned} \tag{3.39}$$

Appendix A contains the details of this simplification. Having simplified the mean square error expression, the next step is to look for $\tilde{h}_{\mathrm{w}_{11}}$ and $\tilde{h}_{\mathrm{w}_{12}}$ to minimize ϵ^2.

From inspection of equation (3.39), it is seen that it is necessary that

$$\mathrm{Im}\{\tilde{h}_{\mathrm{w}_{11}} \tilde{h}_{11} + \tilde{h}_{\mathrm{w}_{12}} \tilde{h}^*_{11}\} = 0 \tag{3.40}$$

since the mean square error calculation must result in a real number. The above requirement leads to a coupling between the functions $\tilde{h}_{w_{11}}$ and $\tilde{h}_{w_{12}}$:

$$\mathrm{Re}\{\tilde{h}_{w_{11}}\} = \mathrm{Re}\{\tilde{h}_{w_{12}}\} - \frac{\mathrm{Re}\{\tilde{h}_{11}\}}{\mathrm{Im}\{\tilde{h}_{11}\}}\mathrm{Im}\{\tilde{h}_{w_{11}} + \tilde{h}_{w_{12}}\} \tag{3.41}$$

To obtain the optimum functions, equation (3.41) is substituted into (3.39), and the following system of equations is solved to get the real and imaginary parts of each weight:

$$\frac{\partial I}{\partial \mathrm{Im}\{\tilde{h}_{w_{11}}\}} = \frac{\partial I}{\partial \mathrm{Re}\{\tilde{h}_{w_{12}}\}} = \frac{\partial I}{\partial \mathrm{Im}\{\tilde{h}_{w_{12}}\}} = 0 \tag{3.42}$$

where I represents the term inside the large curly braces in equation (3.39). The real part of $\tilde{h}_{w_{11}}$ is then obtained from (3.41). A symbolic mathematics software package was extremely useful in performing the calculations and simplifying the results (44). With its aid, the real and imaginary parts of the optimum weights are found to be

$$\mathrm{Re}\{\tilde{h}_{w_{11}}\} = \mathrm{Re}\{\tilde{h}_{w_{12}}\} = \frac{\mathrm{Re}\{\tilde{h}_{11}\}\left[\Phi_{\varphi_{l_1}}\Phi_\eta + 4\mathrm{Im}^2\{\tilde{h}_{11}\}\Phi^2_{\varphi_{l_1}}\right]}{\Phi^2_\eta + 4\Phi_{\varphi_{l_1}}\Phi_\eta + 4\mathrm{Im}^2\{\tilde{h}_{11}\}\Phi^2_{\varphi_{l_1}}} \tag{3.43}$$

$$-\mathrm{Im}\{\tilde{h}_{w_{11}}\} = \mathrm{Im}\{\tilde{h}_{w_{12}}\} = \frac{\mathrm{Im}\{\tilde{h}_{11}\}\left[\Phi_{\varphi_{l_1}}\Phi_\eta + \left(2 - 4\mathrm{Re}^2\{\tilde{h}_{11}\}\right)\Phi^2_{\varphi_{l_1}}\right]}{\Phi^2_\eta + 4\Phi_{\varphi_{l_1}}\Phi_\eta + 4\mathrm{Im}^2\{\tilde{h}_{11}\}\Phi^2_{\varphi_{l_1}}} \tag{3.44}$$

Substitution of equations (3.43) and (3.44) into (3.39) and further use of computer algebra software leads to the final expression for the mean square error in estimating the wavefront due to one of two turbulent layers under assumptions (3.31) through (3.35):

$$\epsilon^2 = \sigma^2_{\varphi_{l_1}} - \int_{-f_{sa}}^{f_{sa}} df_x \int_{-f_{sa}}^{f_{sa}} df_y \frac{2\Phi^2_{\varphi_{l_1}}\Phi_\eta + 4\mathrm{Im}^2\left\{\tilde{h}_{11}\right\}\Phi^3_{\varphi_{l_1}}}{\Phi^2_\eta + 4\Phi_{\varphi_{l_1}}\Phi_\eta + 4\mathrm{Im}^2\left\{\tilde{h}_{11}\right\}\Phi^2_{\varphi_{l_1}}} \tag{3.45}$$

3.7 Performance Plots

The performance of the estimator may be evaluated by substituting different values of wavefront variance $\sigma^2_{\psi_{l_1}}$, measurement noise variance σ^2_η, wavefront correlation length ρ_{l_1}, wavefront sensor spatial bandwidth f_{sa}, tilt bandwidth f_a, turbulent layer altitude z_{l_1}, and guide star position θ_1 into equation (3.45). Results of the computations are plotted in Figures 3.4 through 3.8. Each figure is intended to illustrate the effect of varying a different parameter on the accuracy of the estimate, with the other parameters held constant. The curves are plotted against a "seeing-to-error" (SER) ratio:

$$\text{SER} = 20 \log \frac{\sigma_{\varphi_{l_1}}}{\sigma_\eta} \tag{3.46}$$

The SER is intended to show how much of the measured phase fluctuations are due to the seeing layer vs. the measurement error. The term "signal-to-noise" ratio is avoided since intensity levels are not being compared; however the SER plays a similar role in this estimation problem.

3.7.1 Tilt Removal. Tyson modeled an adaptive optics system as a two-dimensional spatial filter. As mentioned previously, he found that tilt may be viewed as having a spatial frequency content up to about 1/2 cycle per telescope diameter (59). With this guideline, a range of values for tilt bandwidth, f_a was selected and the results plotted in Figures 3.4 and 3.5. For the correlation length, the value $\rho_{l_1} = 0.845$ m was used. This value was employed in Section 3.2 to match the Gaussian structure function to the Kolmogorov structure function with $r_0 = 0.2$ m and outer scale of 1 m. As illustrated in Figure 3.4, eliminating the lowest spatial frequencies helps because the weighting functions $\tilde{h}_{w,m}$ have large magnitudes for low spatial frequencies, since most of the power in the phase fluctuations is concentrated in this region. Note that Figure 3.4 shows the rms error in the estimate normalized by the tilt-removed rms variation, $\sigma_{\varphi_{l_1}}$. As the lowest spatial frequencies are filtered out, the rms phase variation decreases. This normalization shows the improvement in the performance of the estimator alone, since it compares the rms error in the estimate to the rms phase deviation in the wavefront component that is actually in the measurement. Figure 3.5 shows

the same data normalized by the non-tilt-removed rms variation, $\sigma_{\psi_{l_1}}$. This second plot is included to illustrate the benefits of tilt removal to overall system performance. In this dissertation, the primary interest is in the performance of the wavefront component estimator, so the plots discussed in the next section are normalized by the tilt-removed rms variation, $\sigma_{\varphi_{l_1}}$.

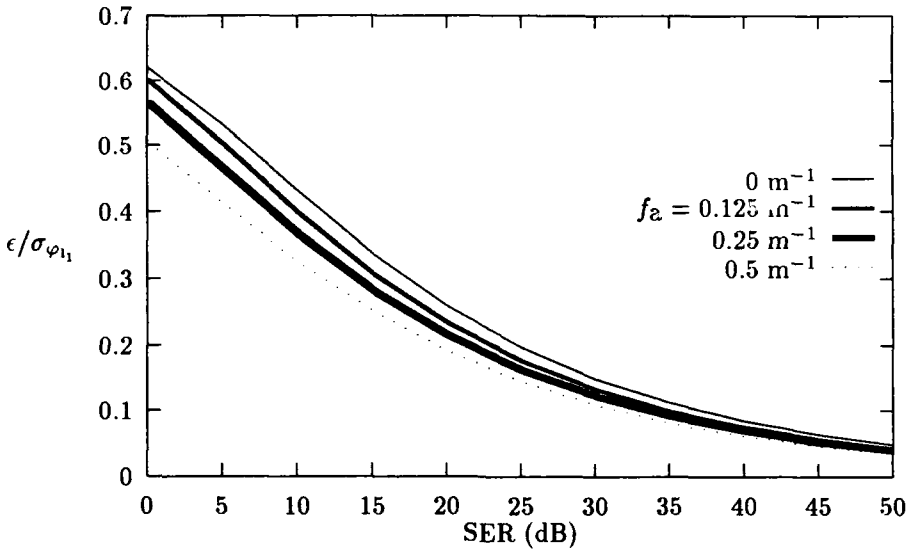

Figure 3.4. Estimator performance as function of tilt bandwidth ($\rho_{l_1} = 0.845$ m, $\vec{\theta}_1 = (10^{-5}, 0)$ rad, $f_{\mathrm{sa}} = 5$ m^{-1}, $z_{l_1} = 5000$ m). Results normalized by tilt-removed phase variance.

3.7.2 WFS Bandwidth. Figure 3.6 shows that the error performance improves as the spatial bandwidth of the wavefront sensor is increased. An increase in the WFS spatial bandwidth corresponds to a decrease in the size of the subaperture according to equation (3.37). As the wavefront is sampled with smaller apertures, the high frequency components in the random process are measured more accurately. The performance improvement is asymptotic because as the WFS bandwidth increases, eventually all of the significant power in the φ_{l_1} random process is contained within the passband.

3.7.3 Phase Correlation Length. Figure 3.7 shows how the performance of the estimator varies as the width of the wavefront autocorrelation function is varied. Performance improves as ρ_{l_1} increases since a wider autocorrelation function corresponds to a narrower power spectrum.

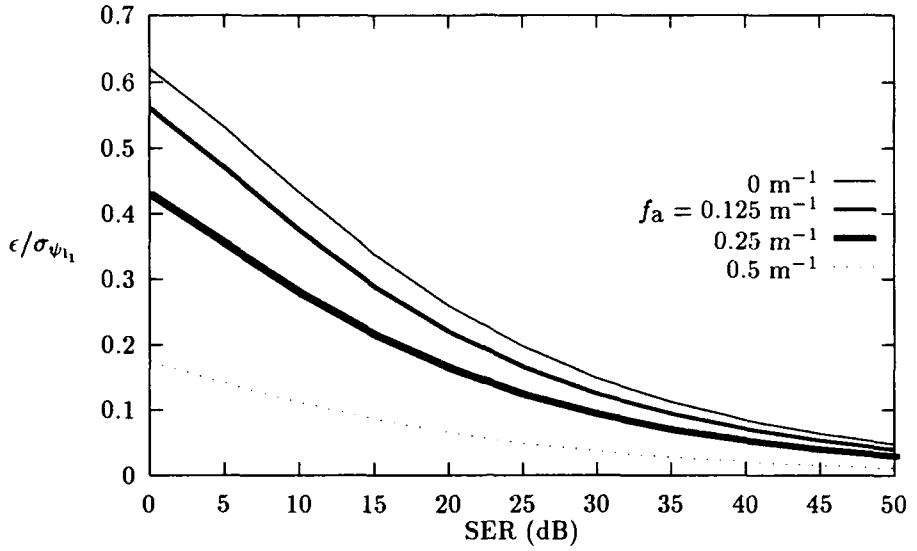

Figure 3.5. Estimator performance as function of tilt bandwidth ($\rho_{l_1} = 0.845$ m, $\vec{\theta}_1 = (10^{-5}, 0)$ rad, $f_{sa} = 5$ m^{-1}, $z_{l_1} = 5000$ m). Results normalized by non-tilt-removed phase variance.

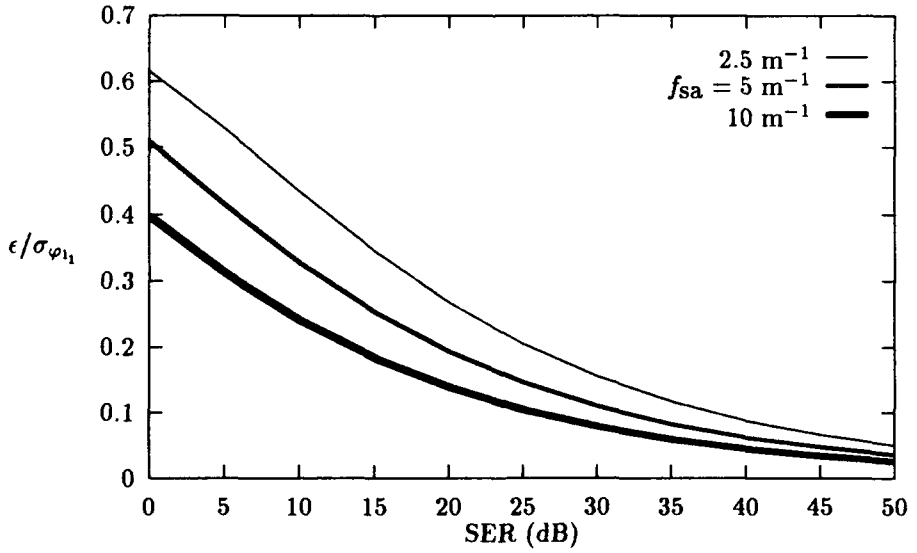

Figure 3.6. Estimator performance as function of WFS spatial bandwidth ($\rho_{l_1} = 0.845$ m, $\vec{\theta}_1 = (10^{-5}, 0)$ rad, $f_a = 0.5$ m^{-1}, $z_{l_1} = 5000$ m)

Hence, as ρ_{l_1} increases more of the significant power in the random process falls within the passband of the WFS transfer function $\tilde{h}_{sa}(\vec{f})$. This effect is asymptotic for the same reason as discussed in the previous paragraph.

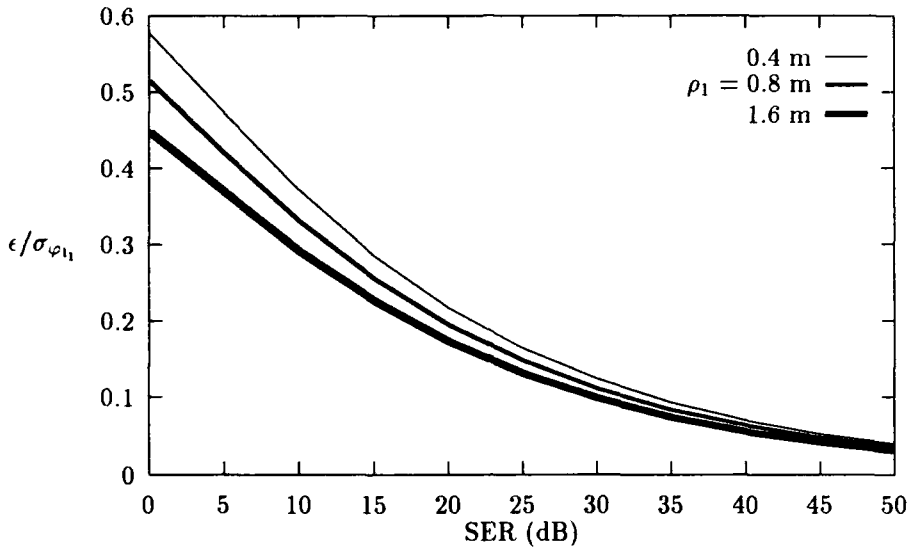

Figure 3.7. Estimator performance as function of wavefront correlation length ($\vec{\theta}_1 = (10^{-5}, 0)$ rad, $f_a = 0.5$ m^{-1}, $f_{sa} = 5$ m^{-1}, $z_{l_1} = 5000$ m)

3.7.4 Guide Star Separation. Figure 3.8 shows that estimator performance improves as the reference stars are spread more widely apart. Wider reference star separation means that the optimum weights must shift the measurements a greater distance in order to correlate the contribution from the turbulent layer of interest in each wavefront measurement. Such large spatial shifts also have the beneficial effect of decorrelating the contributions from the other layers more than small spatial shifts. This improvement is also asymptotic; after a point, the additional benefit of further decorrelation is negligible since after a point the shift of the competing layers is so large as to be on the skirts of the correlation functions. The finite size of the telescope aperture, not yet taken into account, would restrict guide star separation in a practical system.

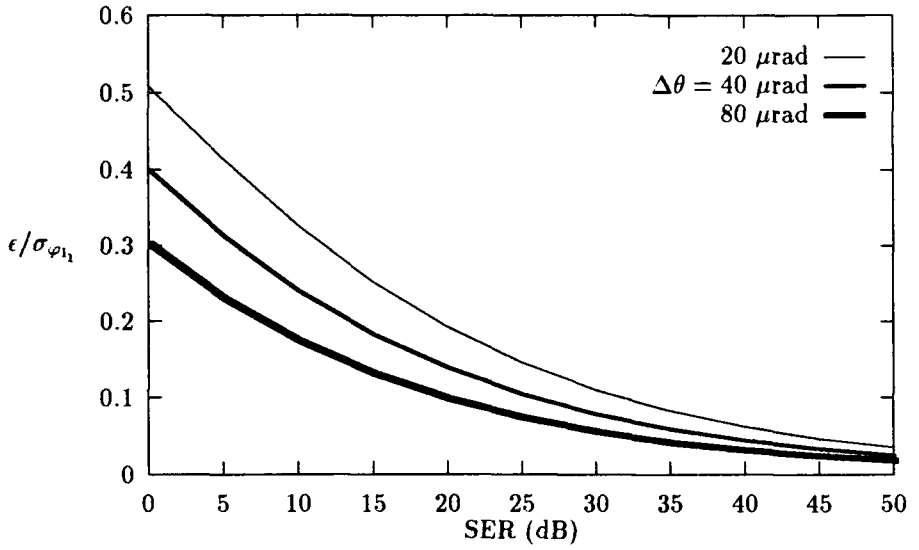

Figure 3.8. Estimator performance as function of reference star angular separation ($\rho_{l_1} = 0.845$ m, $f_a = 0.5$ m^{-1}, $f_{sa} = 5$ m^{-1}, $z_{l_1} = 5000$ m)

3.8 Example

The results of the previous section are now applied to the analysis of the performance of a multiconjugate adaptive optics system. For this example, it is assumed that the seeing conditions are characterized by Kolmogorov turbulence with $r_0 = 20$ cm. The Kolmogorov structure function is approximated with a Gaussian structure function, as shown in Figure 3.2, and it is found that $\sigma = 7.75$ rad and $\rho = 0.845$ m are good choices of parameters.

It is assumed that the turbulence is characterized by two identical layers, one at altitude $z_{l_1} = 5000$ m and the other at $z_{l_2} = 10000$ m, so the final result of the last Section (3.45) can be used in the calculations for this example. Using formula (3.15), it is seen that $r_1 = r_2 \sim 30$ cm. Also, the variance of the phase divides equally between the two turbulent layers, hence $\sigma_{\psi_{l_1}} = \sigma_{\psi_{l_2}} = 5.5$ rad.

Consistent with assumption (3.32) the guide stars are positioned symmetrically, with $\theta_1 = -\theta_2 = (10^{-5}, 0)$ rad. For an effective aperture size of 1 m, and assuming tilt accounts for up to 1/2 cycle per effective telescope aperture, $f_a = 0.5$ m^{-1} is obtained. This leads to a value of $\sigma_{\varphi_{l_1}}$

of $\sim$ 1.9 rad, implying that $\sim$ 88% of the power in the ψ_{l_1} random process is contained in the tilt component, which is about right for Kolmogorov turbulence. For subapertures that are 10 cm square, equation (3.37) may be used to approximate f_{sa} as 5 m^{-1}. Using these parameters in (3.45) the plot shown in Figure 3.9 is obtained, which gives the error in estimating the contribution of one of the two turbulent layers to the total wavefront.

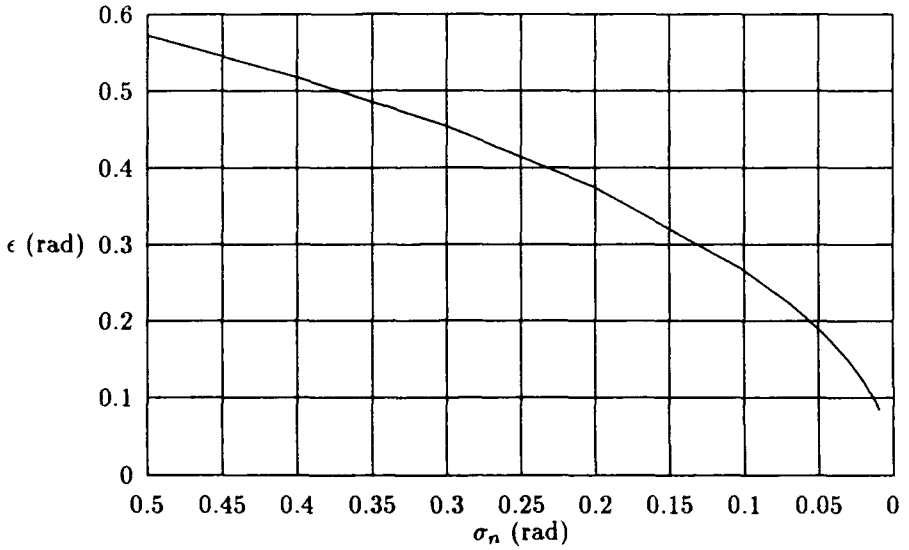

Figure 3.9. Estimator performance for $\sigma_{\varphi_{l_1}} = 5.5$ rad, $\rho_{l_1} = 0.845$ m, $\vec{\theta}_1 = (10^{-5}, 0)$ rad, $f_{sa} = 5$ m^{-1}, $f_a = 0.5$ m^{-1}, $z_{l_1} = 5000$ m

A typical goal for an adaptive optics system is to remove the rms wavefront phase distortion to $\leq$ 0.5 rad (19). The error in the estimated wavefront component will be one of several factors contributing to the inability of the adaptive optics system to perfectly remove phase distortion. Some of the possible factors for a two-DM MCAO system include: 1) wavefront estimation error for two wavefront components, 2) overall tilt removal error, and 3) error due to the change in the state of the atmosphere during processing time (time delay error). In order to achieve a system design goal of 0.5 rad rms residual phase error, the variance of each of the 4 aforementioned error sources must be a factor of 4 less than the goal. This consideration leads to a desired wavefront

component estimation error of $\sim$ 0.25 rad rms. From Figure 3.9, it is seen that this level of performance requires the wavefront measurement error to be $\leq$ 0.08 rad rms.

Wavefront sensor measurement noise power is inversely related to the number of photons entering the subaperture per integration time, $N_{\rm ph}$:

$$\sigma_{\rm n} = \frac{k_{\rm n}}{\sqrt{N_{\rm ph}}} \quad \text{(rad)} \tag{3.47}$$

where $k_{\rm n}$ is a constant which depends on wavefront sensor characteristics. In their recent analysis of a laser guide star adaptive optical telescope, Gardner *et al.* used $k_{\rm n} = 1.30$ (22). From the above formula and Figure 3.9, it is seen that 264 photons per subaperture per wavefront sensor integration time would be necessary to estimate $\varphi_{l_1}(\vec{x})$ to the required accuracy. This flux level is about 14 times that specified by Gardner *et al.* for a single-DM adaptive optics system to achieve a rms wavefront error of $\sim$ 0.57 rad when $r_0 = 20$ cm.

3.9 Summary

In this chapter, a frequency domain approach was taken to solve the problem of estimating the contribution of different parts of the atmosphere to total wavefront aberration. This approach provides some insight into the problem, but the approximations involved make the quantitative results somewhat questionable. The next chapter describes a spatial domain analysis which involves considerably fewer approximations.

IV. Spatial Domain Analysis

4.1 Introduction

In this chapter, a statistical approach is used determine the proper commands for each DM. The approach is based on Wallner's general adaptive optics system analysis method (62), which is extended to include systems with multiple guide stars and DMs. In Section 4.2, the atmosphere model used in this chapter is described, while Section 4.3 outlines the adaptive optics system model. The main analytical results are in Section 4.4, in which expressions for two types of mean square residual wavefront phase error are derived: 1) averaged over the surface of each DM and 2) averaged over the area of an object wavefront. The DM control commands are chosen to minimize the first type of error, while the second type of error is the criterion used to evaluate performance of the MCAO system. In Section 4.5, specific system and atmosphere characteristics are assumed in order to make numerical computations. In Section 4.6, the results of such computations are shown and a summary is in Section 4.7.

4.2 Atmospheric Model

As discussed in previous chapters, several factors motivate the consideration of a layered atmosphere model for an analysis of MCAO. One reason is that experimental evidence indicates that the optical turbulence in the atmosphere is often concentrated in a small number of layers (52, 61). However, any turbulence distribution could be approximated by using a sufficient number of layers. Since an MCAO system approximates a layered atmospheric structure, the use of such a model is convenient for analysis purposes.

To build a layered atmospheric model, it is first assumed that the refractive index structure constant, $C_n^2(z)$ ($\mathrm{m}^{-2/3}$), is known as a function of altitude, z. This information could come from a remote sensing instrument. This continuous profile is discretized into I thin turbulent layers at altitudes z_{l_i} (m). Each layer is modeled with a random phase screen, $\psi_{l_i}(\vec{x})$ (rad). The phase

screen $\psi_{l_i}(\vec{x})$ describes how the phase of an optical wave propagating through the horizontal plane $z = z_{l_i}$ is altered as a two-dimensional function of position $\vec{x}$ (m). This function is assumed to be a sample function of a random process characterized by a structure function $\mathcal{D}_i$ (rad^2):

$$\mathcal{D}_i(\vec{x}, \vec{x}') = \left\langle [\psi_{l_i}(\vec{x}) - \psi_{l_i}(\vec{x}')]^2 \right\rangle \tag{4.1}$$

where the angle brackets indicate an ensemble average. The turbulent layers are assumed to be statistically independent (26, 45).

As in Chapter III, geometrical optics propagation is assumed between the turbulent layers. This layered turbulence model is now used to write an expression for the total phase aberration on an optical wave emanating from a point source at an arbitrary position. Figure 4.1 shows a ray traced from the source through turbulent layer $\psi_{l_i}(\vec{x})$ to point $\vec{x}$ in the aperture plane. The location of the source is given by the position vector $\vec{r}_s = (z_s\theta_{s_x}, z_s\theta_{s_y}, z_s)$ (using a small angle approximation). The position vector $\vec{p}_i$ denotes the point where the ray crosses the plane of turbulent layer i. From the geometry, $\vec{p}_i$ is found to be

$$\vec{p}_i = \vec{x} + \left(\frac{z_{l_i}}{z_s}\right) \{[(\vec{r}_s - \vec{x}) \cdot \hat{x}]\,\hat{x} + [(\vec{r}_s - \vec{x}) \cdot \hat{y}]\,\hat{y}\} \tag{4.2}$$

where $\hat{x}$ and $\hat{y}$ are unit vectors in the x and y directions. This expression can be simplified to

$$\vec{p}_i = \vec{x}\left(1 - \frac{z_{l_i}}{z_s}\right) + z_{l_i}\vec{\theta}_s \tag{4.3}$$

Using this result, along with the geometrical optics assumption, the total wavefront in the aperture plane, $\psi_t(\vec{x})$, from a source located at position $\vec{\theta}_s$ (rad) and altitude z_s (m) is the sum of

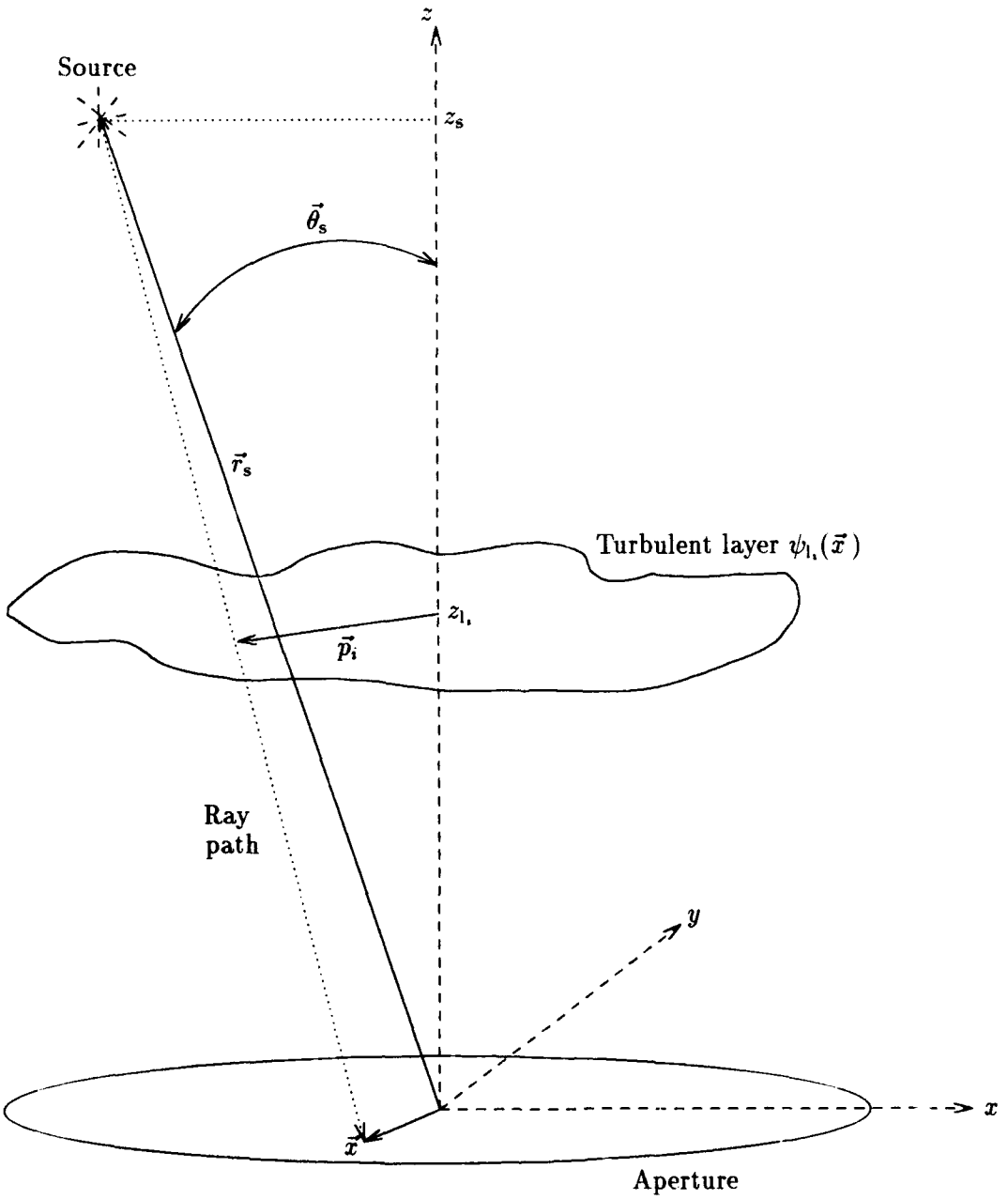

Figure 4.1. Geometry.

the I turbulent layer (phase screen) contributions.

$$\psi_t(\vec{x}) = \sum_{i=1}^{I} \psi_{l_i}\left[\vec{x}\left(1 - \frac{z_{l_i}}{z_s}\right) + z_{l_i}\vec{\theta}_s\right] \tag{4.4}$$

where $\psi_{l_i}(\vec{x})$ is the contribution of turbulent layer i. In this model, the spherical surface of the wavefront from a finite altitude source is ignored. In practice, it must be accurately determined (36).

4.3 System Model

The adaptive optics system model described in this section is based on the model presented by Wallner in (62). His model was also used by Welsh and Gardner to study the single-DM, open loop adaptive telescope schematically diagrammed in Figure 4.2. In this illustration, a reference wavefront propagates through a region of optical turbulence and arrives at the telescope aperture as an aberrated wavefront described by the phase perturbation function, $\psi_t(\vec{x})$ (rad). A WFS in a conjugate plane to the aperture measures the average wavefront gradient over an array of subapertures. The control matrix, $\mathbf{M}$, linearly combines the slope measurements, $\mathbf{s}$, to obtain a set of command voltages, $\mathbf{c}$, to be applied to the actuators on the DM. Typically, the DM is also conjugated to the aperture plane. The matrix $\mathbf{M}$ is chosen to minimize some functional of the residual wavefront error, $\epsilon(\vec{x})$ (rad).

In this chapter, this model is generalized so that adaptive telescopes with K DMs can be studied. As shown in Figure 4.3 ($K = 2$), the light reflects off each DM in series. In this approach, the DMs are conjugated to planes at a range of distances from the aperture. Appropriate command vectors $\mathbf{c}_k$ (or, equivalently, control matrices $\mathbf{M}_k$) are chosen so that the DMs replicate, as closely as possible, the three dimensional turbulence structure. Although not shown in Figure 4.3 for clarity, this multiple-DM system still has a single WFS conjugated to the aperture plane.

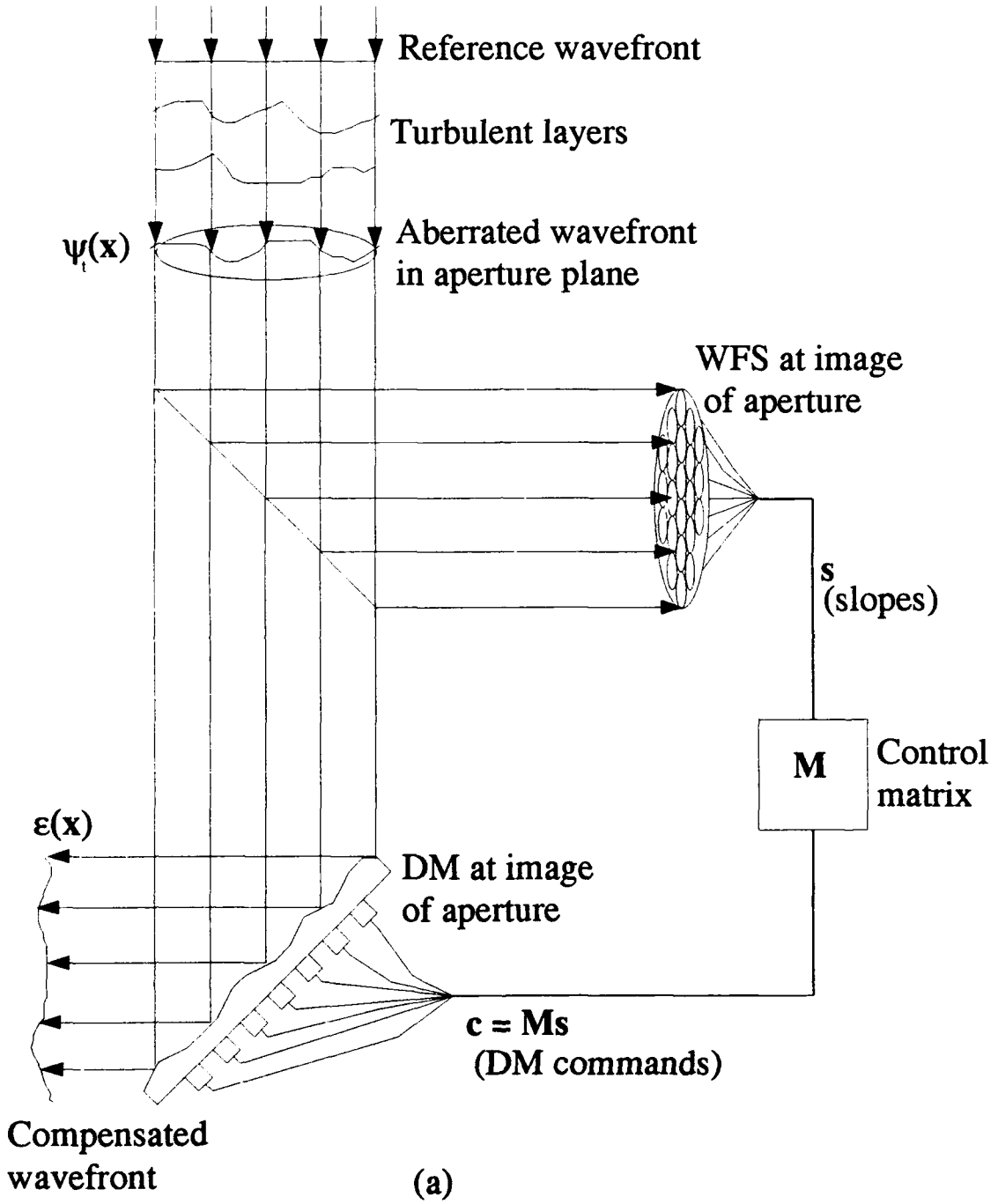

Figure 4.2. Single-DM, open-loop adaptive optical telescope.

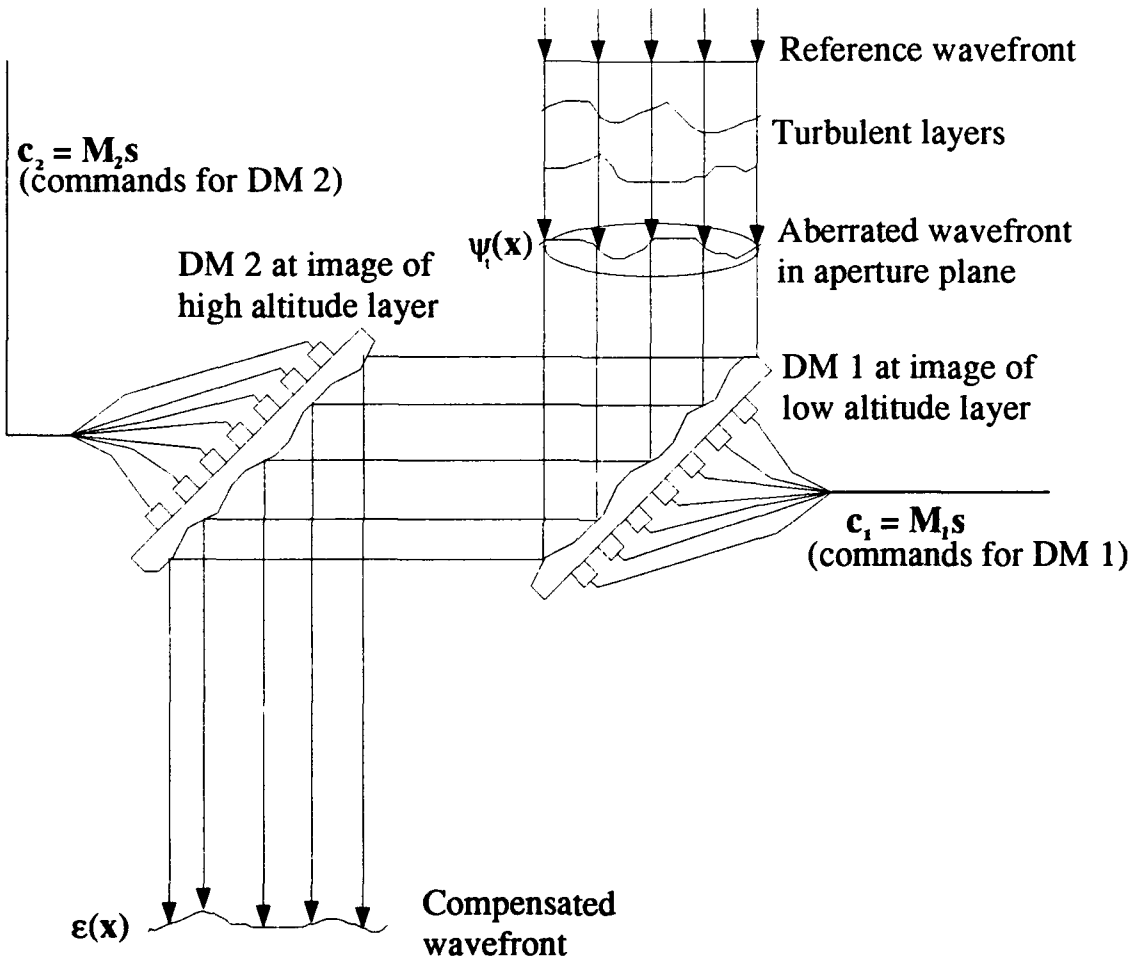

Figure 4.3. Two-DM, open-loop adaptive optical telescope.

4.3.1 Guide stars Multiple guide stars are required for an MCAO telescope for two reasons: 1) to completely sample the turbulence structure throughout the FOV to be compensated (57), and 2) to combine multiple measurements to improve the quality of the estimate of the turbulent layer contributions (5). With M guide stars positioned to project through the turbulence region at different angles, the adaptive optical system will collect an ensemble of M wavefront measurements. In Section 4.4, it is shown that the spatial diversity in the measured wavefronts, along with the geometrical optics assumption, will enable determination of the DM control matrices, $\mathbf{M}_k$, using standard minimum-variance techniques.

Since very few natural stars are bright enough to be used for WFS measurements at visible wavelengths, the guide star array for a multiple-guide-star system must be artificially generated. As discussed in Chapter II, laser beams have already been used to make practical WFS light sources using Rayleigh scattering from air molecules in the troposphere (20) and stimulation of resonance fluorescence in a naturally occurring layer of sodium atoms in the mesosphere (35). Overall tilt information cannot be obtained from the artificial guide stars, since the laser projection system also requires tilt compensation. Rather, natural guide stars are used to provide a reference for tilt-correction with a two-degree-of-freedom, or "tip-tilt" mirror. Since the full aperture may be used for overall tilt sensing, the brightness requirements are not as stringent for the tilt compensation guide star as for the WFS reference. However, to obtain the full benefits of high-order correction, commensurately accurate tilt compensation is required. For this reason, the brightness of the tilt guide star and its proximity to the object are limiting factors on the performance of any laser guide star adaptive optics system, including an MCAO system (16, 51, 54).

The position of each of the M reference stars is described by a two-dimensional vector $\vec{\theta}_m = (\theta_{m_x}, \theta_{m_y})$. The altitude of the guide stars is designated $z_{\mathbf{g}}$. Using equation (4.4), an expression for

the total wavefront phase perturbation in the aperture plane due to guide star m can be written:

$$\psi_{t_m}(\vec{x}) = \sum_{i=1}^{I} \psi_{l_i}\left[\vec{x}\left(1 - \frac{z_{l_i}}{z_g}\right) + z_{l_i}\vec{\theta}_m\right] \tag{4.5}$$

One way to associate the measured wavefronts with their reference sources is by time multiplexing the guide stars. However, it is required that all M phase perturbation measurements be made within the atmosphere's correlation time (27). This requirement clearly limits the number of measurements. Researchers have already demonstrated adaptive optics using sequential wavefront measurements from two artificial guide stars (47). In this experiment, the guide stars were created via Rayleigh backscattered laser light. It is speculated that wavelength multiplexing could be an other possible means of distinguishing the measurements when using Rayleigh guide stars. Sodium guide stars have the advantage of having a much higher altitude, thus reducing the effects of focus anisoplanatism (22). However, since all sodium guide stars have the same wavelength, they cannot be distinguished chromatically.

4.3.2 Wavefront sensor Recall that the proposed MCAO system, although having several DMs, has only one WFS optically conjugated to the telescope pupil. In this section, the WFS is modeled after a Hartmann sensor. This type of WFS outputs the average wavefront gradient over a grid of subapertures. Before modeling the output of the WFS, the aperture-average phase is removed from the mth reference wavefront, $\psi_{t_m}(\vec{x})$ to obtain a piston-removed wavefront, $\varphi_{t_m}(\vec{x})$:

$$\varphi_{t_m}(\vec{x}) = \psi_{t_m}(\vec{x}) - \bar{\psi}_{t_m} \tag{4.6}$$

where the piston mode of the wavefront from the mth guide star, $\bar{\psi}_{t_m}$, is given by

$$\bar{\psi}_{t_m} = \int d^2\vec{x}\, W_i(\vec{x})\psi_{t_m}(\vec{x}) \tag{4.7}$$

and $W_a(\vec{x})$ (m^{-2}) is the weighting function of the telescope aperture, which for convenience is normalized such that

$$\int d^2\vec{x}\, W_a(\vec{x}) = 1 \tag{4.8}$$

Throughout this chapter, the notation φ indicates a wavefront with piston removed over the area of the telescope aperture.

To model the WFS, the telescope aperture is divided into $N/2$ subapertures. Assuming small wavefront deviation over the subaperture, the WFS output can be approximated as the average wavefront gradient over each subaperture (62). Thus, the wavefront sensor output consists of an N-dimensional vector of slope values—the slope in the x and y directions over each subaperture. The nth slope measurement from the mth guide star s_{mn} (rad/m), is described by (62)

$$s_{mn} = -\int d^2\vec{x}\, [\nabla W_n(\vec{x}) \cdot \hat{a}]\, \varphi_{t_m}(\vec{x}) - \nu_{m_a} + \alpha_{mn} \tag{4.9}$$

where

$W_n(\vec{x})$ (m^{-2}) is the weighting function of the subaperture used for slope measurement n,

$\varphi_{t_m}(\vec{x})$ (rad) is the piston-removed wavefront from guide star m,

$\hat{a}$ is the direction of sensitivity of the nth slope sensor ($\hat{x}$ for odd n and $\hat{y}$ for even n),

ν_{m_a} is the overall tilt in the $\hat{a}$ direction during upward propagation,

α_{mn} (rad/m) is the noise in the measurement,

and ∇ is the gradient operator.

As shown in Appendix B, the first term of equation (4.9) is obtained by integrating by parts an expression for the aperture averaged wavefront gradient. It represents the true value of the average slope of $\varphi_{t_m}(\vec{x})$ over the subaperture $W_n(\vec{x})$ while the last term represents measurement noise effects. The second term of equation (4.9) deserves a more detailed discussion. The overall tilt term, ν_{m_a}, is modeled as the best fit plane to the laser beam wavefront after upward propagation to

the scattering layer, given by $\nu_{m_x} x + \nu_{m_y} y$. This term is present because, due to optical reciprocity, the overall tilt experienced by the laser beam on the way up partially cancels that experienced by the guide star wavefront on the downward propagation. The amount of cancellation depends on the size of the laser projection aperture relative to the pupil. It is important to include this "blindness" to overall tilt to obtain accurate results from this analysis. Not including this term is equivalent to assuming that overall tilt information is available in the direction of each guide star, which is unrealistic. Letting a equal x or y, as appropriate, the tilt coefficient is found to be

$$\nu_{m_a} = \frac{\int d^2\vec{x}\, W_{\mathrm{p}}(\vec{x})\, a\varphi_{t_m}(\vec{x})}{\int d^2\vec{x}\, W_{\mathrm{p}}(\vec{x})\, a^2} \tag{4.10}$$

where $W_{\mathrm{p}}(\vec{x})$ (m^{-2}) is the weighting function of the laser projection aperture.

Following the usual practice, the slope measurement noise, α_{mn} is modeled as zero mean and uncorrelated with the turbulence (62). Also, the noise is uncorrelated from subaperture to subaperture and measurement to measurement. Furthermore, the noise added to the x-directed slope is uncorrelated with that added to the y-directed slope, even when measured in the same subaperture. Mathematically,

$$\langle \alpha_{mn} \alpha_{m'n'} \rangle = \sigma_\alpha^2 \delta_{mm'} \delta_{nn'} \tag{4.11}$$

$$\langle \alpha_{mn} \psi_{l_i}(\vec{x}) \rangle \equiv 0 \tag{4.12}$$

where σ_α^2 ($(\mathrm{rad/m})^2$) is the variance of the slope measurement noise and $\delta_{qq'}$ is the Kronecker delta.

4.3.3 Deformable mirrors The mathematical model for the kth DM consists of a collection of J_k two-dimensional actuator influence functions $r_{jk}(\vec{x})$ (m). Physically, these functions represent the shape of the mirror surface when a unit command voltage is applied to the jth actuator on the kth DM, with the other actuators held at their quiescent position. The spatial extent of DM k is indicated by a weighting function, $W_{\mathrm{d}_k}(\vec{x})$ (m^{-2}), which is normalized in the same manner as the

pupil weighting function, $W_a(\vec{x})$. Unlike the case of the single-DM adaptive telescope studied by Welsh and Gardner (63), the DM weighting function is not, in general, the same as the aperture weighting function. As shown in Figure 4.4, to widen the corrected FOV the DM must compensate an area larger than the aperture. The extent of $W_{d_k}(\vec{x})$ is determined by the altitude of the plane conjugate to the kth mirror, z_{d_k} (m), and the FOV of the telescope, β (rad).

4.4 Analysis

The previous sections defined a layered atmospheric model and generalized Wallner's adaptive optics system models to allow for an arbitrary number of guide stars and DMs. This section presents a method which uses the ensemble of wavefront measurements to obtain K sets of DM command voltages. The intent is to construct a three-dimensional correction for atmospheric distortion in the optical train of the telescope. The general approach is to divide the atmosphere into K slabs, corresponding to the available K DMs. The contribution of the kth slab to the total wavefront is called the kth wavefront "component" and designated $\psi_{d_k}(\vec{x})$. The surface of DM k is figured to compensate for the wavefront $\phi_{d_k}(\vec{x})$, where ϕ_{d_k} is the piston- and tilt-removed phase

$$\phi_{d_k}(\vec{x}) = \psi_{d_k}(\vec{x}) - \int d^2\vec{x}\, W_{d_k}(\vec{x})\psi_{d_k}(\vec{x}) - (\nu_{d_{k_x}} x + \nu_{d_{k_y}} y) \tag{4.13}$$

where $\nu_{d_{k_\alpha}}$ is defined in the same way as ν_{m_α} (equation (4.10)) except the DM weighting function is used. (It is desirable to place a piston- and tilt-removed wavefront on the surface of the DM to help ensure that the actuators are not driven beyond the limits of their dynamic range. Recall that overall tilt is compensated by a separate correction system, not by the DMs.) In analyzing the performance of an MCAO system, two types of errors are of interest. The first type is the mean square difference between the desired and actual surfaces of the kth DM. Then an optimum matrix, $\mathbf{M}_k^*$, is chosen to minimize this difference using the phase screen statistics. This reconstruction method is known as the minimum variance approach. To evaluate the performance of the MCAO

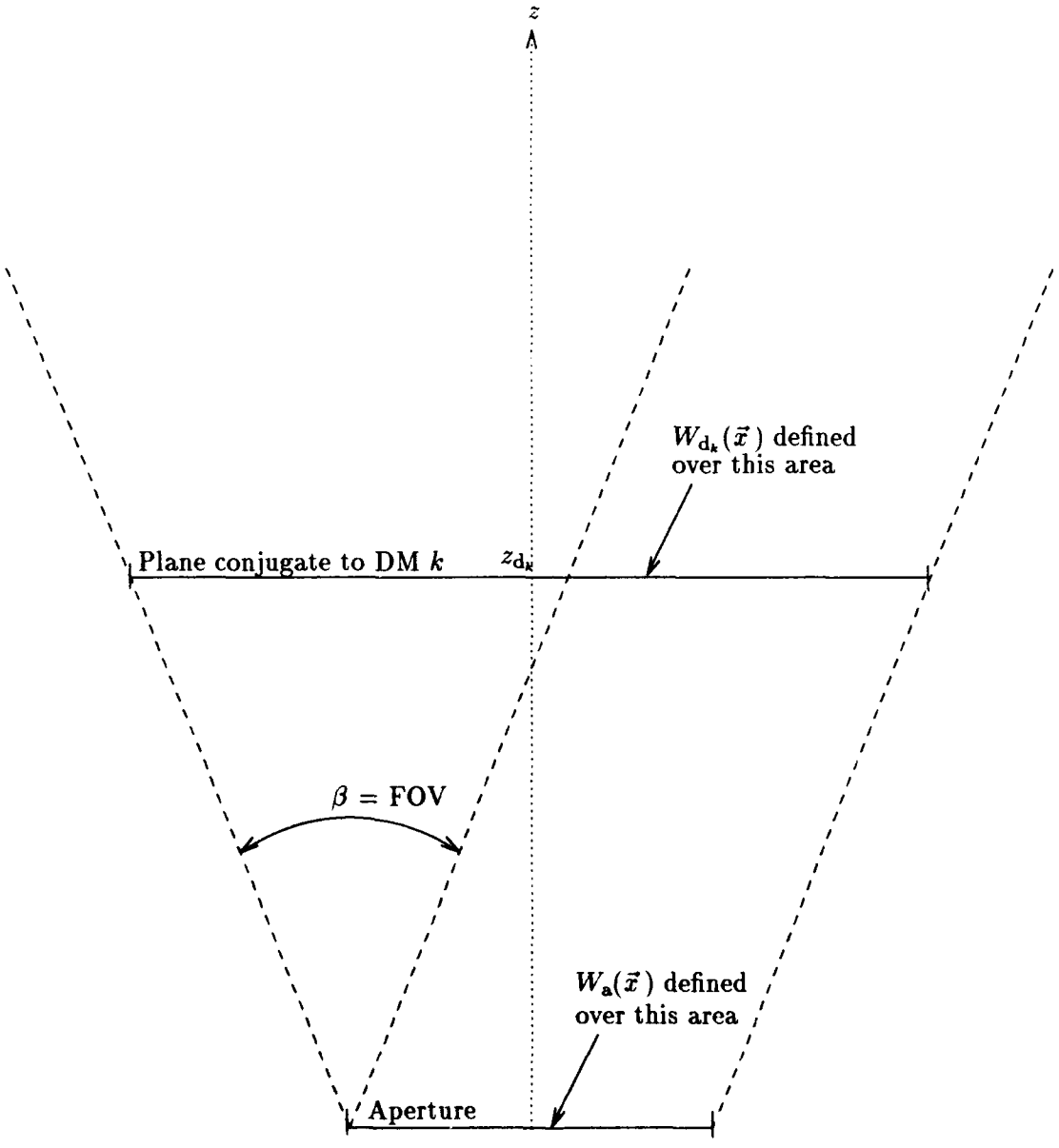

Figure 4.4. Size of DM k weighting function.

system, the second type of error is computed: the average residual phase error in the object wavefront after compensation by all K DMs and the tip-tilt mirror. First, consider the error in the reconstructed wavefront on the individual DMs.

4.4.1 Error in the reconstructed wavefront component Recall that the goal is to have each DM in the MCAO system compensate for the phase distortion effects for a certain portion of the atmosphere. That contribution, or wavefront component, must be reconstructed using the information in the slope measurements from M guide stars and *a priori* knowledge of phase and noise statistics. The analysis in this section results in expression for the reconstructed wavefront component placed on the kth DM. As discussed previously, each wavefront measurement consists of an N-dimensional vector of subaperture slopes, $\mathbf{s}_m$, collected in the aperture plane using guide star m. If there are M guide stars, then altogether there are MN slope measurements. The command voltage c_{jk}, to be applied to actuator j on DM k, is computed from a linear combination of these slope measurements:

$$c_{jk} = \sum_{m=1}^{M} \sum_{n=1}^{N} M_{jkmn} s_{mn} \tag{4.14}$$

where M_{jkmn} is the weight of the nth slope measurement from the mth guide star in the jth actuator command for DM k. In matrix notation,

$$\mathbf{c}_k = \mathbf{M}_k \mathbf{s} \tag{4.15}$$

where the vector $\mathbf{c}_k$ has the individual c_{jk} as its elements and the vector $\mathbf{s}$ contains all MN slope measurements. The matrix $\mathbf{M}_k$ is a $J_k \times MN$ reconstruction matrix for DM k.

After figuring, the surface of DM k may be mathematically described by a linear combination of actuator influence functions $r_{jk}(\vec{x})$. With the actuator commands given by equation (4.15), the surface of the DM forms an estimate of the wavefront component $\phi_{\mathbf{d}_k}(\vec{x})$. Designating this

estimated wavefront, $\hat{\phi}_{\mathrm{d}_k}(\vec{x})$, it may be written as

$$\begin{aligned}\hat{\phi}_{\mathrm{d}_k}(\vec{x}) &= \mathbf{c}_k \cdot \mathbf{r}_k(\vec{x}) \\ &= \mathbf{M}_k \mathbf{s} \cdot \mathbf{r}_k(\vec{x}) \end{aligned} \tag{4.16}$$

where $\mathbf{r}_k(\vec{x})$ is a J_k-dimensional vector of actuator influence functions for DM k.

The error in the reconstructed wavefront component placed on the kth DM, $\epsilon_k(\vec{x})$, may be written

$$\epsilon_k(\vec{x}) = \hat{\phi}_{\mathrm{d}_k}(\vec{x}) - \phi_{\mathrm{d}_k}(\vec{x}) \tag{4.17}$$

The mean square error averaged over the surface of the kth DM is

$$\begin{aligned}\langle \epsilon_k^2 \rangle &= \int d^2\vec{x}\, W_{\mathrm{d}_k}(\vec{x}) \left\langle \left[\hat{\phi}_{\mathrm{d}_k}(\vec{x}) - \phi_{\mathrm{d}_k}(\vec{x})\right]^2 \right\rangle \\ &= \int d^2\vec{x}\, W_{\mathrm{d}_k}(\vec{x}) \left\langle \hat{\phi}_{\mathrm{d}_k}^2(\vec{x}) \right\rangle + \int d^2\vec{x}\, W_{\mathrm{d}_k}(\vec{x}) \left\langle \phi_{\mathrm{d}_k}^2(\vec{x}) \right\rangle \\ &\quad -2 \int d^2\vec{x}\, W_{\mathrm{d}_k}(\vec{x}) \left\langle \hat{\phi}_{\mathrm{d}_k}(\vec{x}) \phi_{\mathrm{d}_k}(\vec{x}) \right\rangle \end{aligned} \tag{4.18}$$

where $W_{\mathrm{d}_k}(\vec{x})$ is the aperture weighting function for DM k. Implicitly, $\langle \epsilon_k^2 \rangle$ is a function of system parameters such as the number and positions of the guide stars, DM actuator density, etc.

By substituting equation (4.16) in equation (4.18), $\langle \epsilon_k^2 \rangle$ can be computed in terms of phase correlations that can be computed using Kolmogorov statistics. The first term of equation (4.18) is the average variance of the kth reconstructed wavefront component:

$$\int d^2\vec{x}\, W_{\mathrm{d}_k}(\vec{x}) \left\langle \hat{\phi}_{\mathrm{d}_k}(\vec{x}) \right\rangle = \mathrm{tr}\left[\mathbf{M}_k^{\mathrm{T}} \mathbf{R}_k \mathbf{M}_k \mathbf{\Sigma}_{ss}\right] \tag{4.19}$$

where tr[·] indicates the trace of the matrix, $\mathbf{\Sigma}_{ss}$ is the slope measurement covariance matrix:

$$\mathbf{\Sigma}_{ss} = \left\langle \mathbf{s}\mathbf{s}^{\mathrm{T}} \right\rangle \tag{4.20}$$

and $\mathbf{R}_k$ is the actuator correlation matrix of the kth DM:

$$\mathbf{R}_k = \int d^2\vec{x}\, W_{\mathrm{d}_k}(\vec{x})\mathbf{r}_k(\vec{x})\mathbf{r}_k^{\mathrm{T}}(\vec{x}) \tag{4.21}$$

The second term of equation (4.18) is the mean square uncorrected phase error of the kth wavefront component, $\langle\epsilon_{0_k}^2\rangle$:

$$\langle\epsilon_{0_k}^2\rangle \;=\; \int d^2\vec{x}\, W_{\mathrm{d}_k}(\vec{x})\,\langle\phi_{\mathrm{d}_k}^2(\vec{x})\rangle \tag{4.22}$$

Finally, the third term of equation (4.18) can be written

$$\int d^2\vec{x}\, W_{\mathrm{d}_k}(\vec{x})\left\langle\hat{\phi}_{\mathrm{d}_k}(\vec{x})\phi_{\mathrm{d}_k}(\vec{x})\right\rangle = \mathrm{tr}\left[\mathbf{A}_k^{\mathrm{T}}\mathbf{M}_k\right] \tag{4.23}$$

where the matrix $\mathbf{A}_k$ is given by

$$\mathbf{A}_k = \int d^2\vec{x}\, W_{\mathrm{d}_k}(\vec{x})\mathbf{r}_k(\vec{x})\langle\mathbf{s}^{\mathrm{T}}\phi_{\mathrm{d}_k}(\vec{x})\rangle \tag{4.24}$$

The final result for the mean square residual phase error in the reconstructed wavefront component on the kth DM is

$$\langle\epsilon_k^2\rangle = \langle\epsilon_{0_k}^2\rangle + \mathrm{tr}\left[\mathbf{M}_k^{\mathrm{T}}\mathbf{R}_k\mathbf{M}_k\boldsymbol{\Sigma}_{ss}\right] - 2\,\mathrm{tr}\left[\mathbf{A}_k^{\mathrm{T}}\mathbf{M}_k\right] \tag{4.25}$$

Note that detailed derivations of the expressions in this section are in Appendix B.

4.4.2 Minimum variance reconstruction method One could suggest a number of ways to derive control matrices for an MCAO system. The method used in this chapter is to independently minimize the mean square residual phase error averaged over the surface of each DM. In other words, equation (4.25) is minimized with respect to the control matrix $\mathbf{M}_k$ to obtain an optimum

control matrix $\mathbf{M}_k^*$ for each DM. As shown in Appendix B, this minimization results in

$$\mathbf{M}_k^* = \mathbf{R}_k^{-1}\mathbf{A}_k\boldsymbol{\Sigma}_{ss}^{-1} \tag{4.26}$$

which is of exactly the same form as Wallner's optimum matrix for a single-DM system (62). Wallner's discussion of the existence conditions for the matrix inverses in equation (4.26) also applies here.

Substitution of equation (4.26) into equation (4.25) yields an expression for the minimum component reconstruction error:

$$\langle\epsilon_k^2\rangle_{\min} = \langle\epsilon_{0_k}^2\rangle - \mathrm{tr}\left[\boldsymbol{\Sigma}_{ss}^{-1}\mathbf{A}_k^{\mathrm{T}}\mathbf{R}_k^{-1}\mathbf{A}_k\right] \tag{4.27}$$

4.4.3 Residual phase error in the compensated object wavefront In the preceding section the mean-square residual error in each wavefront component estimate (i.e. the figured surface of each DM) was derived. This quantity, $\langle\epsilon_k^2\rangle$ is minimized by proper selection of control matrices, $\mathbf{M}_k^*$. The main interest, however, is not how well each wavefront component is estimated, but how well an object wavefront is compensated as a function of its position in the telescope's FOV. Theoretically, if the individual wavefront components are well estimated the object wavefront will be well compensated. In this section, the compensated object wavefront error is evaluated by deriving an expression for the mean-square residual phase error averaged over an object wavefront, after compensation by all K DMs and the tip-tilt mirror. For calculation purposes, it is assumed that the object is a far-field point source. (This is not to imply that the utility of MCAO is limited to point sources. The goal of the MCAO system described in this chapter is to compensate nearby or extended sources as well. For analysis purposes, it is simpler to decompose the object field into a superposition of point sources and evaluate the system performance at selected points.) Using

equation (4.4), the piston-removed wavefront from the object can be written

$$\varphi_o(\vec{x}, \vec{\theta}_o) = \sum_{i=1}^{I} \varphi_{l_i}(\vec{x} + z_{l_i}\vec{\theta}_o) \tag{4.28}$$

where $\vec{\theta}_o$ is the angular position of the object. This wavefront propagates through the optical train of the telescope, reflecting off the tip-tilt mirror and the K DMs in series. The system can be analyzed as if the compensation provided by each DM takes place in its corresponding conjugate plane. Thus, the residual phase error, $\epsilon(\vec{x}, \vec{\theta}_o)$ (rad), of the compensated wavefront can be written:

$$\epsilon(\vec{x}, \vec{\theta}_o) = \sum_{i=1}^{I} \varphi_{l_i}(\vec{x} + z_{l_i}\vec{\theta}_o) - \sum_{k=1}^{K} \bar{\varphi}_{d_k}(\vec{x} + z_{d_k}\vec{\theta}_o) - \hat{\psi}_\tau(\vec{x}) \tag{4.29}$$

where $\hat{\psi}_\tau(\vec{x})$ is the overall tilt correction using a natural star located in the telescope's FOV. Recall that the DMs do not provide overall tilt correction. In the preceding equation, it is important to note that the average phase over the area of the telescope *aperture* must be removed from the DM terms to get accurate results. This is because an arbitrary aperture-sized area on the surface of the DM may have a non-zero average value even though the entire DM surface has zero piston. Of interest is the average mean square residual error for a particular observation angle,

$$\left\langle \epsilon^2(\vec{\theta}_o) \right\rangle = \int d^2\vec{x}\, W_a(\vec{x}) \left\langle \epsilon^2(\vec{x}, \vec{\theta}_o) \right\rangle \tag{4.30}$$

Using a procedure similar to that outlined in the previous section, the following expression is obtained:

$$\begin{aligned} \left\langle \epsilon^2(\vec{\theta}_o) \right\rangle \;=\; & \langle \epsilon_0^2(\theta_o) \rangle + \sum_{k=1}^{K}\sum_{k'=1}^{K} \mathrm{tr}\left[\mathbf{M}_k^{*\mathrm{T}} \mathbf{R}_{kk'}(\vec{\theta}_o) \mathbf{M}_{k'}^{*} \mathbf{\Sigma}_{ss}\right] - 2\sum_{i=1}^{I}\sum_{k=1}^{K} \mathrm{tr}\left[\mathbf{A}_{ik}^{\mathrm{T}}(\vec{\theta}_o)\mathbf{M}_k^{*}\right] \\ & + \int d^2\vec{x}\, W_a(\vec{x}) \langle \hat{\psi}_\tau^2(\vec{x}) \rangle - 2\sum_{i=1}^{I} \int d^2\vec{x}\, W_a(\vec{x}) \left\langle \hat{\psi}_\tau(\vec{x}) \varphi_{l_i}(\vec{x} + z_{l_i}\vec{\theta}_o) \right\rangle \\ & + 2\sum_{k=1}^{K} \int d^2\vec{x}\, W_a(\vec{x}) \mathbf{M}_k^{*} \left\langle \mathbf{s}\hat{\psi}_\tau(\vec{x}) \right\rangle \cdot \mathbf{r}_k(\vec{x} + z_{d_k}\vec{\theta}_o) \end{aligned} \tag{4.31}$$

The first term in the preceding equation is the error in the uncompensated object wavefront:

$$\langle \epsilon_0^2(\theta_o) \rangle = \int d^2\vec{x}\, W_a(\vec{x}) \left\langle \varphi_o^2(\vec{x}, \vec{\theta}_o) \right\rangle \tag{4.32}$$

The matrix $\mathbf{R}_{kk'}(\vec{\theta}_o)$ is of dimension $J_k \times J_{k'}$ and is given by

$$\mathbf{R}_{kk'}(\vec{\theta}_o) = \int d^2\vec{x}\, W_a(\vec{x}) \left[\mathbf{r}_k(\vec{x} + z_{d_k}\vec{\theta}_o) \mathbf{r}_{k'}^T(\vec{x} + z_{d_{k'}}\vec{\theta}_o) \right] - \bar{\mathbf{r}}_k(\vec{\theta}_o) \bar{\mathbf{r}}_{k'}^T(\vec{\theta}_o) \tag{4.33}$$

where

$$\bar{\mathbf{r}}_k(\vec{\theta}_o) = \int d^2\vec{x}\, W_a(\vec{x}) \mathbf{r}_k(\vec{x} + z_{d_{k'}}\vec{\theta}_o) \tag{4.34}$$

The second term in equation (4.33) results from removing the average phase from an aperture-sized area on the surface of the DM. The $\mathbf{A}_{ik}(\vec{\theta}_o)$, (dimension $J_k \times MN$) matrix is defined as

$$\mathbf{A}_{ik}(\vec{\theta}_o) = \int d^2\vec{x}\, W_a(\vec{x}) \mathbf{r}_k(\vec{x} + z_{d_k}\vec{\theta}_o) \left\langle \mathbf{s}^T \varphi_{l_i}(\vec{x} + z_{l_i}\vec{\theta}_o) \right\rangle \tag{4.35}$$

Having derived an expression for the object wavefront error in terms of phase correlations and system parameters, it is now possible to make numerical computations in order to evaluate system performance. Note that Appendix B contains the detailed derivations of the results of this section.

4.5 Numerical Computations

In the preceding sections, a general framework for analyzing a multiple-DM, multiple-guide-star adaptive telescope was developed. The analysis is not completely general in that a particular method for obtaining control matrices was chosen and the amplitude effects of atmospheric turbulence were neglected. However, specifics of the telescope hardware and configuration, as well as noise and phase statistics, have yet to be specified. In this section, a particular telescope is

selected and commonly accepted turbulence and noise statistics are used to perform numerical computations.

4.5.1 Example system To simplify the computations, the telescope is specified to have a square aperture of dimension D (m) divided into a rectangular grid of square subapertures of dimension d (m) where $N = 2(D/d)^2$ is the number of slope measurements. The WFS measures the wavefront gradient averaged over each of these subapertures. Figure 4.5 illustrates the WFS grid for the case of $D/d = 6$. The subaperture size is set equal to the atmospheric coherence diameter, r_0 (17). Similarly, the DMs are square and the DM actuators are arranged in a square grid, with the interactuator spacing on all mirrors equal to r_0. All the actuator response functions are Gaussian-shaped:

$$r_{jk}(x,y) \propto \exp\left\{\frac{-\left[(x-x_{jk})^2+(y-y_{jk})^2\right]}{\rho_{\mathrm{m}}^2}\right\} \tag{4.36}$$

where x_{jk} and y_{jk} are the actuator coordinates in the DM k plane. The mirror influence radius, ρ_{m}, is also set equal to r_0. Two different guide star arrangements are examined: 1) a single guide star located on the optical axis and 2) 4 guide stars positioned symmetrically. The 4-guide-star constellation is illustrated in Figure 4.6.

All guide stars are located in the plane $z = z_{\mathrm{g}}$. The coordinates of the guide star positions in this plane are

$$x_{\mathrm{g}_m} = z_{\mathrm{g}}\theta_{m_x} \tag{4.37}$$

$$y_{\mathrm{g}_m} = z_{\mathrm{g}}\theta_{m_y} \tag{4.38}$$

To generalize the results, the guide star positions are normalized by the subaperture dimension d

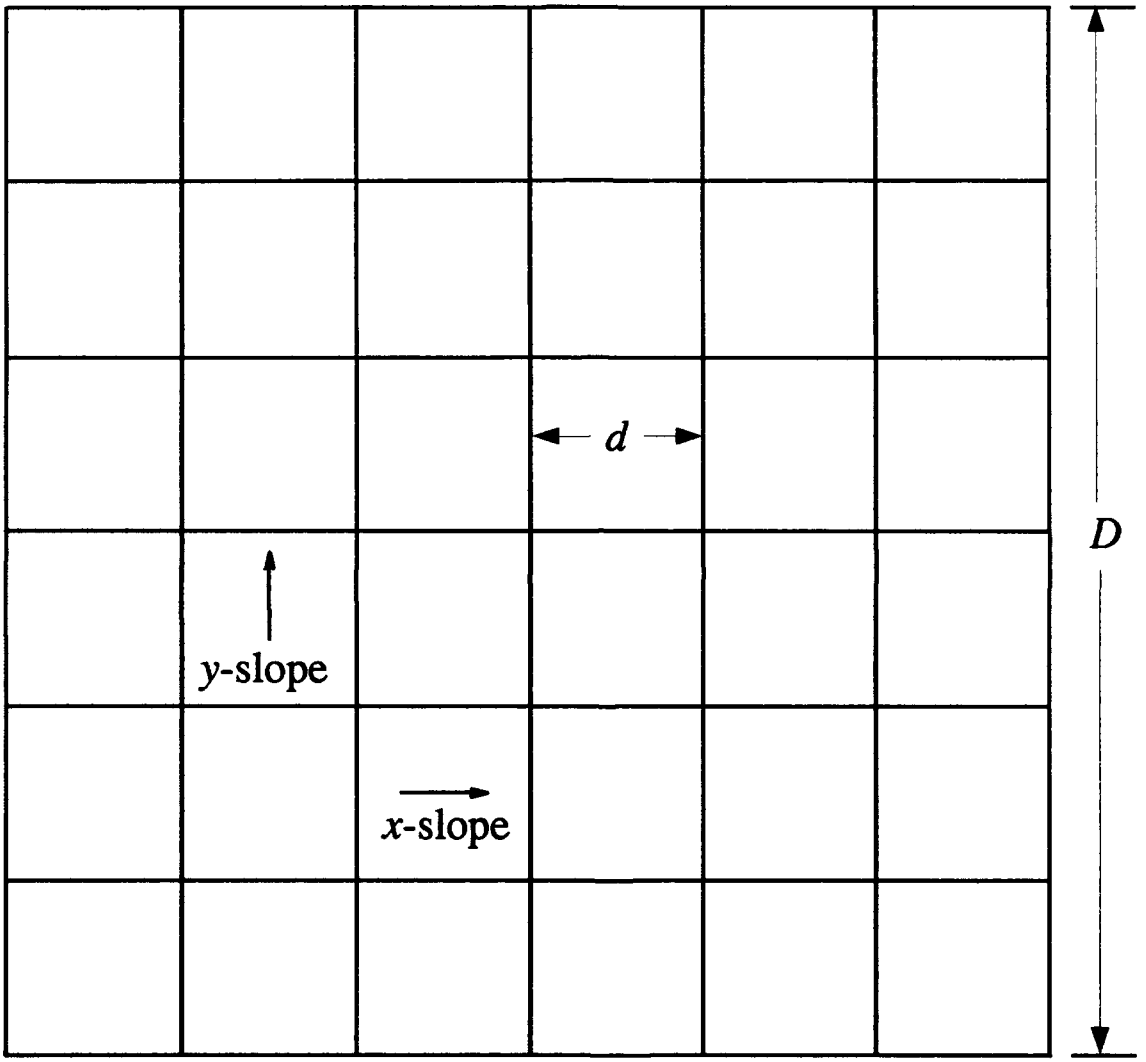

Figure 4.5. Square telescope aperture divided into $N/2$ square subapertures.

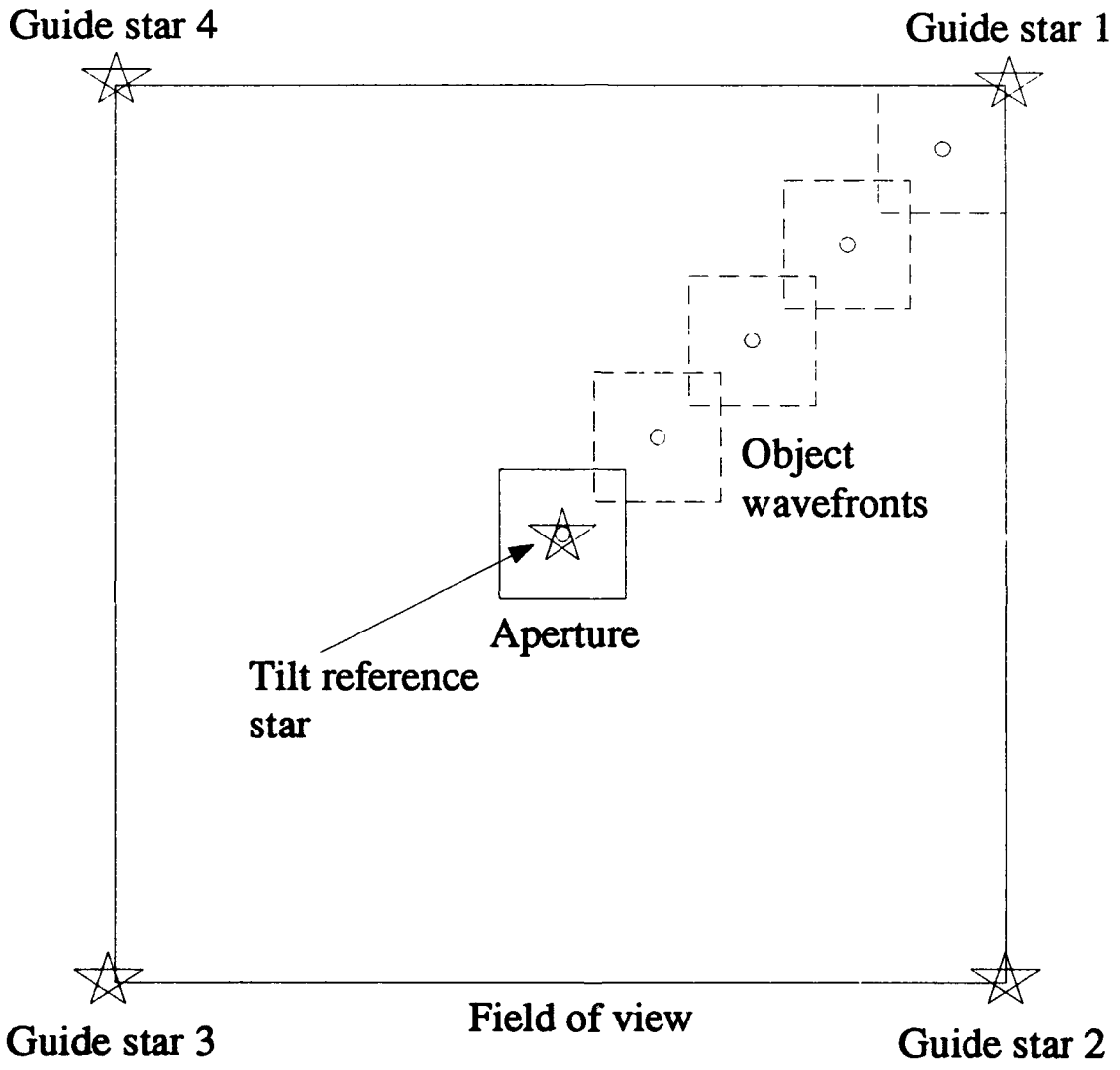

Figure 4.6. Telescope aperture and FOV projected onto the guide star plane where a constellation of 4 guide stars has been projected.

to obtain the dimensionless quantities $\tilde{x}_{g_m}$, $\tilde{y}_{g_m}$:

$$\tilde{x}_{g_m} = \frac{x_{g_m}}{d} \tag{4.39}$$

$$\tilde{y}_{g_m} = \frac{y_{g_m}}{d} \tag{4.40}$$

In the case of the 4-guide-star array, the guide stars are located at the points $(\tilde{x}_g, \tilde{y}_g)$, $(\tilde{x}_g, -\tilde{y}_g)$, $(-\tilde{x}_g, -\tilde{y}_g)$, $(-\tilde{x}_g, \tilde{y}_g)$. A similar set of normalized coordinates, $(\tilde{x}_r, \tilde{y}_r)$, is defined for the natural tilt reference star. Finally, the normalized object coordinates are

$$\tilde{x}_o = \frac{z_g \theta_{o_x}}{d} \tag{4.41}$$

$$\tilde{y}_o = \frac{z_g \theta_{o_y}}{d} \tag{4.42}$$

where θ_{o_x} and θ_{o_y} (rad) are the x and y components of the object angle vector. As illustrated in Figure 4.6, the mean square residual phase error of the compensate object wavefront is evaluated as a function of position along a diagonal line from the optical axis toward one of the corners. The maximum allowed object coordinates are determined by the FOV of the telescope which is specified by the angle β (see Figure 4.7). These maximum coordinates are designated $(\tilde{x}_\beta, \tilde{y}_\beta)$:

$$\tilde{x}_\beta = \tilde{y}_\beta = \frac{z_g \beta}{2d} \tag{4.43}$$

For the 4-guide-star array to probe the entire FOV, the normalized guide star locations need to be

$$\tilde{x}_g = \frac{D}{2d} + \tilde{x}_\beta \tag{4.44}$$

$$\tilde{y}_g = \frac{D}{2d} + \tilde{y}_\beta \tag{4.45}$$

The conjugate plane to DM k is defined to be at the altitude $z = z_{\mathrm{d}_k}$ (m). This altitude is normalized by the guide star altitude to obtain the dimensionless quantity $\tilde{z}_{\mathrm{d}_k}$:

$$\tilde{z}_{\mathrm{d}_k} = \frac{z_{\mathrm{d}_k}}{z_{\mathrm{g}}} \tag{4.46}$$

As illustrated in Figure 4.7, the size of DM k, D_k (m), is given by

$$D_k = D + 2d\tilde{z}_{\mathrm{d}_k}\tilde{x}_\beta \tag{4.47}$$

where small angle approximations have been used.

The final system specification is the determination of the wavefront components, $\phi_{\mathrm{d}_k}(\vec{x})$. As explained earlier, $\phi_{\mathrm{d}_k}(\vec{x})$ is that portion of the total wavefront aberration which DM k is intended to compensate. As shown in Figure 4.8, DM k is assigned the wavefront phase contribution of a slab of atmosphere, $\mathcal{S}_k$. (In this dissertation, the problems of how to best divide the atmosphere into slabs and how the conjugate planes are chosen are not addressed.) The wavefront component $\phi_{\mathrm{d}_k}(\vec{x})$ is defined to be the sum of the turbulent layers $\phi_{\mathrm{l}_i}(\vec{x})$ contained within slab $\mathcal{S}_k$:

$$\phi_{\mathrm{d}_k}(\vec{x}) = \sum_{i \in \mathcal{S}_k} \phi_{\mathrm{l}_i}(\vec{x}) \tag{4.48}$$

4.5.2 Phase statistics As explained previously, the ith turbulent layer alters the phase of a plane wave propagating through it according to a phase perturbation function $\psi_{\mathrm{l}_i}(\vec{x})$ (rad), where $\vec{x} = (x, y)$ (m) is a position vector in the plane of the layer. For computational purposes, this function is assumed to be a sample function of a random process which is described by the Kolmogorov structure function $\mathcal{D}_i(\vec{x}, \vec{x}')$ (rad^2) (64):

$$\mathcal{D}_i(\vec{x}, \vec{x}') = \left\langle [\phi_{\mathrm{l}_i}(\vec{x}) - \phi_{\mathrm{l}_i}(\vec{x}')]^2 \right\rangle = 6.88 \left(\frac{|\vec{x} - \vec{x}'|}{r_i} \right)^{5/3} \tag{4.49}$$

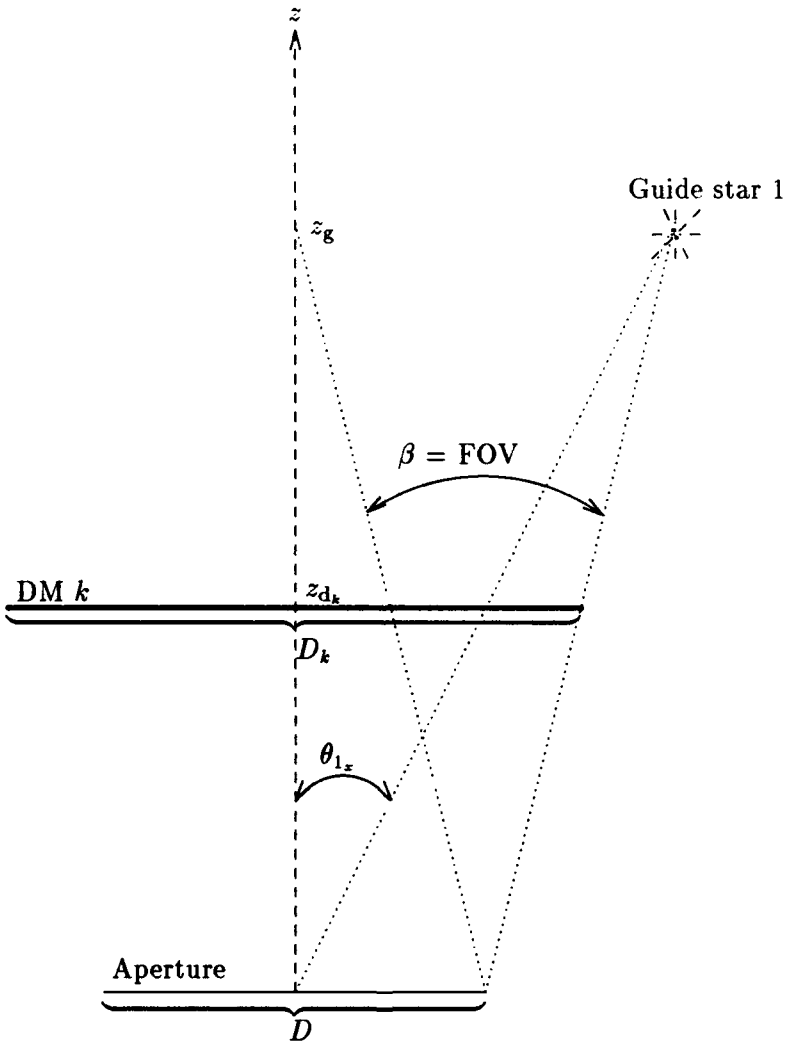

Figure 4.7. Size of DM k.

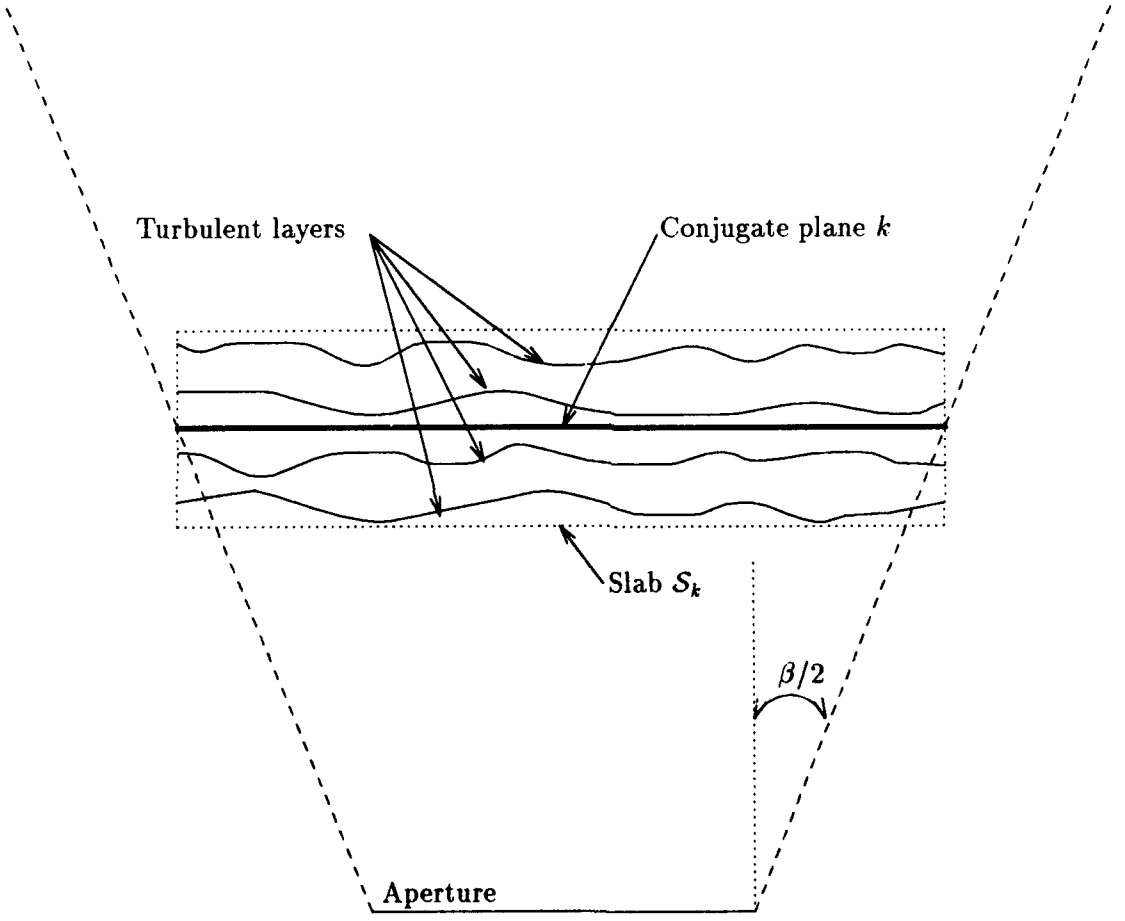

Figure 4.8. Portion of the atmosphere assigned to DM k.

where the angle brackets indicate an ensemble average. The parameter r_i (m) is the turbulent layer's coherence diameter. The r_i are related to r_0, the overall atmospheric coherence diameter, by the formula (5)

$$r_0^{-5/3} = \sum_{i=1}^{I} r_i^{-5/3} \tag{4.50}$$

It is also convenient to characterize the turbulent layer as having a fraction, q_i, of the total turbulence strength:

$$q_i = \left(\frac{r_i}{r_0}\right)^{-5/3} \tag{4.51}$$

and to define a normalized layer altitude $\tilde{z}_{l_i}$:

$$\tilde{z}_{l_i} = \frac{z_{l_i}}{z_g} \tag{4.52}$$

4.5.3 Noise statistics Welsh and Gardner quantified the slope measurement error due to photon noise associated with a Hartmann-Shack WFS (63):

$$\sigma_\alpha = \begin{cases} \dfrac{0.86\pi\eta}{N_{\text{ph}}^{1/2} r_0} & d > r_0 \\ & \text{rad/m} \\ \dfrac{0.74\pi\eta}{N_{\text{ph}}^{1/2} d} & d \leq r_0 \end{cases} \tag{4.53}$$

where N_{ph} is the total subaperture photon count and η is a detector efficiency factor which is ≥ 1. In the computations in this chapter, $\eta = 1.35$ was used. Kane *et al.* give this value as that associated with an efficient charge-coupled device array preceded by an image intensifier (40).

4.6 Results

In this section, the analysis method described in Section 4.4 and the assumptions in Section 4.5 are used to present numerical results for single-DM and multiple-DM adaptive optics systems

imaging through a 2-layer atmosphere. The 2-layer model is composed of a low-altitude turbulent layer containing 90% of the turbulence strength located at 1% of the guide star altitude, and an upper layer having the remaining 10% of the turbulence at 10% of z_g. The MCAO system used for these computations is composed of a WFS, 2 DMs and 4 guide stars. The WFS is a 6×6 grid of square subapertures, with subaperture dimension $d = r_0$. For all computations, a photon count of $N_{ph} = 50$ photons per subaperture was assumed. The 4 guide stars are arranged in the constellation shown in Figure 4.6, with $\tilde{x}_g = \tilde{y}_g = 22.5$. (This value was chosen because it corresponds to 50 μrad when $d = 0.2$ m and $z_g = 90$ km, the nominal altitude of the sodium layer.) The tilt reference star is located at the origin. A side view of the geometry is depicted in Figure 4.9. As shown in the figure, DM 1 must cover an area 1.065 times as large as the telescope aperture, while DM 2 is 1.65 times the size of the pupil. Due to the fact that the DM areas are larger than the aperture area, as well as the finite height of the guide stars, each guide star probes only a fraction of each turbulent layer. Figures 4.10 and 4.11 illustrate how a portion of each layer will be sampled by all 4 guide stars, other sections will contribute to 2 guide star wavefronts, and some areas are probed by only one of the guide stars. In the case of layer 1, each guide star probes 86% of the area of DM 1, with 74% of the area common to all 4 measurements and 24% common to 2 of the 4 measurements. Figure 4.11 shows that the larger area of DM 2 is not probed as thoroughly by the 4-guide-star array: only 1% of the area is common to all 4 measurements and 16% common to 2 measurements. Table 4.1 summarizes the atmospheric and system parameters used in the computations of this section.

Using the parameters in Table 4.1, the optimum control matrices for the 2-DM system were found using equation (4.26). Then the object wavefront error was evaluated at 5 points in the FOV along the diagonal line shown in Figure 4.6. The results are shown in Figure 4.12. For comparison, the object error at the same points for a single-DM, single-guide-star system is also plotted. For this "conventional" adaptive optical telescope, the DM is optically conjugated to the pupil and the guide star is located on the optical axis. To allow a fair comparison with the 4-guide-star system,

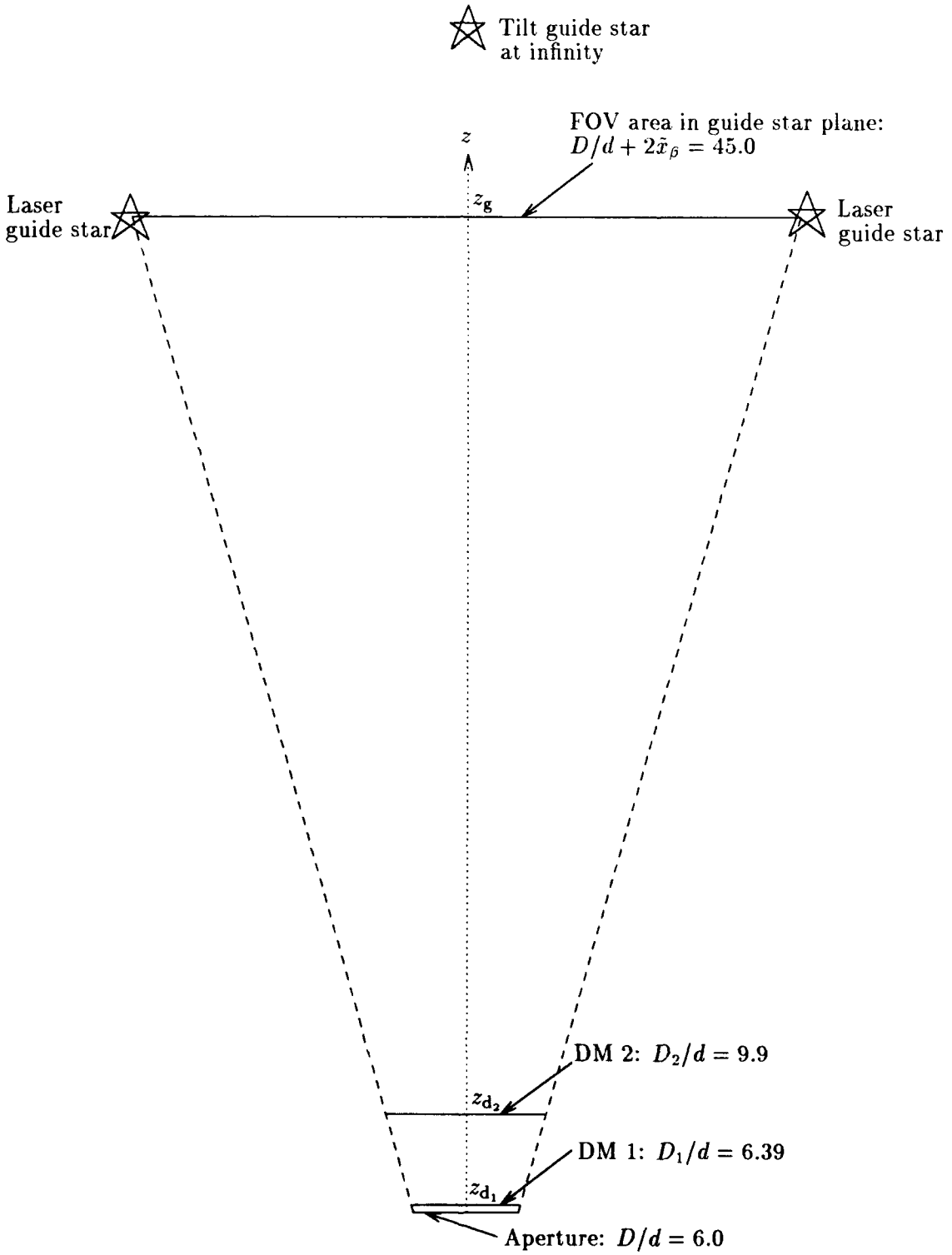

Figure 4.9. DM sizes when conjugated to the turbulent layers described in Table 4.1.

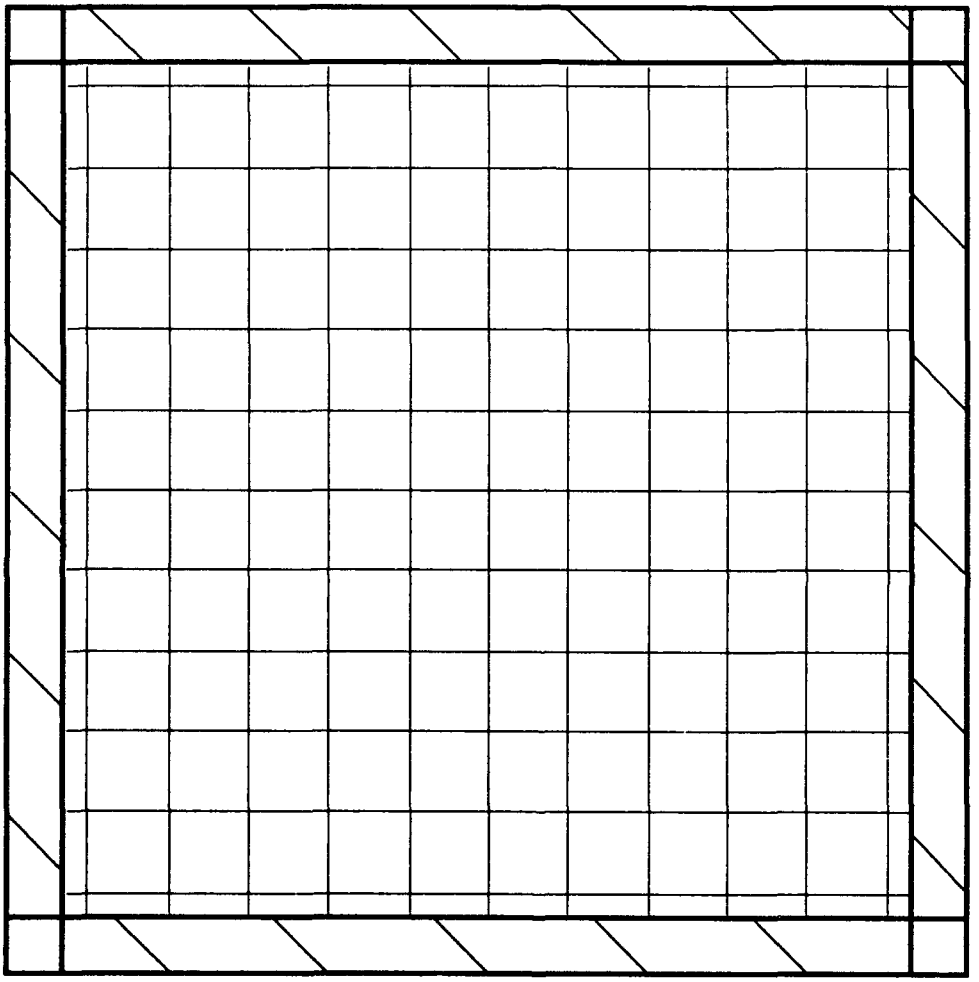

Figure 4.10. Areas of turbulent layer 1 probed by each guide star in 4-guide-star array. The double-cross-hatched area is probed by all 4 guide stars, the single cross-hatched area is probed by 2 guide stars, while the small non-cross-hatched square areas in each corner are probed by only one guide star.

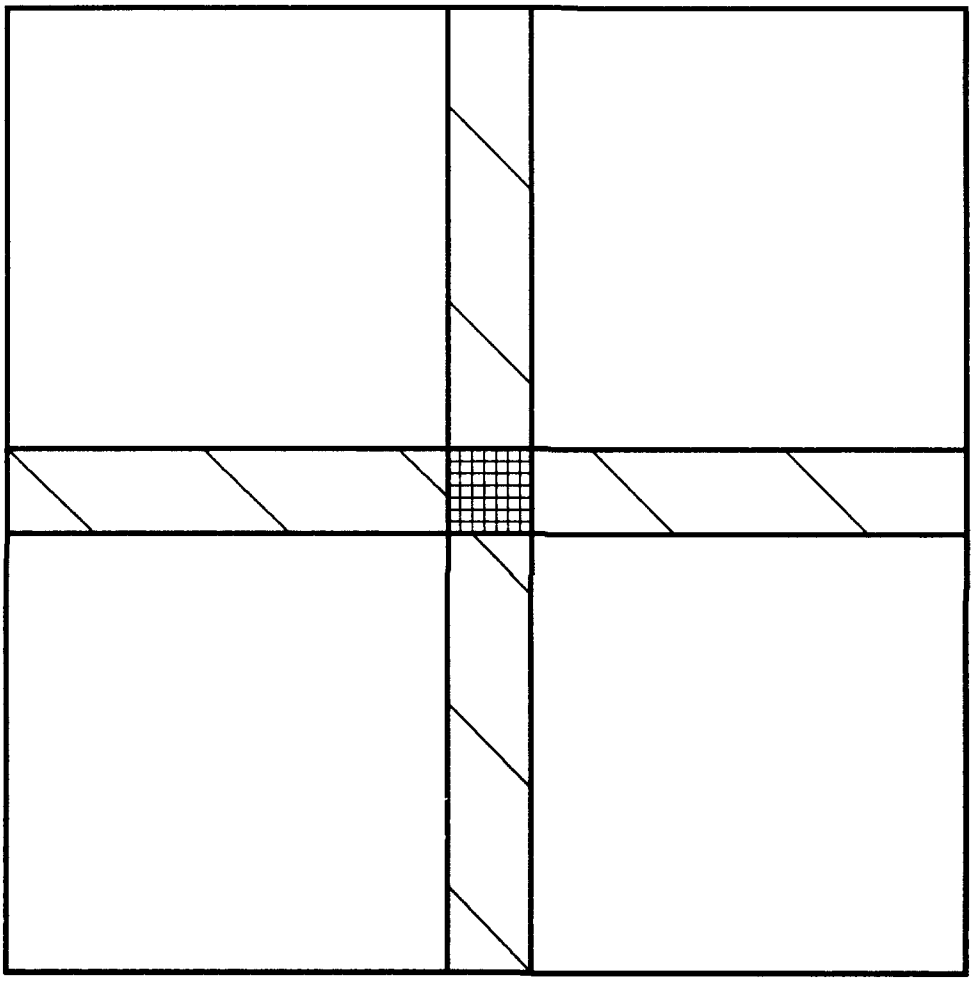

Figure 4.11. Areas of layer 2 probed by each guide star in 4-guide-star array. The double-cross-hatched area is probed by all 4 guide stars, the single cross-hatched area is probed by 2 guide stars, while the non-cross-hatched square areas in each corner are probed by only one guide star.

Parameter	Symbol	Value
Number of turbulent layers	I	2
Normalized altitude of turbulent layer 1	$\tilde{z}_{l_1}$	0.01
Fraction of turbulence strength in layer 1	q_1	0.90
Normalized altitude of turbulent layer 2	$\tilde{z}_{l_2}$	0.10
Fraction of turbulence strength in layer 2	q_2	0.10
Ratio of aperture to subaperture size	D/d	6.0
Ratio of subaperture to seeing cell size	d/r_0	1.0
WFS efficiency factor	η	1.35
Detected photons per subaperture	N_{ph}	50
Number of DMs	K	2
Normalized altitude of conjugate plane 1	$\tilde{z}_{\mathrm{d}_1}$	0.01
Normalized altitude of conjugate plane 2	$\tilde{z}_{\mathrm{d}_2}$	0.10
Guide star positions	$\tilde{x}_{\mathrm{g}}, \tilde{y}_{\mathrm{g}}$	22.5
Maximum object coordinates	$\tilde{x}_\beta, \tilde{y}_\beta$	19.5
Tilt reference star position	$\tilde{x}_{\mathrm{r}}, \tilde{y}_{\mathrm{r}}$	0.

Table 4.1. Parameters for MCAO problem.

4 measurements from the single guide star were combined (which reduces the measurement noise power by a factor of 4). For both systems, overall tilt was compensated by removing the best-fit plane from an on-axis natural guide star from the object wavefront (errors in the tilt compensation system were not modeled, but tilt anisoplanatism is properly accounted for since the tilt reference star and object point are not necessarily in the same location). The figure indicates that the MCAO system is able to compensate its entire FOV to an rms residual phase error of $\lambda/7$. However, the single-DM system outperforms the MCAO system for object points out to about 1/3 of the way from the optical axis to the corner of the FOV. The single-DM system does very well in the neighborhood of the optical axis since its single guide star is located there. In effect, the single-DM system is designed to optimize performance along a single observation direction—in the direction of the single reference. By comparison, the multiconjugate system, in this implementation, does not optimize for a particular observation direction but attempts to compensate the entire FOV as well as possible. As a result, a system which has an optimum observation direction has better performance in that direction, at the expense of worse performance in other directions.

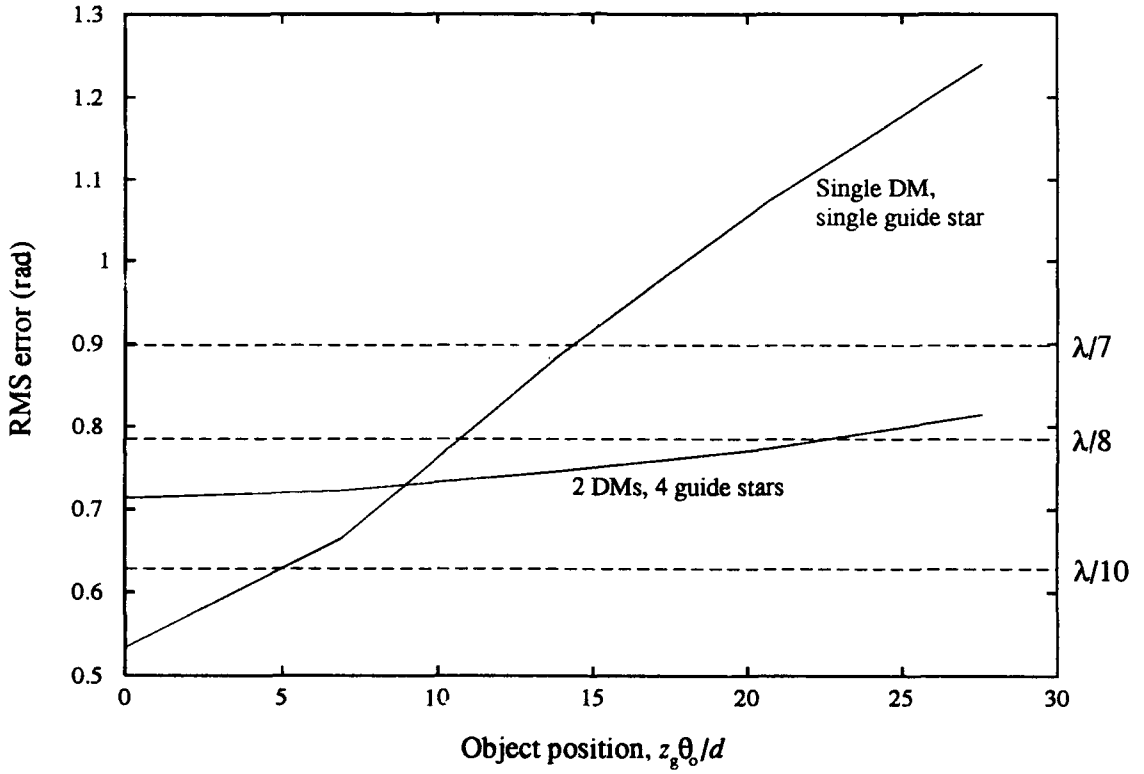

Figure 4.12. RMS residual phase error averaged over object wavefront vs. object position for 2-DM adaptive telescope with 4 guide stars compared with "conventional" single-DM system.

Figure 4.13 illustrates the effect of laser guide star tilt blindness. In this figure, the performance of the 2-DM, 4-laser-guide-star system is compared with a hypothetical system employing 4 reference sources (e.g. 4 sufficiently bright natural stars in just the right locations) that also provide overall tilt information. This hypothetical system does not use a separate tip-tilt mirror, but corrects the tilt component using the DMs. From examination of the figure, we see that tilt anisoplanatism significantly limits the performance of a realistic MCAO system.

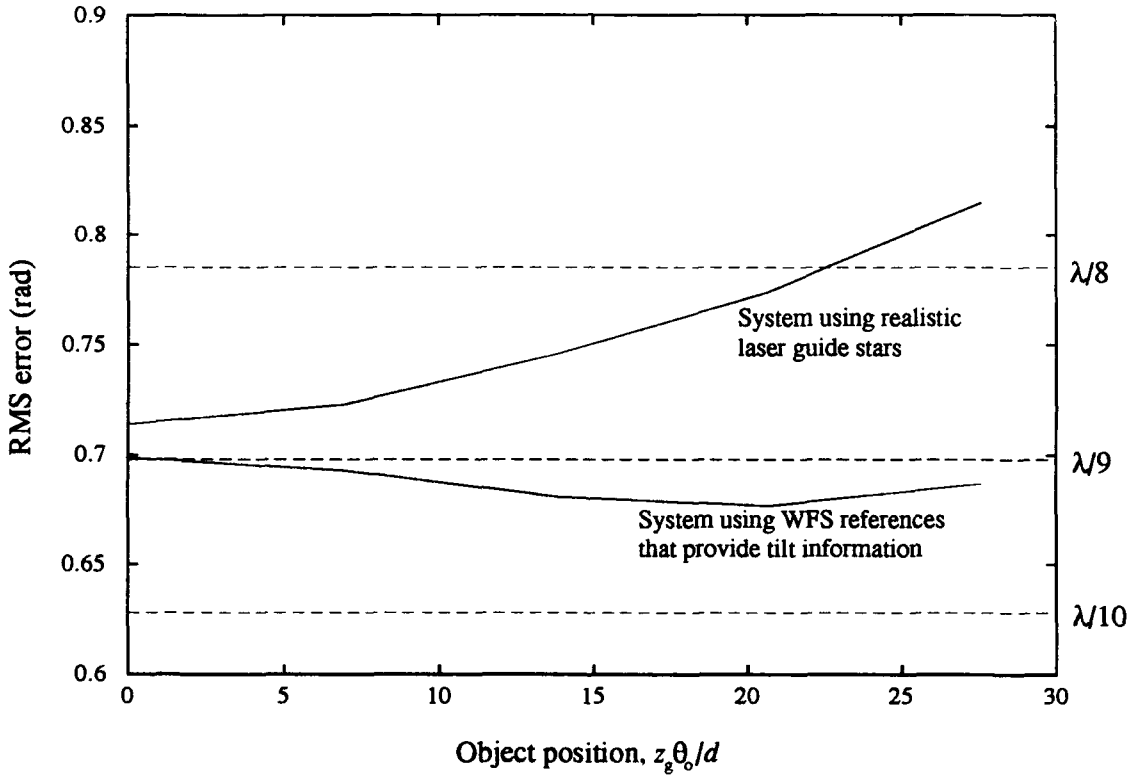

Figure 4.13. Performance of 2-DM system with multiple WFS reference sources that provide overall tilt information compared with system using laser guide stars providing only higher-order phase information.

One might expect that we could improve on a "conventional" adaptive telescope design, by conjugating the mirror to a plane closer to the turbulence. In Figure 4.14, three cases are compared corresponding to the DM conjugated to 1) the aperture 2) the strongest turbulent layer, and 3) the center of gravity (CG) of the turbulence profile. The results show that, for this 2-layer

atmosphere, slightly better performance is obtained if the DM is conjugated to the aperture when the FOV criterion is average rms residual phase error $< \lambda/8$. However, conjugating the mirror to the strongest turbulent layer is better for object points more than one-third of the way to the edge of the FOV. In this case, conjugating the DM to the center of gravity of the turbulence profile is the least effective choice. The 2-DM system appears to work better than either of the single-DM alternatives.

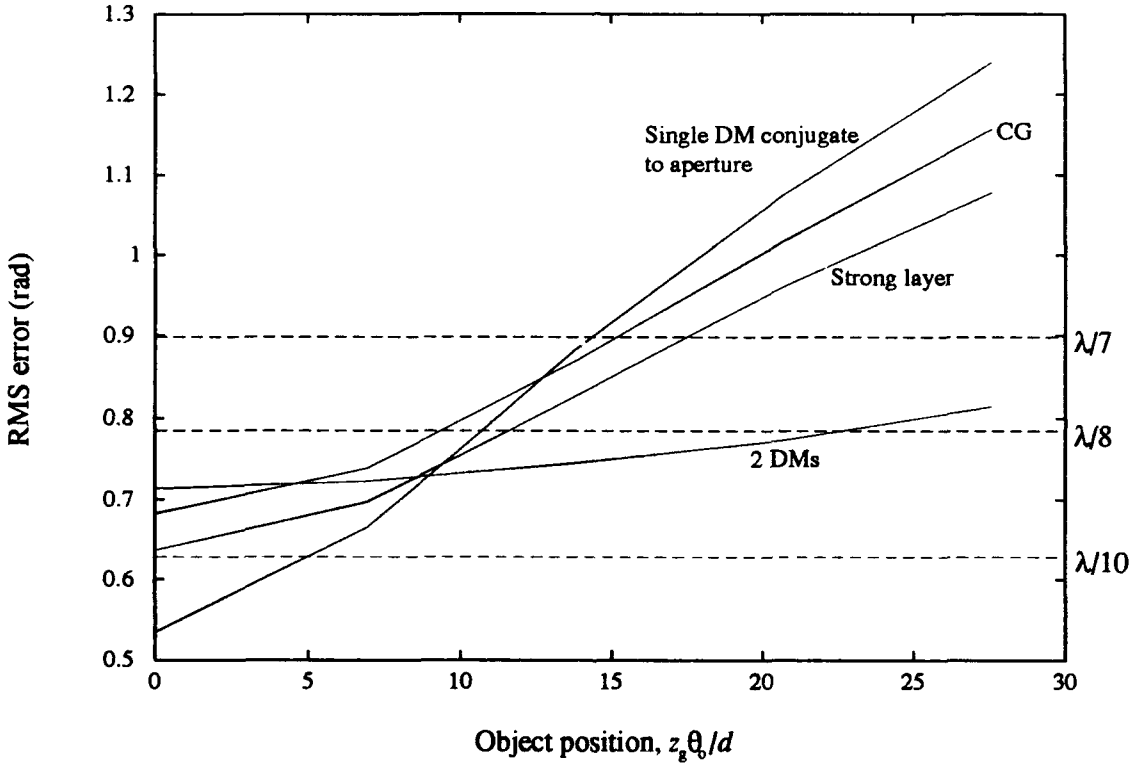

Figure 4.14. RMS residual phase error averaged over object wavefront vs. object position for single-DM adaptive telescope and various choices of DM position, compared with 2-DM system. For the single-DM cases with the DM conjugated to the strongest layer and the turbulence center of gravity, the 4 guide star constellation was used.

4.7 Summary

Wallner's adaptive optics system analysis method has been generalized to allow for an arbitrary number of guide stars, DMs, and atmospheric layers. This method can be used to compute

analytical performance predictions for a variety of adaptive optics problems. The chief limitation is the impracticality of computing results for large telescopes due to excessive computation time. However, the technique does provide further insight into the performance of various adaptive telescope system configurations imaging through different atmospheres. The results show that multiple-DM systems do hold promise for widening the compensated FOV, provided that multiple wavefront measurements from different guide star locations can be made before the atmosphere changes significantly. Performance of an MCAO system is still limited by tilt anisoplanatism, since tilt information is not obtainable from the artificial guide stars.

V. *Conclusions and Recommendations*

5.1 Major Results

The major results of this research effort are the following:

1) Development of an analytical method for estimating the contribution of a portion of the turbulent atmosphere to the total optical wavefront distortion resulting from propagation through the entire atmosphere.

2) Development of a practical method of controlling an arbitrary number of DMs in an adaptive optical telescope to achieve a useful level of phase compensation over a wide FOV.

3) The first analytical performance prediction for a multiple-DM, multiple-laser-guide star telescope imaging through a layered atmosphere incorporating the integrated effects of WFS noise; angular, focus, and tilt anisoplanatism; finite aperture sizes; DM influence functions; and laser guide star tilt blindness.

4) Quantitative results showing that multiple DMs and multiple artificial guide stars can be used to increase the compensated FOV of an adaptive optical telescope under good observing conditions.

5) Quantitative results showing the effect of conjugating a single DM to various choices for correction planes, as compared with the addition of a second DM.

6) Quantitative results showing the effect of laser guide star tilt blindness on the performance of a wide-FOV adaptive optics system.

5.2 Discussion

One way to quantify the compensated FOV for an adaptive optical telescope is to specify the area over which a particular level of residual phase error is achieved. Two examples of such

FOV criteria are residual phase error levels less than $\lambda/7$ or $\lambda/8$. Figure 4.12 shows that, for the 2-layer atmosphere studied in Chapter IV, a 2-DM system increases the compensated area by a factor of 4 for either of these FOV criteria. If $d = r_0 = 0.2$ m, these results show that a 1.2 meter 2-DM adaptive optical telescope with 4 sodium-layer guide stars can compensate a square FOV 90 microradians (18 arcsec) on a side to a level of residual phase error $< \lambda/8$, vs. 45 microradians (9 arcsec) for the single-DM system. If the FOV criterion is $\lambda/7$, the MCAO system can compensate a FOV 135 microradians (28 arcsec) vs. 70 microradians (14 arcsec) for the single-DM system. This value of r_0 might be seen under excellent observing conditions at visible wavelengths. At infrared wavelengths, a typical value of r_0 is 0.5 meters. Hence, the plots in Chapter IV apply to a 3 meter telescope imaging in the infrared and the compensated areas increase accordingly.

Continuing this example, the importance of laser guide star tilt blindness may be illustrated. According to Figure 4.13, if laser guide stars did not have this limitation, the 2-DM telescope could compensate the larger area (i.e. 135 microradians on a side) to $\lambda/9$ instead of $\lambda/7$. This corresponds to an increase in the Strehl ratio from 0.45 to 0.61.

5.2.1 Recommendations for Future Work Several areas remain to be investigated in the study of MCAO systems.

5.2.2 Wave Optics Diffraction alters the phase aberration function in the telescope aperture due to turbulence at a distance. Also, propagation over a significant distance causes some of the phase effects to convert to amplitude effects (scintillation). An interesting question remaining to be answered is whether conjugating the DMs in an adaptive telescope to correction planes close to the turbulence can reduce scintillation in the telescope aperture.

5.2.3 Temporal Effects The refractive index of the atmosphere is a temporal as well as a spatial random process. Since a finite amount of time elapses between wavefront measurement and correction, degradation in the level of compensation results. In a multiple guide star system that

collects the WFS measurements sequentially, the different guide star measurements in the ensemble will be slightly different due to the time delay between measurements.

5.2.4 Closed Loop Control Closed loop control has been successfully achieved for single-DM, single-guide-star adaptive optics systems. Closed loop control of multiple-DM systems could be troublesome due to the optical coupling among the DMs.

5.2.5 Wide Field Tilt Compensation The results of this dissertation show if we are to approach the full theoretical potential of MCAO systems, a means of sensing the overall tilt component from a variety of directions in the FOV is required.

Appendix A. *Derivation of Equations in Chapter III*

A.1 Expected Value of Product of Convolutions

In the following section, the expected value of the product of two-dimensional convolutions is needed. In the subsequent derivation, all random processes are assumed to be wide sense stationary.

$$\begin{aligned}
&\langle [f_1(x_1,y_1) * *g_1(x_1,y_1)]\,[f_2(x_2,y_2) * *g_2(x_2,y_2)]\rangle \\
&\quad = \int d\xi_1 \int d\eta_1 \int d\xi_2 \int d\eta_2 \,\langle f_1(x_1-\xi_1, y_1-\eta_1) f_2(x_2-\xi_2, y_2-\eta_2)\rangle\, g_1(\xi_1,\eta_1) g_2(\xi_2,\eta_2) \\
&\quad = \int d\xi_1 \int d\eta_1 \int d\xi_2 \int d\eta_2 \,\Gamma_{f_1 f_2}(x_1-\xi_1-x_2+\xi_2, y_1-\eta_1-y_2+\eta_2) \\
&\qquad \times g_1(\xi_1,\eta_1) g_2(\xi_2,\eta_2) \qquad\qquad (A.1)
\end{aligned}$$

Letting $\Delta x = x_1 - x_2$ and $\Delta y = y_1 - y_2$,

$$\begin{aligned}
&\langle [f_1(x_1,y_1) * *g_1(x_1,y_1)]\,[f_2(x_2,y_2) * *g_2(x_2,y_2)]\rangle \\
&\quad = \int d\xi_1 \int d\eta_1 \int d\xi_2 \int d\eta_2 \,\Gamma_{f_1 f_2}(\Delta x+\xi_2-\xi_1, \Delta y+\eta_2-\eta_1) g_1(\xi_1,\eta_1) g_2(\xi_2,\eta_2) \\
&\quad = \int d\xi_2 \int d\eta_2 \,[\Gamma_{f_1 f_2}(\Delta x+\xi_2, \Delta y+\eta_2) * *g_1(\Delta x+\xi_2, \Delta y+\eta_2)]\, g_2(\xi_2,\eta_2) \\
&\quad = \Gamma_{f_1 f_2}(\Delta x, \Delta y) * *g_1(\Delta x, \Delta y) * *g_2(-\Delta x, -\Delta y) \qquad (A.2)
\end{aligned}$$

A.2 Equation (3.27)

In this section the autocorrelation function of the wavefront component estimate, $\Gamma_{\hat{\varphi}_{1_i}}(\vec{x})$, is derived. The development begins with equation (3.25), which is the expression for the wavefront

component estimate.

$$
\begin{aligned}
\Gamma_{\hat{\varphi}_{l_i}}(\vec{x}) &= \langle \varphi_{l_i}(\vec{x}' + \vec{x}) \hat{\varphi}_{l_i}(\vec{x}') \rangle \\
&= \left\langle \sum_{m=1}^{M} \left[\sum_{i'=1}^{I} \varphi_{l_i,i'}(\vec{x}' + \vec{x} + z_{l_i,i'} \vec{\theta}_m) + \eta_m(\vec{x}' + \vec{x}) \right] * * h_{\mathrm{sa}}(\vec{x}' + \vec{x}) * * h_{\mathrm{w}_{i,m}}(\vec{x}' + \vec{x}) \right. \\
&\quad \left. \times \sum_{m'=1}^{M} \left[\sum_{i''=1}^{I} \varphi_{l_i,i''}(\vec{x}' + z_{l_i,i''} \vec{\theta}_{m'}) + \eta_{m'}(\vec{x}') \right] * * h_{\mathrm{sa}}(\vec{x}') * * h_{\mathrm{w}_{i,m'}}(\vec{x}') \right\rangle \\
&= \sum_{m=1}^{M} \sum_{m'=1}^{M} \left\langle \left[\sum_{i'=1}^{I} \varphi_{l_i,i'}(\vec{x}' + \vec{x} + z_{l_i,i'} \vec{\theta}_m) + \eta_m(\vec{x}' + \vec{x}) \right] * * h_{\mathrm{sa}}(\vec{x}' + \vec{x}) * * h_{\mathrm{w}_{i,m}}(\vec{x}' + \vec{x}) \right. \\
&\quad \left. \times \left[\sum_{i''=1}^{I} \varphi_{l_i,i''}(\vec{x}' + z_{l_i,i''} \vec{\theta}_{m'}) + \eta_{m'}(\vec{x}') \right] * * h_{\mathrm{sa}}(\vec{x}') * * h_{\mathrm{w}_{i,m'}}(\vec{x}') \right\rangle
\end{aligned} \tag{A.3}
$$

Using equation (A.2) from the preceding section,

$$
\begin{aligned}
&\Gamma_{\hat{\varphi}_{l_i}}(\vec{x}) = \\
&\quad \sum_{m=1}^{M} \sum_{m'=1}^{M} \left\langle \left[\sum_{i'=1}^{I} \varphi_{l_i,i'}(\vec{x}' + \vec{x} + z_{l_i,i'} \vec{\theta}_m) + \eta_m(\vec{x}' + \vec{x}) \right] \left[\sum_{i''=1}^{I} \varphi_{l_i,i''}(\vec{x}' + z_{l_i,i''} \vec{\theta}_{m'}) + \eta_{m'}(\vec{x}') \right] \right\rangle \\
&\quad * * h_{\mathrm{sa}}(\vec{x}) * * h_{\mathrm{sa}}(-\vec{x}) * * h_{\mathrm{w}_{i,m}}(\vec{x}) * * h_{\mathrm{w}_{i,m'}}(-\vec{x})
\end{aligned} \tag{A.4}
$$

Using the mutual independence of random processes $\varphi_{l_i}(\vec{x})$ and $\eta_m(\vec{x})$. and the fact that convolution distributes over addition (23):

$$
\begin{aligned}
&\Gamma_{\hat{\varphi}_{l_i}}(\vec{x}) = \\
&\quad \sum_{m=1}^{M} \left\{ \sum_{m'=1}^{M} \sum_{i'=1}^{I} \Gamma_{\varphi_{l_i,i'}} \left[\vec{x} + z_{l_i,i'}(\vec{\theta}_m - \vec{\theta}_{m'}) \right] * * h_{\mathrm{sa}}(\vec{x}) * * h_{\mathrm{sa}}(-\vec{x}) * * h_{\mathrm{w}_{i,m}}(\vec{x}) * * h_{\mathrm{w}_{i,m'}}(-\vec{x}) \right. \\
&\quad \left. + \Gamma_{\eta}(\vec{x}) * * h_{\mathrm{sa}}(\vec{x}) * * h_{\mathrm{sa}}(-\vec{x}) * * h_{\mathrm{w}_{i,m}}(\vec{x}) * * h_{\mathrm{w}_{i,m}}(-\vec{x}) \right\} \\
&= \sum_{m=1}^{M} \left\{ \sum_{m'=1}^{M} \sum_{i'=1}^{I} \Gamma_{\varphi_{l_i,i'}} \left[\vec{x} + z_{l_i,i'}(\vec{\theta}_m - \vec{\theta}_{m'}) \right] * * h_{\mathrm{w}_{i,m}}(\vec{x}) * * h_{\mathrm{w}_{i,m'}}(-\vec{x}) \right. \\
&\quad \left. + \Gamma_{\eta}(\vec{x}) * * h_{\mathrm{w}_{i,m}}(\vec{x}) * * h_{\mathrm{w}_{i,m}}(-\vec{x}) \right\} * * h_{\mathrm{sa}}(\vec{x}) * * h_{\mathrm{sa}}(-\vec{x})
\end{aligned} \tag{A.5}
$$

A.3 Equation (3.39)

Substituting equations (3.31) and (3.34) into equation (3.30), the mean square error expression becomes

$$\epsilon^2 = \sigma^2_{\varphi_{i_1}} + \int_{-fsa}^{fsa}\int_{-fsa}^{fsa} df_x\, df_y \left\{ 2\Phi_{\varphi_{i_1}} \left[|\tilde{h}_{w_{11}}|^2 + |\tilde{h}_{w_{12}}|^2 + \mathrm{Re}\left\{ \tilde{h}_{11}\tilde{h}^*_{12}\tilde{h}_{w_{11}}\tilde{h}^*_{w_{12}} \right\} \right.\right.$$
$$\left.\left. + \mathrm{Re}\left\{ \tilde{h}_{21}\tilde{h}^*_{22}\tilde{h}_{w_{11}}\tilde{h}^*_{w_{12}} \right\} - \left(\tilde{h}_{11}\tilde{h}_{w_{11}} + \tilde{h}_{12}\tilde{h}_{w_{12}} \right) \right] + \Phi_\eta \left(|\tilde{h}_{w_{11}}|^2 + |\tilde{h}_{w_{12}}|^2 \right) \right\} \quad \text{(A.6)}$$

Assumption (3.32) means that

$$\tilde{h}^*_{12} = \tilde{h}_{11} \quad \text{(A.7)}$$

$$\tilde{h}^*_{22} = \tilde{h}_{21} \quad \text{(A.8)}$$

$$\tilde{h}_{12} = \tilde{h}^*_{11} \quad \text{(A.9)}$$

With these substitutions, the integrand of equation (A.6) becomes

$$2\Phi_{\varphi_{i_1}} \left[|\tilde{h}_{w_{11}}|^2 + |\tilde{h}_{w_{12}}|^2 + \mathrm{Re}\left\{ \tilde{h}^2_{11}\tilde{h}_{w_{11}}\tilde{h}^*_{w_{12}} \right\} + \mathrm{Re}\left\{ \tilde{h}^2_{21}\tilde{h}_{w_{11}}\tilde{h}^*_{w_{12}} \right\} - \left(\tilde{h}_{11}\tilde{h}_{w_{11}} + \tilde{h}^*_{11}\tilde{h}_{w_{12}} \right) \right]$$
$$+ \Phi_\eta \left(|\tilde{h}_{w_{11}}|^2 + |\tilde{h}_{w_{12}}|^2 \right) \quad \text{(A.10)}$$

Assumption (3.33) means that

$$\tilde{h}_{21} = \tilde{h}^2_{11} \quad \text{(A.11)}$$

This final substitution leads to equation (3.39).

Appendix B. *Derivation of Equations in Chapter IV*

B.1 Equation (4.9)

The derivation of the first term of equation 4.9 is shown for x-directed slopes. The procedure is exactly the same for the y-slope. The x-directed slope from the mth guide star measured in the nth subaperture is the gradient of the total phase in the x-direction averaged over the subaperture:

$$\begin{aligned} s_{mn_x} &= \int d^2\vec{x}\, W_n(\vec{x})\,[\nabla\varphi_{t_m}(\vec{x})\cdot\hat{x}] \\ &= \int_{-\infty}^{\infty} dy \int_{-\infty}^{\infty} dx\, W_n(x,y)\frac{\partial\varphi_{t_m}(x,y)}{\partial x} \end{aligned} \tag{B.1}$$

Using integration by parts on the x integral with

$$\begin{aligned} u &= W_n(x,y) \\ du &= \frac{\partial W_n(x,y)}{\partial x}dx \\ v &= \varphi_{t_m}(x,y) \\ dv &= \frac{\partial\varphi_{t_m}(x,y)}{\partial x}dx \end{aligned}$$

equation (B.1) becomes

$$s_{mn_x} = \int_{-\infty}^{\infty} dy \left\{ W_n(x,y)\varphi_{t_m}(x,y)\Big|_{-\infty}^{\infty} - \int_{-\infty}^{\infty} dx\, \frac{\partial W_n(x,y)}{\partial x}\varphi_{t_m}(x,y) \right\} \tag{B.2}$$

The first term of the preceding equation is 0 since the subaperture has finite size, which implies $W_n(x,y) = 0$ at infinity. Thus,

$$\begin{aligned} s_{mn_x} &= -\int_{-\infty}^{\infty} dy \int_{-\infty}^{\infty} dx\, \frac{\partial W_n(x,y)}{\partial x}\varphi_{t_m}(x,y) \\ &= -\int d^2\vec{x}\,[\nabla W_n(\vec{x})\cdot\hat{x}]\,\varphi_{t_m}(\vec{x}) \end{aligned} \tag{B.3}$$

B.2 Equation (4.19)

Substituting equation (4.16) into the first term of equation (4.18),

$$\begin{aligned}
\int d^2\vec{x}\, W_{\mathrm{d}_k}(\vec{x}) \left\langle \hat{\phi}^2_{\mathrm{d}_k}(\vec{x}) \right\rangle &= \int d^2\vec{x}\, W_{\mathrm{d}_k}(\vec{x}) \left\langle \mathbf{M}_k\mathbf{s}\cdot\mathbf{r}_k(\vec{x})\mathbf{M}_k\mathbf{s}\cdot\mathbf{r}_k(\vec{x})\right\rangle \\
&= \int d^2\vec{x}\, W_{\mathrm{d}_k}(\vec{x}) \left\langle \mathbf{r}_k(\vec{x})\cdot\mathbf{M}_k\mathbf{s}\mathbf{M}_k\mathbf{s}\cdot\mathbf{r}_k(\vec{x})\right\rangle \\
&= \int d^2\vec{x}\, W_{\mathrm{d}_k}(\vec{x}) \left\langle \mathbf{r}_k^{\mathrm{T}}(\vec{x})\mathbf{M}_k\mathbf{s}\mathbf{s}^{\mathrm{T}}\mathbf{M}_k^{\mathrm{T}}\mathbf{r}_k(\vec{x})\right\rangle \\
&= \int d^2\vec{x}\, W_{\mathrm{d}_k}(\vec{x})\mathbf{r}_k^{\mathrm{T}}(\vec{x})\mathbf{M}_k \left\langle \mathbf{s}\mathbf{s}^{\mathrm{T}}\right\rangle \mathbf{M}_k^{\mathrm{T}}\mathbf{r}_k(\vec{x}) \\
&= \int d^2\vec{x}\, W_{\mathrm{d}_k}(\vec{x})\mathbf{r}_k^{\mathrm{T}}(\vec{x})\mathbf{M}_k\boldsymbol{\Sigma}_{ss}\mathbf{M}_k^{\mathrm{T}}\mathbf{r}_k(\vec{x}) \qquad \text{(B.4)}
\end{aligned}$$

For two vectors $\mathbf{b}$ and $\mathbf{c}$ having the same number of elements (6):

$$\mathbf{c}^{\mathrm{T}}\mathbf{b} = \mathrm{tr}\left[\mathbf{b}\mathbf{c}^{\mathrm{T}}\right] \qquad \text{(B.5)}$$

Letting

$$\begin{aligned}
\mathbf{b} &= \boldsymbol{\Sigma}_{ss}\mathbf{M}_k^{\mathrm{T}}\mathbf{r}_k(\vec{x}) \\
\mathbf{c}^{\mathrm{T}} &= \mathbf{r}_k^{\mathrm{T}}(\vec{x})\mathbf{M}_k
\end{aligned}$$

equation (B.4) becomes

$$\begin{aligned}
\int d^2\vec{x}\, W_{\mathrm{d}_k}(\vec{x}) \left\langle \hat{\phi}^2_{\mathrm{d}_k}(\vec{x}) \right\rangle &= \int d^2\vec{x}\, W_{\mathrm{d}_k}(\vec{x})\mathrm{tr}\left[\boldsymbol{\Sigma}_{ss}\mathbf{M}_k^{\mathrm{T}}\mathbf{r}_k(\vec{x})\mathbf{r}_k^{\mathrm{T}}(\vec{x})\mathbf{M}_k\right] \\
&= \mathrm{tr}\left[\boldsymbol{\Sigma}_{ss}\mathbf{M}_k^{\mathrm{T}}\mathbf{R}_k\mathbf{M}_k\right] \\
&= \mathrm{tr}\left[\mathbf{M}_k^{\mathrm{T}}\mathbf{R}_k\mathbf{M}_k\boldsymbol{\Sigma}_{ss}\right] \qquad \text{(B.6)}
\end{aligned}$$

since for any square matrix $\mathbf{B}$

$$\mathrm{tr}\left[\mathbf{B}\right] = \mathrm{tr}\left[\mathbf{B}^{\mathrm{T}}\right] \qquad \text{(B.7)}$$

In the final step of equation (B.6), the symmetry of the $\mathbf{\Sigma}_{ss}$ and $\mathbf{R}_k$ matrices was used.

B.3 Equation (4.23)

Substituting equation (4.16) into the third term of equation (4.18),

$$\begin{aligned}
\int d^2\vec{x}\, W_{\mathrm{d}_k}(\vec{x}) \left\langle \hat{\phi}_{\mathrm{d}_k}(\vec{x}) \phi_{\mathrm{d}_k}(\vec{x}) \right\rangle &= \int d^2\vec{x}\, W_{\mathrm{d}_k}(\vec{x}) \left\langle \mathbf{M}_k \mathbf{s} \cdot \mathbf{r}_k(\vec{x}) \phi_{\mathrm{d}_k}(\vec{x}) \right\rangle \\
&= \int d^2\vec{x}\, W_{\mathrm{d}_k}(\vec{x}) \left\langle \mathbf{s}^{\mathrm{T}} \mathbf{M}_k^{\mathrm{T}} \mathbf{r}_k(\vec{x}) \phi_{\mathrm{d}_k}(\vec{x}) \right\rangle \\
&= \int d^2\vec{x}\, W_{\mathrm{d}_k}(\vec{x}) \left\langle \mathrm{tr}\left[\mathbf{r}_k(\vec{x}) \phi_{\mathrm{d}_k}(\vec{x}) \mathbf{s}^{\mathrm{T}} \mathbf{M}_k^{\mathrm{T}} \right] \right\rangle \\
&= \int d^2\vec{x}\, W_{\mathrm{d}_k}(\vec{x}) \mathrm{tr}\left[\mathbf{r}_k(\vec{x}) \left\langle \phi_{\mathrm{d}_k}(\vec{x}) \mathbf{s}^{\mathrm{T}} \right\rangle \mathbf{M}_k^{\mathrm{T}} \right] \\
&= \mathrm{tr}\left[\mathbf{A}_k \mathbf{M}_k^{\mathrm{T}} \right] \qquad \text{(B.8)}
\end{aligned}$$

If a matrix $\mathbf{B}$ is of order $(i \times j)$ and a matrix $\mathbf{C}$ is of order $(j \times i)$ then (6):

$$\mathrm{tr}[\mathbf{BC}] = \mathrm{tr}[\mathbf{CB}] \qquad \text{(B.9)}$$

Hence, equation (B.8) may be written in several forms:

$$\begin{aligned}
\int d^2\vec{x}\, W_{\mathrm{d}_k}(\vec{x}) \left\langle \hat{\phi}_{\mathrm{d}_k}(\vec{x}) \phi_{\mathrm{d}_k}(\vec{x}) \right\rangle &= \mathrm{tr}\left[\mathbf{M}_k^{\mathrm{T}} \mathbf{A}_k \right] \\
&= \mathrm{tr}\left[\mathbf{A}_k^{\mathrm{T}} \mathbf{M}_k \right] \qquad \text{(B.10)}
\end{aligned}$$

B.4 Equation (4.26)

The derivation of the minimizing control matrix starts with equation (4.25) in its summation form:

$$\left\langle \epsilon_k^2 \right\rangle = \left\langle \epsilon_{0_k}^2 \right\rangle + \sum_j \sum_{j'} \sum_n \sum_{n'} M_{jn} R_{jj'} M_{j'n'} \Sigma_{n'n} - 2 \sum_j \sum_n A_{jn} M_{jn} \qquad \text{(B.11)}$$

The minimizing control matrix is found by setting the first derivative of the preceding equation, with respect to an arbitrary element of the matrix, equal to zero. Consider element M_{kl}:

$$\begin{aligned}\langle \epsilon_k^2 \rangle &= \langle \epsilon_{0_k}^2 \rangle + \sum_{j'} \sum_{n'} M_{kl} R_{j'k} M_{j'n'} \Sigma_{n'l} + \sum_{j} \sum_{n} M_{jn} R_{jk} M_{kl} \Sigma_{ln} - 2A_{kl} M_{kl} \\ &\quad + [\text{terms not multiplied by } M_{kl}] \end{aligned} \tag{B.12}$$

The derivative with respect to M_{kl} is

$$\frac{\partial \langle \epsilon_k^2 \rangle}{\partial M_{kl}} = \sum_{j'} \sum_{n'} R_{j'k} M_{j'n'} \Sigma_{n'l} + \sum_{j} \sum_{n} R_{jk} M_{jn} \Sigma_{ln} - 2A_{kl} \tag{B.13}$$

Setting the preceding equation equal to zero and writing in matrix form results in

$$\mathbf{RM\Sigma} = \mathbf{A} \tag{B.14}$$

Solving for $\mathbf{M}^*$:

$$\mathbf{M}^* = \mathbf{R}^{-1}\mathbf{A}\Sigma^{-1} \tag{B.15}$$

To show that this stationary point is a minimum, the second derivative may be examined:

$$\frac{\partial^2 \langle \epsilon_k^2 \rangle}{\partial M_{kl}^2} = 2R_{kk}\Sigma_{ll} > 0 \tag{B.16}$$

Since equation (4.25) is quadratic in $\mathbf{M}_k$, it is a global minimum.

B.5 Equation (4.33)

Substituting equation (4.16) into equation (4.29) (with the tilt correction term dropped) and removing the piston in the wavefront estimate yields

$$\begin{aligned}\epsilon(\vec{x},\vec{\theta}_{\rm o}) &= \sum_{i=1}^{I}\varphi_{{\rm l}_i}(\vec{x}+z_{{\rm l}_i}\vec{\theta}_{\rm o}) - \sum_{k=1}^{K}\left[\mathbf{M}_k\mathbf{s}\cdot\mathbf{r}_k(\vec{x}+z_{{\rm d}_k}\vec{\theta}_{\rm o}) - \int d^2\vec{x}\,W_{\rm a}(\vec{x})\mathbf{M}_k\mathbf{s}\cdot\mathbf{r}_k(\vec{x}+z_{{\rm d}_k}\vec{\theta}_{\rm o})\right] \\ &= \sum_{i=1}^{I}\varphi_{{\rm l}_i}(\vec{x}+z_{{\rm l}_i}\vec{\theta}_{\rm o}) - \sum_{k=1}^{K}\mathbf{M}_k\mathbf{s}\cdot\left[\mathbf{r}_k(\vec{x}+z_{{\rm d}_k}\vec{\theta}_{\rm o}) - \bar{\mathbf{r}}_k(\vec{\theta}_{\rm o})\right] \qquad \text{(B.17)}\end{aligned}$$

Substituting the preceding equation into equation (4.30) and following the same procedure as in Sections B.2 and B.3:

$$\begin{aligned}\left\langle\epsilon^2(\vec{\theta}_{\rm o})\right\rangle &= \epsilon_0^2(\theta_{\rm o}) + \int d^2\vec{x}\,W_{\rm a}(\vec{x}) \\ &\quad\times\sum_{k=1}^{K}\sum_{k'=1}^{K}\left\langle\mathbf{M}_k\mathbf{s}\cdot\left[\mathbf{r}_k(\vec{x}+z_{{\rm d}_k}\vec{\theta}_{\rm o}) - \bar{\mathbf{r}}_k(\vec{\theta}_{\rm o})\right]\mathbf{M}_{k'}\mathbf{s}\cdot\left[\mathbf{r}_{k'}(\vec{x}+z_{{\rm d}_{k'}}\vec{\theta}_{\rm o}) - \bar{\mathbf{r}}_{k'}(\vec{\theta}_{\rm o})\right]\right\rangle \\ &\quad -2\int d^2\vec{x}\,W_{\rm a}(\vec{x})\sum_{i=1}^{I}\sum_{k=1}^{K}\left\langle\mathbf{M}_k\mathbf{s}\cdot\left[\mathbf{r}_k(\vec{x}+z_{{\rm d}_k}\vec{\theta}_{\rm o}) - \bar{\mathbf{r}}_k(\vec{\theta}_{\rm o})\right]\varphi_{{\rm l}_i}(\vec{x}+z_{{\rm l}_i}\vec{\theta}_{\rm o})\right\rangle \\ &= \int d^2\vec{x}\,W_{\rm a}(\vec{x})\,{\rm tr}\left\{\mathbf{\Sigma}_{ss}\mathbf{M}_k^{\rm T}\left[\mathbf{r}_k(\vec{x}+z_{{\rm d}_k}\vec{\theta}_{\rm o}) - \bar{\mathbf{r}}_k(\vec{\theta}_{\rm o})\right]\left[\mathbf{r}_{k'}(\vec{x}+z_{{\rm d}_{k'}}\vec{\theta}_{\rm o}) - \bar{\mathbf{r}}_{k'}(\vec{\theta}_{\rm o})\right]^{\rm T}\mathbf{M}_k\right\} \\ &\quad -2\int d^2\vec{x}\,W_{\rm a}(\vec{x})\sum_{i=1}^{I}\sum_{k=1}^{K}{\rm tr}\left\{\left[\mathbf{r}_k(\vec{x}+z_{{\rm d}_k}\vec{\theta}_{\rm o}) - \bar{\mathbf{r}}_k(\vec{\theta}_{\rm o})\right]\left\langle\varphi_{{\rm l}_i}(\vec{x}+z_{{\rm l}_i}\vec{\theta}_{\rm o})\mathbf{s}^{\rm T}\right\rangle\mathbf{M}_k^{\rm T}\right\}\end{aligned} \qquad \text{(B.18)}$$

Defining the $\mathbf{R}_{kk'}(\vec{\theta}_{\rm o})$ matrix:

$$\begin{aligned}\mathbf{R}_{kk'}(\vec{\theta}_{\rm o}) &= \int d^2\vec{x}\,W_{\rm a}(\vec{x})\left[\mathbf{r}_k(\vec{x}+z_{{\rm d}_k}\vec{\theta}_{\rm o}) - \bar{\mathbf{r}}_k(\vec{\theta}_{\rm o})\right]\left[\mathbf{r}_{k'}(\vec{x}+z_{{\rm d}_{k'}}\vec{\theta}_{\rm o}) - \bar{\mathbf{r}}_{k'}(\vec{\theta}_{\rm o})\right]^{\rm T} \\ &= \int d^2\vec{x}\,W_{\rm a}(\vec{x})\mathbf{r}_k(\vec{x}+z_{{\rm d}_k}\vec{\theta}_{\rm o})\mathbf{r}_{k'}^{\rm T}(\vec{x}+z_{{\rm d}_{k'}}\vec{\theta}_{\rm o}) - 2\bar{\mathbf{r}}_k(\vec{\theta}_{\rm o})\bar{\mathbf{r}}_{k'}^{\rm T}(\vec{\theta}_{\rm o}) + \bar{\mathbf{r}}_k(\vec{\theta}_{\rm o})\bar{\mathbf{r}}_{k'}^{\rm T}(\vec{\theta}_{\rm o}) \\ &= \int d^2\vec{x}\,W_{\rm a}(\vec{x})\mathbf{r}_k(\vec{x}+z_{{\rm d}_k}\vec{\theta}_{\rm o})\mathbf{r}_{k'}^{\rm T}(\vec{x}+z_{{\rm d}_{k'}}\vec{\theta}_{\rm o}) - \bar{\mathbf{r}}_k(\vec{\theta}_{\rm o})\bar{\mathbf{r}}_{k'}^{\rm T}(\vec{\theta}_{\rm o}) \qquad \text{(B.19)}\end{aligned}$$

B.6 Equation (4.35)

Defining the $\mathbf{A}_{ik}(\vec{\theta}_o)$ matrix from the third term of equation (B.18):

$$\begin{aligned}\mathbf{A}_{ik}(\vec{\theta}_o) &= \int d^2\vec{x}\, W_a(\vec{x}) \left[\mathbf{r}_k(\vec{x} + z_{d_k}\vec{\theta}_o) - \bar{\mathbf{r}}_k(\vec{\theta}_o)\right] \left\langle \varphi_{l_i}(\vec{x} + z_{l_i}\vec{\theta}_o)\mathbf{s}^T \right\rangle \\ &= \int d^2\vec{x}\, W_a(\vec{x})\mathbf{r}_k(\vec{x} + z_{d_k}\vec{\theta}_o) \left\langle \varphi_{l_i}(\vec{x} + z_{l_i}\vec{\theta}_o)\mathbf{s}^T \right\rangle \\ &\quad - \int d^2\vec{x}\, W_a(\vec{x})\bar{\mathbf{r}}_k(\vec{\theta}_o) \left\langle \varphi_{l_i}(\vec{x} + z_{l_i}\vec{\theta}_o)\mathbf{s}^T \right\rangle \end{aligned} \tag{B.20}$$

The second term of the preceding equation is equal to 0 because of the definition of $\varphi_{l_i}(\vec{x})$, hence

$$\mathbf{A}_{ik}(\vec{\theta}_o) = \int d^2\vec{x}\, W_a(\vec{x})\mathbf{r}_k(\vec{x} + z_{d_k}\vec{\theta}_o) \left\langle \varphi_{l_i}(\vec{x} + z_{l_i}\vec{\theta}_o)\mathbf{s}^T \right\rangle \tag{B.21}$$

Appendix C. *Additional Results*

In this appendix, some additional computational results using the analysis of Chapter IV are presented and discussed. Unless otherwise indicated, the geometry of Figure 4.6 and the parameters in Table 4.1 were used in the computations.

C.1 Photon Noise

Figure C.1 shows that the residual phase error in the object wavefront decreases asymptotically as the light level is increased. With a larger number of photons per subaperture, the WFS is able to obtain a better estimate of the centroid of the laser guide star image in each subaperture. This improved centroid estimate results in more accurate slope measurements. The values for N_{ph} in the figure are based on the photon-limited noise model presented in Chapter IV. Higher light levels are required to obtain similar results if readout noise is significant.

C.2 Guide Star Separation

The designer of an MCAO system may also be interested in the answer to the following question: Given the available resources (number of guide stars and DMs) and a known atmospheric turbulence profile, how large a field of view may be compensated while maintaining a specified level of residual phase error? Figure C.2 addresses this question for the MCAO system described by Figure 4.6 and Table 4.1. The figure plots the maximum level of residual phase error in the FOV vs. guide star separation. If the maximum allowed RMS error for any point in the FOV is $\lambda/7$, then the separation between the guide stars is limited to about 9 times the aperture dimension for this 2-layer atmospheric profile.

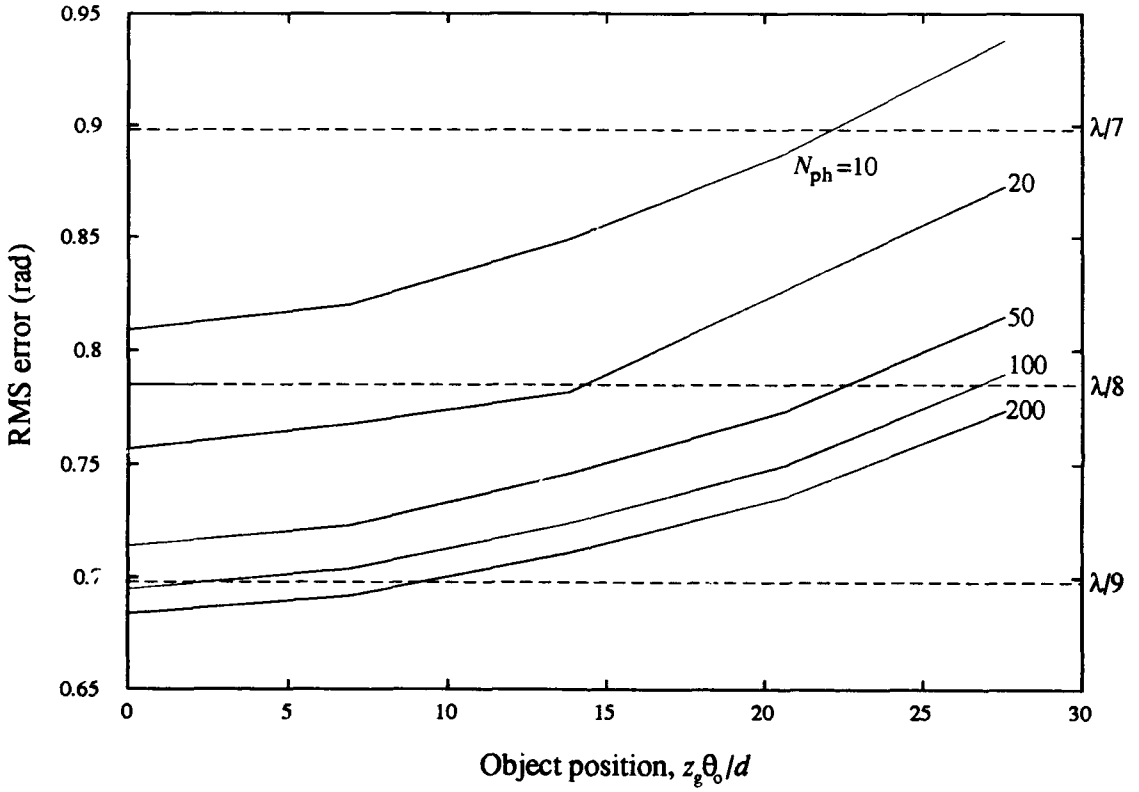

Figure C.1. RMS residual phase error averaged over object wavefront vs. object position for 2-DM adaptive telescope with 4 guide stars with light level as a parameter.

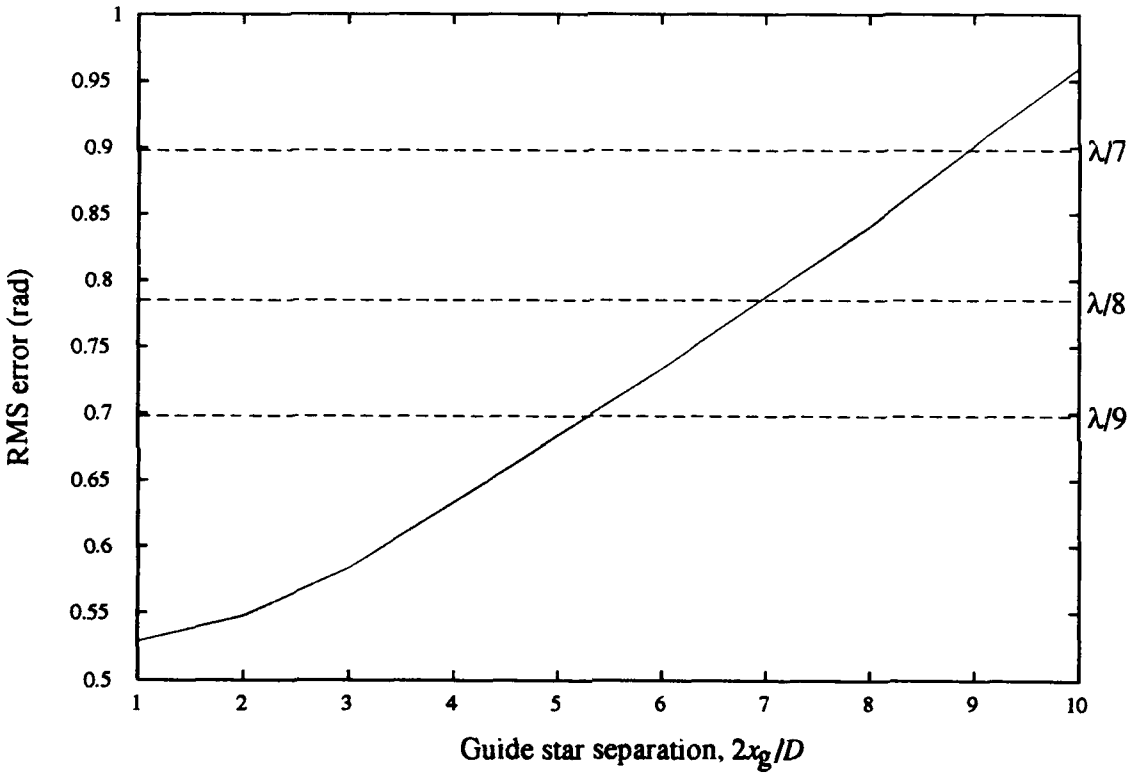

Figure C.2. Maximum RMS residual phase error averaged over object wavefront vs. guide star separation for 2-DM adaptive telescope with 4 guide stars.

C.3 Guide Star Projection Aperture

Figure 4.13 shows how the performance of an MCAO system is limited due to the inability to measure overall tilt using laser guide stars. However, suppose the telescope aperture we wish to compensate is smaller than the laser guide star projection aperture. As shown in Figure C.3, the overall tilt could be measured across the telescope aperture, since it is seen as part of a higher-order component from the point of view of the projection aperture. This point is illustrated quantitatively in Figure C.4, which shows how the performance of the MCAO system improves as the laser guide star projection aperture increases in size. The curves labeled $D_p/D = 1$ and $D_p/D = \infty$ correspond to the two curves in Figure 4.13.

C.4 Upper DM Actuator Density

In the results shown in Chapter IV, the same interactuator spacing was used for both DMs. Because of the larger size of the upper DM, as shown in Figure 4.9, it requires an array of 100 actuators vs. 49 for the lower DM when the same interactuator spacing is used. However, the upper DM is compensating for the weaker of the two turbulent layers. Since the upper layer accounts for only 10% of the total turbulence strength, it has very little power at high spatial frequencies. Thus, the DM assigned to this layer should be able to effectively compensate for the aberrations due to this layer with fewer actuators. In other words, since the upper DM reconstructs lower spatial frequency surfaces than the lower DM, it can allow a wider interactuator spacing. In Figure C.5, the interactuator spacing was increased on the upper DM to $2 \times r_0$ (25 actuators), $3 \times r_0$ (16 actuators), and $4 \times r_0$ (9 actuators). The figure shows that performance initially improves as the interactuator spacing increases. It is actually detrimental to use too many actuators, since good information about the high spatial frequencies achievable by a dense actuator array is not available for the weak turbulent layer. As the number of actuators is further decreased toward the limit of 0, the performance curve in Figure C.5 begins to tip up toward the single-DM performance curve.

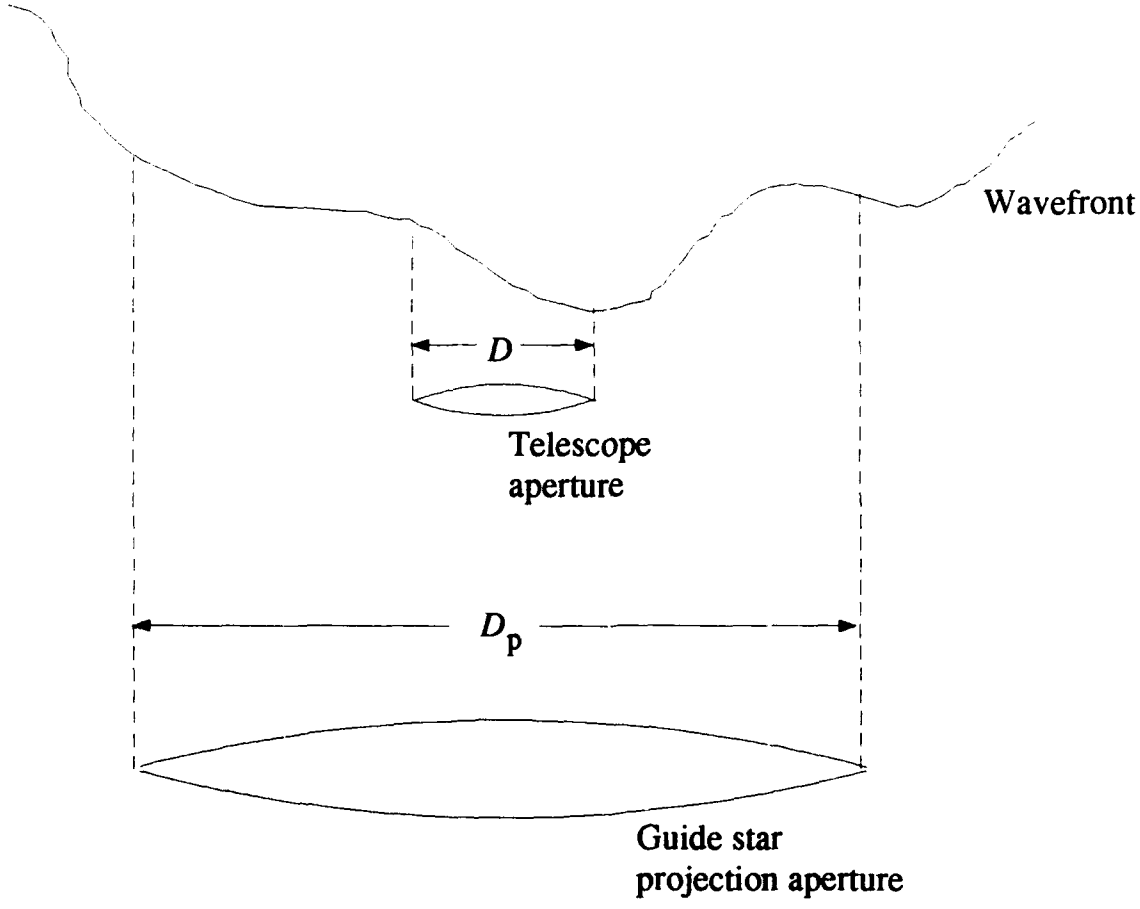

Figure C.3. The overall tilt component for a small aperture is part of a higher-order component for a large aperture.

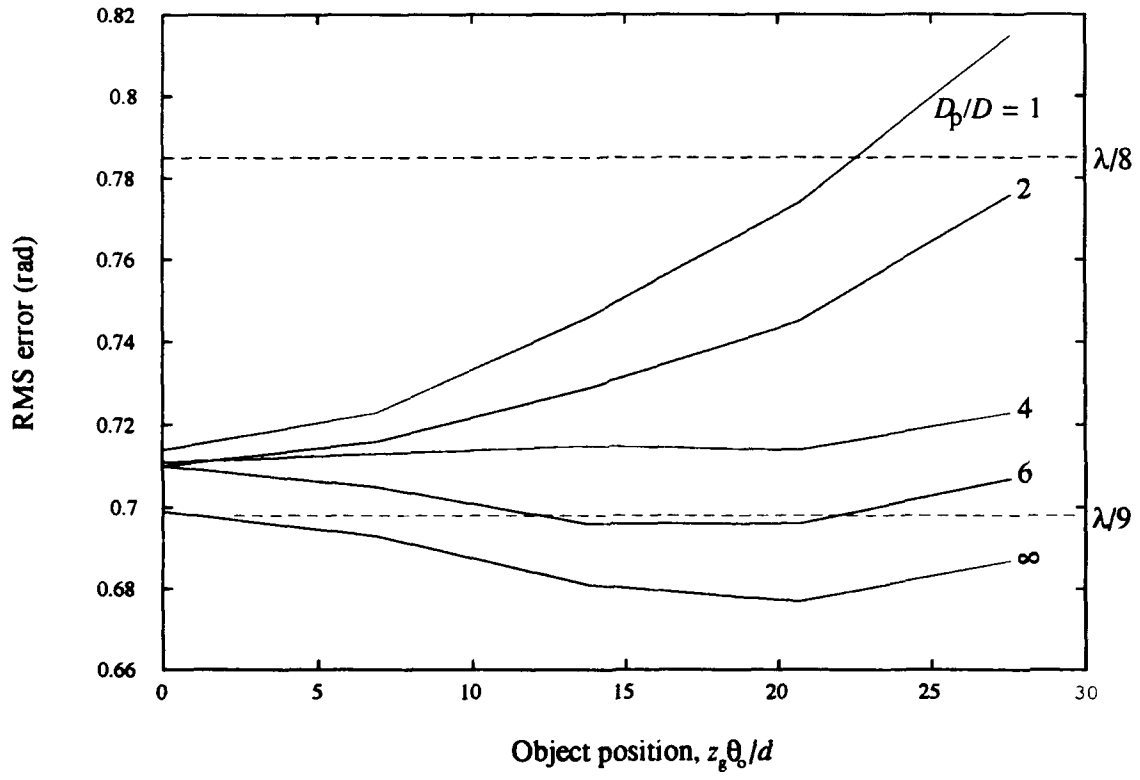

Figure C.4. RMS residual phase error averaged over object wavefront vs. object position for 2-DM adaptive telescope with 4 guide stars with projection aperture dimension as a parameter.

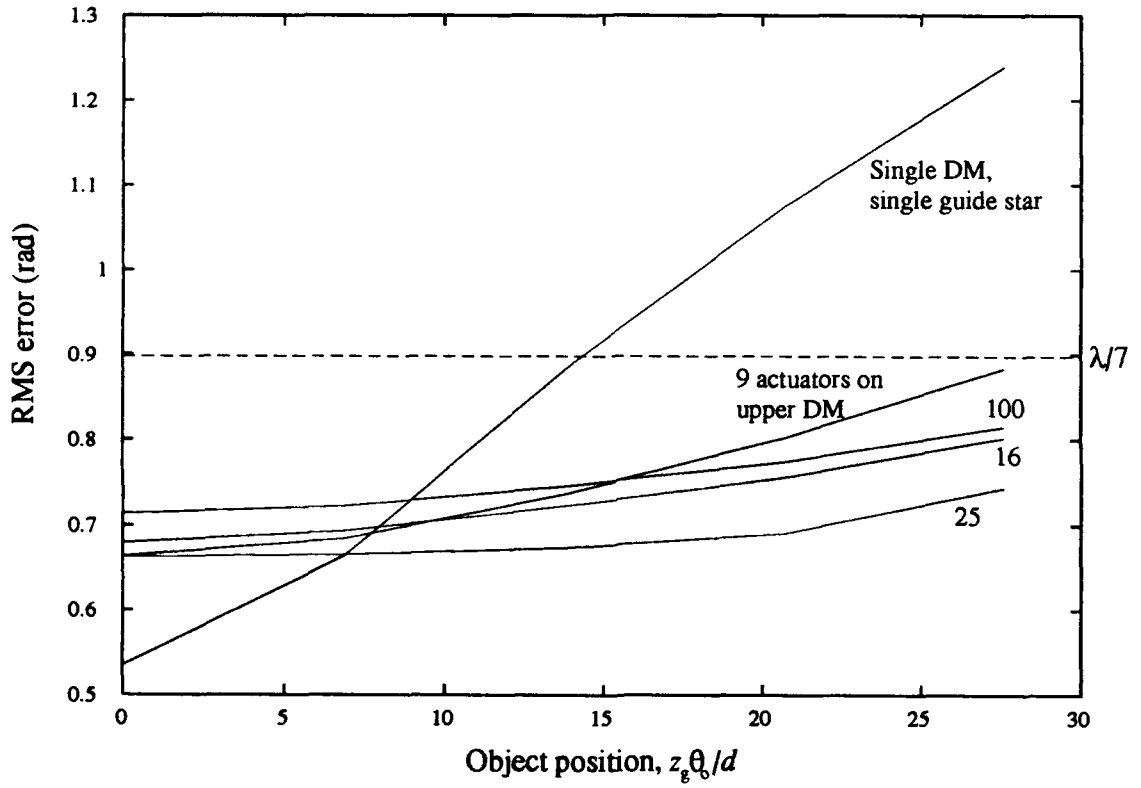

Figure C.5. RMS residual phase error averaged over object wavefront vs. object position for 2-DM adaptive telescope with 4 guide stars with number of actuators on upper DM as a parameter.

Bibliography

1. Allen, Jeff and others. "Speckle and Adaptive Optics Techniques," *Photonics Spectra*, 97–104 (August 1988).
2. Babcock, H. W. "The possibility of compensating astronomical seeing," *Pub. Astron. Soc. Pac.*, *65*(386):229–236 (October 1953).
3. Barakat, Richard and James W. Beletic. "Influence of atmospherically induced random wavefronts on diffraction imagery: a computer simulation model for testing image reconstruction algorithms," *J. Opt. Soc. Am. A*, 7(4):653–671 (April 1990).
4. Barakat, Richard and Peter Nisenson. "Influence of the wave-front correlation function and deterministic wave-front aberrations on the speckle image-reconstruction problem in the high-light-level regime," *J. Opt. Soc. Am.*, *71*(11):1390–1402 (November 1981).
5. Beckers, Jacques M. "Increasing the size of the isoplanatic patch with multiconjugate adaptive optics." *Proc. ESO Conf. on Very Large Telescopes and their Instrumentation*, edited by M.-H. Ulrich. 693–703. 1988.
6. Beyer, William H., editor. *CRC Standard Mathematical Tables* (25th Edition). West Palm Beach, Florida: CRC Press 1978.
7. Born, Max and E[illegible]olf. *Principles of Optics: Electromagnetic Theory of Propagation, Interference and Diffraction of Light* (6th Edition). Oxford: Pergamon Press, 1980.
8. Buffington, J. A. and others. "Correction of atmospheric distortion with an image-sharpening telescope," *J. Opt. Soc. Am.*, *67*(3):298–303 (March 1977).
9. Buffington, J. A. and others. "First observatory results with an image-sharpening telescope," *J. Opt. Soc. Am.*, *67*(3):304–305 (March 1977).
10. Claflin, E. Scott and Noah Bareket. "Configuring an electrostatic membrane mirror by least-squares fitting with analytically derived influence functions," *J. Opt. Soc. Am. A*, *3*(11):1833–1839 (November 1986).
11. Dicke, Robert H. "Phase-constrast detection of telescope seeing errors and their correction," *Astrophys. J.*, *198*(3):605–615 (June 1975).
12. Ealey, Mark A. and John F. Washeba. "Continuous facesheet low voltage deformable mirrors," *Optical Engineering*, *29*(10):1191–1198 (October 1990).
13. Ellerbroek, Brent L. *Wavefront and tilt estimators for the SOR-3 experiment*. Technical Report TR-684, Placentia, CA: the Optical Sciences Company, December 1985.
14. Ellerbroek, Brent L. "First-order performance evaluation of adaptive optics systems for atmospheric turbulence compensation in extended field-of-view astronomical telescopes," *J. Opt. Soc. Am. A* (1993). Draft pre-print.
15. Foy, R. and A. Labeyrie. "Feasibility of adaptive telescope with laser probe," *Astron. and Astrophys.*, *152*:L29–L31 (1985).
16. Foy, Renaud. "Work in France in the field of the laser artificial guide star." *Proceedings of the Laser Guide Star Adaptive Optics Workshop*. 1992.
17. Fried, D. L. "Statistics of a geometric representation of wavefront distortion," *J. Opt. Soc. Am.*, *55*(11):1427–1435 (November 1965).
18. Fried, D. L. "Optical resolution through a randomly inhomogeneous medium for very long and very short exposures," *J. Opt. Soc. Am.*, *56*:1372–1379 (1966).

19. Fried, David L. *Adaptive optics for imaging within the atmosphere: Reference generation and field-of-view widening*. Technical Report TR-273, the Optical Sciences Company, August 1977.

20. Fugate, R. Q. and others. "Measurement of atmospheric wavefront distortion using scattered light from a laser guide-star," *Nature*, *353*:144–146 (12 September 1991).

21. Fugate, Robert and Brent Ellerbroek, Phillips Laboratory/Starfire Optical Range. Briefing to AFIT students. Air Force Institute of Technology (AU), Wright-Patterson AFB OH, 8 July 1991.

22. Gardner, Chester S. and others. "Design and performance analysis of adaptive optical telescopes using laser guide stars," *Proc. IEEE*, *78*(11):1721–1743 (November 1990).

23. Gaskill, Jack D. *Linear Systems, Fourier Transforms, and Optics*. New York: John Wiley & Sons, 1978.

24. Genrui, Cao and others. "An experimental study on photon noise limited wavefront sensor." *International Conference on Optoelectronic Science and Engineering, Proc. SPIE1230*. 457–460. 1990.

25. Goodman, Joseph W. *Introduction to Fourier Optics*. San Francisco: McGraw-Hill Book Company, 1968.

26. Goodman, Joseph W. *Statistical Optics*. New York: John Wiley & Sons, 1985.

27. Greenwood, D. P. "Bandwidth specification for adaptive optics systems," *J. Opt. Soc. Am.*, *67*(3):390 (March 1977).

28. Greenwood, Darryl P. and Charles A. Primmerman. "Adaptive optics research at Lincoln Laboratory," *Lincoln Laboratory Journal*, *5*(1):3–24 (1992).

29. Hardy, John W. "Active optics: A new technology for the control of light," *Proc. IEEE*, *66*(6):651–697 (June 1978).

30. Hardy, John W. "Instrumental limitations in adaptive optics for astronomy." *Active Telescope Systems, Proc. SPIE1114*. 2–13. 1989.

31. Hardy, John W. "Adaptive optics—a progress review." *Active and Adaptive Optical Systems, Proc. SPIE1542*, edited by Mark A. Ealey. 2–17. 1991.

32. Hudgin, Richard. "Wavefront compensation error due to finite corrector element size," *J. Opt. Soc. Am.*, *67*(3):393–395 (March 1977).

33. Hufnagel, Robert E. "Propagation through atmospheric turbulence." *The Infrared Handbook* edited by William L. Wolfe and George J. Zissis, chapter 6, Washington, DC: U.S. Government Printing Office, 1978.

34. Hulburd, Bill and David Sandler. "Segmented mirrors for atmospheric compensation," *Optical Engineering*, *29*(10):1186–1190 (October 1990).

35. Humphreys, Ronald A. and others. "Atmospheric-turbulence measurements using a synthetic beacon in the mesospheric sodium layer," *Optics Letters*, *16*(18):1367–1369 (15 September 1991).

36. Humphreys, Ronald A. and others. "Sodium-layer synthetic beacons for adaptive optics," *Lincoln Laboratory Journal*, *5*(1):45–66 (1992).

37. Iizuka, Keigo. *Engineering Optics* (2nd Edition). Berlin: Springer-Verlag, 1987.

38. Johnston, Dustin C. and Byron M. Welsh. "Estimating contributions of turbulent layers to total wavefront phase aberration." *Atmospheric Propagation and Remote Sensing, Proc. SPIE1688*, edited by A. Kohnle and W. B. Miller. 510–521. 1992.

39. Johnston, Dustin C. and Byron M. Welsh. "Estimating the contribution of different parts of the atmosphere to optical wavefront aberration," *Computers and Electrical Engineering*, *18*(6):467–483 (1992).

40. Kane, T. J. and others. "Wavefront detector optimization for laser guided adaptive telescopes." *Active Telescope Systems, Proc. SPIE1114*, edited by François Roddier. 160–171. March 1989.

41. Kern, Pierre. "COME-ON: an adaptive optics prototype dedicated to infrared astronomy." *Active Telescope Systems, Proc. SPIE1114*, edited by François Roddier. 54–64. 1989.

42. Kolmogorov, A. N. "Dissipation of energy in the locally isotropic turbulence." *Turbulence: Classic Papers on Statistical Theory* edited by S. K. Friedlander and Leonard Topper, 159–161, London: Interscience, 1961.

43. *Lincoln Laboratory Journal*. Massachusetts Institute of Technology, Spring, 1992. Special issue on adaptive optics.

44. "MACSYMA." Symbolics, Inc., computer software.

45. McKechnie, T. Stewart. "Light propagation through the atmosphere and the properties of images formed by large ground-based telescopes," *J. Opt. Soc. Am. A*, *8*(2):346–365 (February 1991).

46. Murphy, Daniel V. "Atmospheric-turbulence compensation experiments using cooperative beacons," *Lincoln Laboratory Journal*, *5*(1):25–44 (1992).

47. Murphy, Daniel V. and others. "Experimental demonstration of atmospheric compensation using multiple synthetic beacons," *Optics Letters*, *16*(22):1797–1799 (15 November 1991).

48. Noll, R. J. "Zernike polynomials and atmospheric turbulence," *J. Opt. Soc. Am.*, *66*(3):207–211 (March 1976).

49. Parenti, Ronald R. "Adaptive optics for astronomy," *Lincoln Laboratory Journal*, *5*(1):93–114 (1992).

50. Primmerman, Charles A. and others. "Compensation of atmospheric optical distortion using a synthetic beacon," *Nature*, *353*:141–143 (12 September 1991).

51. Rigaut, François. "Dual adaptive optics: a solution to the tilt determination problem using laser guide star." *Proceedings of the Laser Guide Star Adaptive Optics Workshop*. 1992.

52. Roddier, F. and others. "Seeing at Mauna Kea: a joint UH-UN-NOAO-CFHT study." *Advanced Technology Optical Telescopes IV, Proc. SPIE1236*, edited by Lawrence D. Barr. 485–491. 1990.

53. Roddier, François. "Curvature sensing and compensation: a new concept in adaptive optics," *Appl. Opt.*, *27*(7):1223–1225 (1988).

54. Roddier, François. "Astronomical adaptive optics with natural reference stars." *Proceedings of the Laser Guide Star Adaptive Optics Workshop*. 1992.

55. Rousset, G. and others. "First diffraction-limited astronomical images with adaptive optics," *Astron. and Astrophys.*, *230*:L29–32 (1990).

56. Steinhaus, Ehud and S. G. Lipson. "Bimorph piezoelectric flexible mirror," *J. Opt. Soc. Am.*, *69*(3):478–481 (March 1979).

57. Tallon, M. and R. Foy. "Adaptive telescope with laser probe: isoplanatism and cone effect," *Astron. and Astrophys.*, *235*:549–557 (1990).

58. Thompson, Laird A. and Chester S. Gardner. "Experiments on laser guide stars at Mauna Kea Observatory for adaptive imaging in astronomy," *Nature*, *328*:229–231 (1987).

59. Tyson, Robert K. "Adaptive optics system performance approximations for atmospheric turbulence correction," *Optical Engineering*, *29*(10):1165–1173 (October 1990).

60. Tyson, Robert K. *Principles of Adaptive Optics*. Boston: Academic Press, Inc., 1991.

61. Vernin, J. and F. Roddier. "Experimental determination of two-dimensional spatiotemporal power spectra of stellar light scintillation. Evidence for a multilayer structure of the air turbulence in the upper troposphere," *J. Opt. Soc. Am.*, *63*(3):270–273 (March 1973).

62. Wallner, Edward P. "Optimal wave-front correction using slope measurements," *J. Opt. Soc. Am.*, *73*:1771–1776 (December 1983).

63. Welsh, Byron M. and Chester S. Gardner. "Performance analysis of adaptive-optics systems using laser guide stars and slope sensors," *J. Opt. Soc. Am. A*, *6*(12):1913–1923 (December 1989).

64. Welsh, Byron M. and Chester S. Gardner. "Effects of turbulence-induced anisoplanatism on the imaging performance of adaptive-astronomical telescopes using laser guide stars," *J. Opt. Soc. Am. A*, *8*(1):69–80 (January 1991).

65. Zollars, Byron G. "Atmospheric-turbulence compensation experiments using synthetic beacons," *Lincoln Laboratory Journal*, *5*(1):67–92 (1992).

Vita

Captain Dustin C. Johnston was born on 13 September 1960 in Peoria, Illinois. He graduated from high school in East Peoria, Illinois, in 1978 and attended the USAF Academy, receiving the Bachelor of Science in Electrical Engineering in June, 1982. Captain Johnston has served in various Air Force assignments, including electronic warfare systems engineer at the USAF Tactical Air Warfare Center, Eglin AFB, FL. In 1989, Captain Johnston received the Master of Science in Electrical Engineering from the Air Force Institute of Technology (AFIT). He entered the PhD program at AFIT in 1990.

Permanent address: 201 Pekin Avenue
East Peoria, Illinois 61611

REPORT DOCUMENTATION PAGE

Form Approved
OMB No. 0704-0188

1. AGENCY USE ONLY (Leave blank)	2. REPORT DATE	3. REPORT TYPE AND DATES COVERED
	December 1992	Doctoral Dissertation

4. TITLE AND SUBTITLE
INCREASING THE CORRECTED FIELD OF VIEW OF AN ADAPTIVE OPTICAL TELESCOPE

5. FUNDING NUMBERS

6. AUTHOR(S)
Dustin C. Johnston, Captain, USAF

7. PERFORMING ORGANIZATION NAME(S) AND ADDRESS(ES)
Air Force Institute of Technology, WPAFB OH 45433-6583

8. PERFORMING ORGANIZATION REPORT NUMBER
AFIT/DS/ENG/92-06

9. SPONSORING/MONITORING AGENCY NAME(S) AND ADDRESS(ES)
Phillips Laboratory/LITE
Kirtland AFB NM 87117

10. SPONSORING/MONITORING AGENCY REPORT NUMBER

11. SUPPLEMENTARY NOTES

12a. DISTRIBUTION/AVAILABILITY STATEMENT
Approved for public release; distribution unlimited

12b. DISTRIBUTION CODE

13. ABSTRACT *(Maximum 200 words)*

Current adaptive optical telescope designs use a single deformable mirror (DM) to compensate for atmospheric distortion. The corrected field of view (FOV) of an adaptive optics system could be increased through the use of multiple DMs optically conjugated to corresponding planes which sample the turbulence region in altitude. Often, the atmospheric turbulence responsible for the degradation of telescope images is concentrated in several layers. Each DM would correct for the component of the total wavefront in the pupil contributed by one or more layers. If the atmosphere does not possess a layered structure, the best fit of the turbulence profile can be made to a layered model. This dissertation describes and analyzes two novel methods for estimating the proper DM surfaces which would result in wide-FOV compensation. Both methods use multiple wavefront sensor measurements to estimate the three-dimensional turbulence structure. The wavefront measurements are made using artificial guide stars created by scattered laser light. The analysis includes the effects of noise, realistic models of systems components, and the limitations of artificial guide stars. It is shown that multiple-DM, multiple-guide-star systems can significantly increase the compensated FOV relative to single-DM, single-guide star systems.

14. SUBJECT TERMS	15. NUMBER OF PAGES
Adaptive optics, telescopes, wavefronts, optical analysis, image compensation	138
	16. PRICE CODE

17. SECURITY CLASSIFICATION OF REPORT	18. SECURITY CLASSIFICATION OF THIS PAGE	19. SECURITY CLASSIFICATION OF ABSTRACT	20. LIMITATION OF ABSTRACT
UNCLASSIFIED	UNCLASSIFIED	UNCLASSIFIED	UL